1992

# Neutron diffraction study of the electronic structure of high-T[subscript c] superconductor-related compounds

Xun-Li Wang
*Iowa State University*

Order Number 9223978

# Neutron diffraction study of the electronic structure of high-$T_c$ superconductor-related compounds

Wang, Xun-Li, Ph.D.

Iowa State University, 1992

U·M·I
300 N. Zeeb Rd.
Ann Arbor, MI 48106

# Neutron diffraction study of the electronic structure of high-$T_c$ superconductor-related compounds

by

Xun-Li Wang

A Dissertation Submitted to the
Graduate Faculty in Partial Fulfillment of the
Requirements for the Degree of
DOCTOR OF PHILOSOPHY

Department: Physics and Astronomy
Major: Solid State Physics

Approved:

Signature was redacted for privacy.

In Charge of Major Work

Signature was redacted for privacy.

For the Major Department

Signature was redacted for privacy.

For the Graduate College

Iowa State University
Ames, Iowa

1992

# TABLE OF CONTENTS

## LIST OF FIGURES

# LIST OF TABLES

# I. INTRODUCTION

Over the past few years, tremendous efforts have been devoted to the study of the physical properties of high-$T_c$ superconductors and their non-superconducting parent compounds [1]. Numerous experimental studies of the superconductors, in both superconducting and normal states, have revealed many properties that are substantially different from the characteristics of the conventional superconductors. This, in turn, raises a serious question regarding whether the high-temperature superconductivity derives from the same paring mechanism known to be responsible for the conventional superconductors. The parent compounds, although not superconducting, are also interesting, not only because they serve as references to the study of the superconductors, but also because they display a rich variety of physics phenomena (e.g., the 2-dimensional antiferromagnetic correlations) that have not been fully explored before. Among the extensively studied compounds, $La_2CuO_4$, which has a $K_2NiF_4$ crystal structure, has received special attention.

## A. Crystal Structure

$La_2CuO_4$ is an insulator. At high temperatures, the compound has a body-centered tetragonal structure with space group I/4mmm. As temperature decreases, it undergoes a structural transition to an orthorhombic phase characterized by space group Bmab. The transition temperature, $T_o$, depends strongly on the oxygen content [2-5]. For the stoichiometric compound, $T_o \sim 530$ K. Following Axe et al. [6], we shall use HTT and LTO to label the high-temperature-tetragonal and the low-temperature-orthorhombic phase, respectively. The LTO cell is related to the HTT cell by a doubling of the basal plane in $\sqrt{2} \times \sqrt{2}$ fashion. In addition, the $CuO_6$ octahedra also rotate slightly around the

a-axis (the shorter axis of the basal plane) of the orthorhombic cell. As a result of this rotation, there is a new set of Bragg reflections in the LTO phase. Figure 1.1 shows the crystal structure of $La_2CuO_4$ in the LTO phase and the motion of oxygen atoms at the HTT-LTO phase transition.

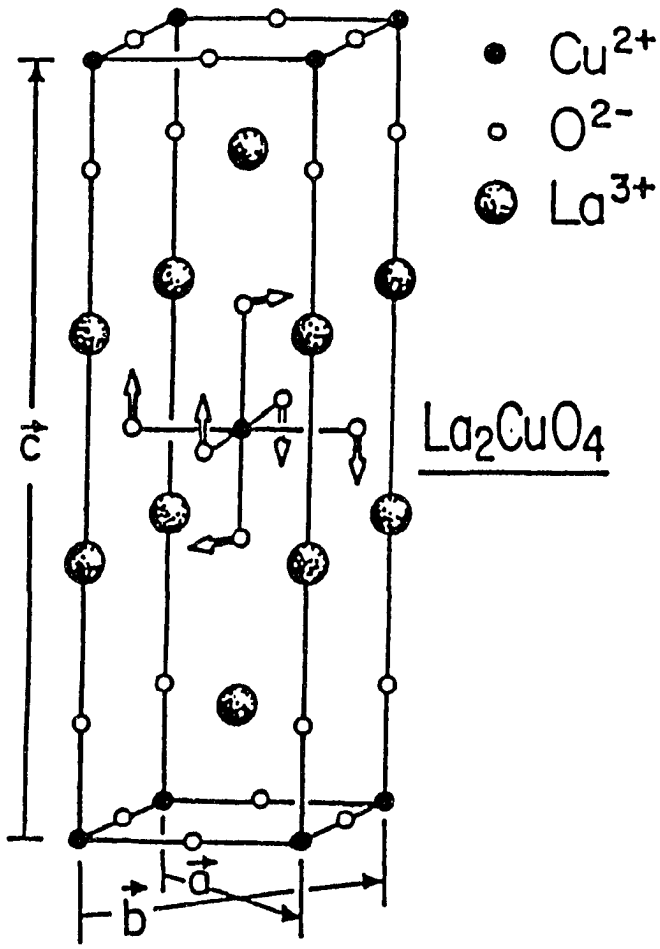


Figure 1.1 Crystal structure of $La_2CuO_4$ in the LTO phase. The center arrows show the motion of oxygen atoms at the HTT-LTO structure phase transition. (Adapted from Ref. 19)

In Ba-doped compounds, there is another phase transition at lower temperatures. Below the transition temperature, the crystal structure reverts to tetragonal but with space group $P4_2/ncm$ of lower symmetry [6-7]. This phase is denoted as LTT (low-temperature-tetragonal) to distinguish it from the HTT phase. Figure 1.2 is the experimentally determined phase diagram for $La_{2-x}Ba_xCuO_4$. The LTT phase is a very interesting modification of the LTO phase, in which the buckling of the octahedra rotate about one of the <1 1 0> axes rather than about the [1 0 0] axis in the LTO phase. Since the crystal symmetry is lower in the LTT phase, an extra set of Bragg reflections, which are not allowed in either the LTO or the HTT phase, appears. The LTT phase is not unique to the Cu compounds; it exits in Ni compounds [8-10] and possibly in Co compounds [11] as well. For this reason, it has been regarded as a common feature in the crystal structure of these so-called 2-1-4 compounds.

## B. Antiferromagnetism

### 1. Antiferromagnetic ordering

In the LTO phase, $La_2CuO_4$ orders antiferromagnetically as the temperature further lowers. This was first suggested in the magnetic susceptibility measurements [12]. As shown in Figure 1.3, the magnetic susceptibility of $La_2CuO_4$ displays an anomaly between 200 and 300 K. The magnitude and position of the anomaly depend strongly on the oxygen content. Subsequent neutron diffraction experiments [5,13-16] identified the anomaly as associated with the onset of the antiferromagnetic ordering of the spins on the $Cu^{2+}$ ions. The magnetic structure established by neutron diffraction experiments is shown in Figure 1.4: The moments are along the LTO[0 1 0] axis and the magnetic propagation wave vector is along the [1 0 0] axis.

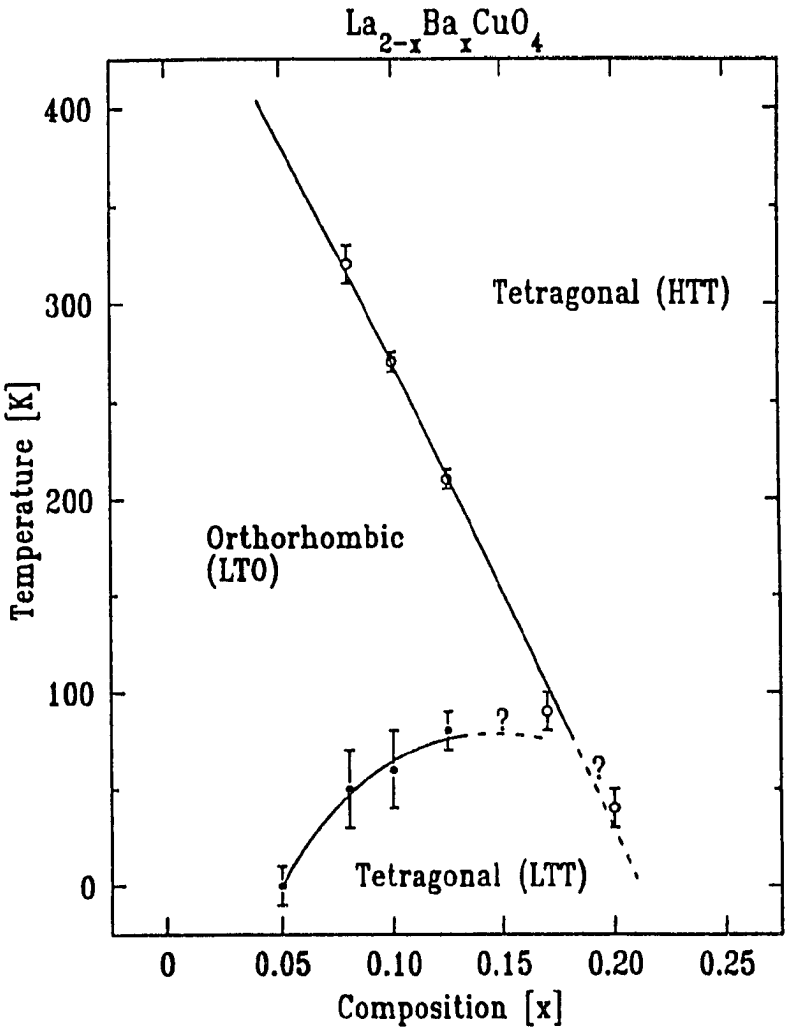


Figure 1.2 **Experimental phase diagram for $La_{2-x}Ba_xCuO_4$. For x>0.15, the small orthorhombicity increasingly blurs the distinction between orthorhombic and tetragonal. (After Ref. 6)**

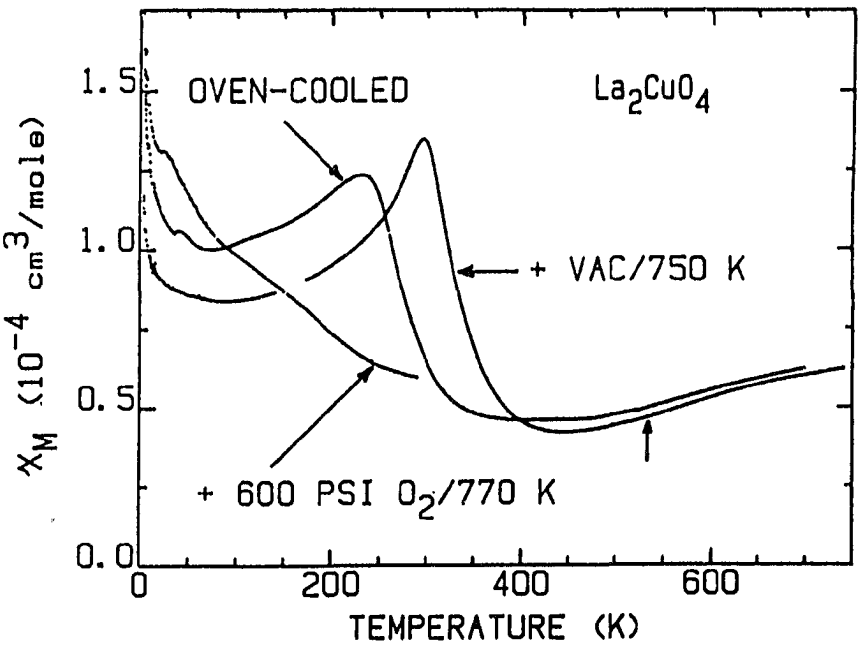


Figure 1.3 Magnetic susceptibility for three samples of $La_2CuO_4$. The samples were prepared by different procedures and of different oxygen contents. (After Ref. 12)

## 2. Magnetic dynamics

The continuing interest in $La_2CuO_4$ was led by discoveries that the magnetic dynamics in this compound can be well described by a two-dimensional (2D) spin 1/2 Heisenberg antiferromagnet [17-25].

Inelastic neutron scattering experiments [17-19] have established that, in the previously believed "paramagnetic" region, the spins in the Cu-O planes are actually

antiferromagnetically correlated, with the correlation length increasing progressively as the transition temperature is approached [Figure 1.5(a)]. As shown in Figures 1.5(b) and 1.6(a), the 2D scattering intensity (due to correlated spins) exhibits a maxima at about $T_N$. Below $T_N$, the intensity decreases but does not vanish even at T = 0 K. This evidence indicates that the 3D long-range order is driven by the 2D spin fluctuations. The spins in the Cu-O planes are always correlated. As soon as the 2D correlation length becomes sufficiently large, the interplanar coupling triggers a transition to the 3D long-range order.

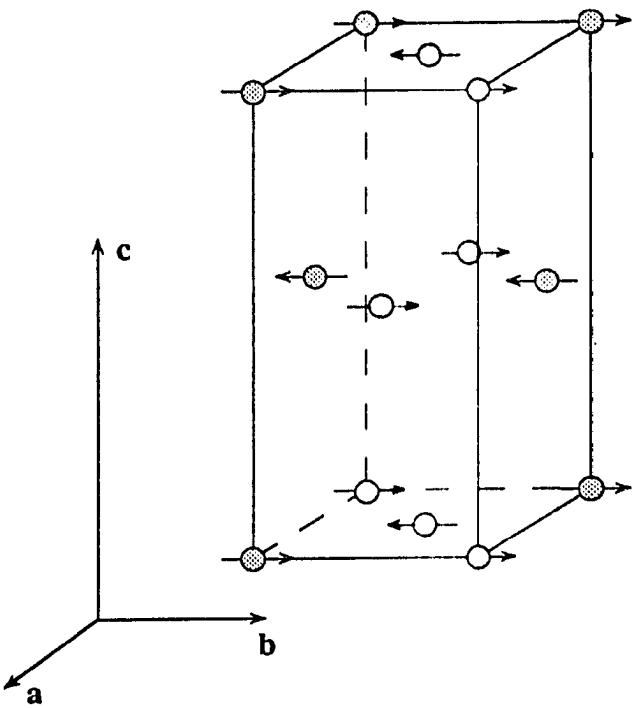


Figure 1.4 **Magnetic structure of $La_2CuO_4$.** For simplicity, only Cu atoms are plotted. The moments are aligned along the b-axis (the longer axis of the orthorhombic basal plane) and the magnetic propagation wave vector is along the a-axis.

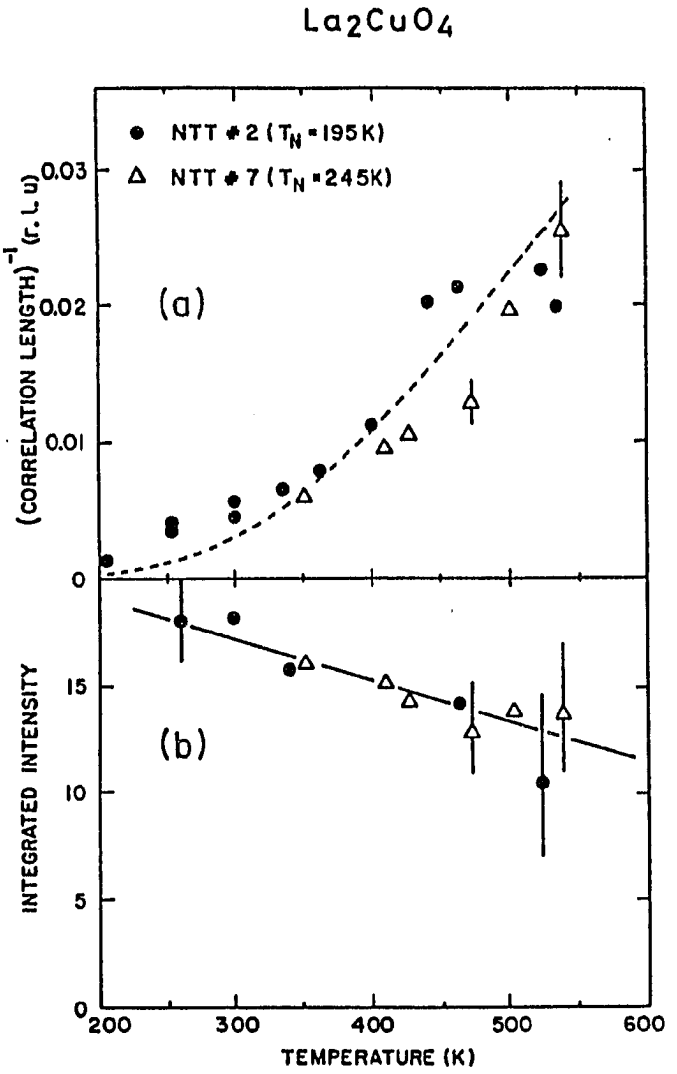


Figure 1.5 Temperature dependence of 2D scattering from the correlated spins in $La_2CuO_4$. The measurements were conducted at **Q** = (1 0 0.59). The two sets of symbols represent measurements on separate samples. 1 r.l.u. = $2\pi/a$ = 1.178 $Å^{-1}$. (a) Inverse correlation length. The dashed curve is the calculated results based on CHN's solutions of the 2D spin 1/2 Heisenberg antiferromagnet (see text). (b) Integrated intensity. The solid curve is a guide to the eye. (After Ref. 19)

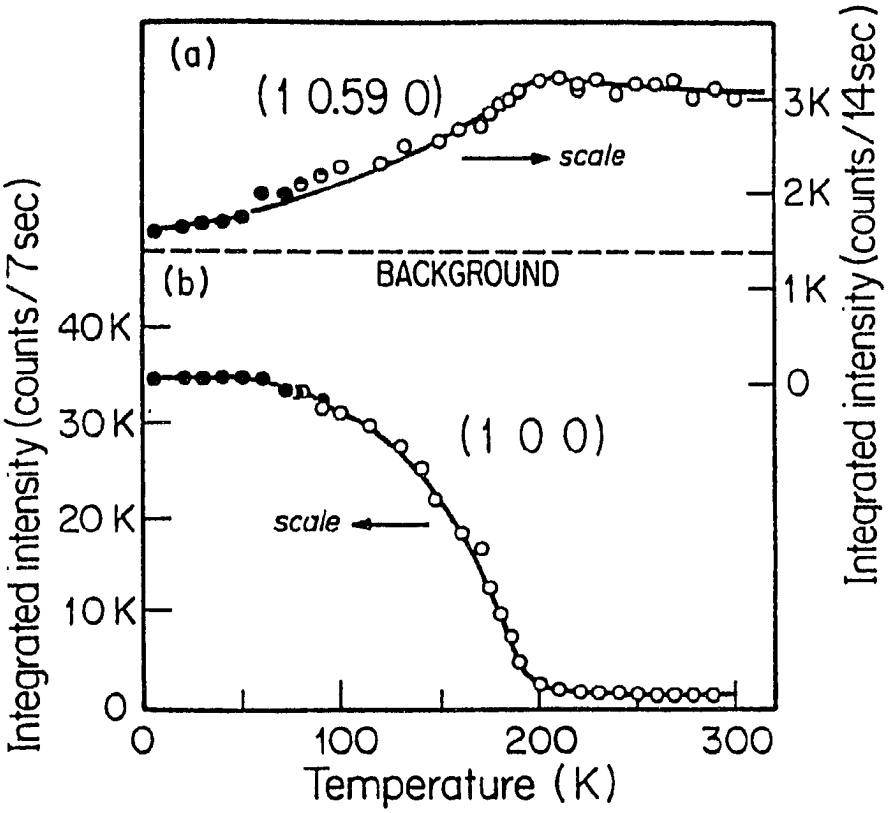


Figure 1.6 Temperature dependence of the integrated intensity of the 2D and 3D scattering from the spins in $La_2CuO_4$. (a) The 2D scattering at (1 0 0.59). (b) The (1 0 0) 3D antiferromagnetic Bragg peaks. The open and closed circles represent separate experiments which were normalized in the overlap region. The solid curves are guides to the eye. (After Ref. 18)

These experimental observations have inspired many developments in theories to elucidate the basics of the 2D spin 1/2 Heisenberg antiferromagnet. The most remarkable breakthrough was made by Chakravarty, Halperin and Nelson (CHN) [20]. By using a combination of hydrodynamics, dynamic scaling, renormalization analysis, and a fit to

the simulations of a classical rotor model, they were able to calculate the correlation length [Figure 1.5(a)] as well as the profile of neutron scattering intensities. The overall agreement with the experimental data is very good, considering that there is no adjustable parameter in the calculations. This shows that, for $T > T_N$, the main features of the spin fluctuations in $La_2CuO_4$ can be understood within the classical Heisenberg picture.

For temperatures below or near $T_N$, the magnetic dynamics is characterized by normal spin-wave excitations [21-23]. Figure 1.7 shows the fits using conventional spin-wave theory to the inelastic neutron scattering data collected at T = 296 K on a sample with $T_N = 295 \pm 5$ K. The long wavelength spin-wave velocity deduced from the fit is $c = 0.75 \pm 0.03$ eVÅ. At T = 5 K, c increases to $0.85 \pm 0.03$ eVÅ. This value corresponds to a coupling constant $J = 0.136 \pm 0.005$ eV, consistent with the coupling constants derived from susceptibility [24] and Raman scattering [25] measurements. Because of the stiff spin-wave velocity, the neutron scattering measurements were extremely difficult. Nevertheless, by using a time-of-flight chopper spectrometer operated on a pulsed spallation source (see Chapter III), Hayden et al. [23] managed to measure the one-magnon excitations throughout the Brillouin zone. The zone-boundary magnons have an energy $\hbar\omega = 0.312 \pm 0.005$ eV and are good eigenstates of the quantum Heisenberg Hamiltonian in that they possess lifetimes $> 10/\omega$.

## C. Magnetic Form Factor

Although the magnetic dynamics in $La_2CuO_4$ has been well established, considerably less is known about the electronic structure of the antiferromagnetic ground state.

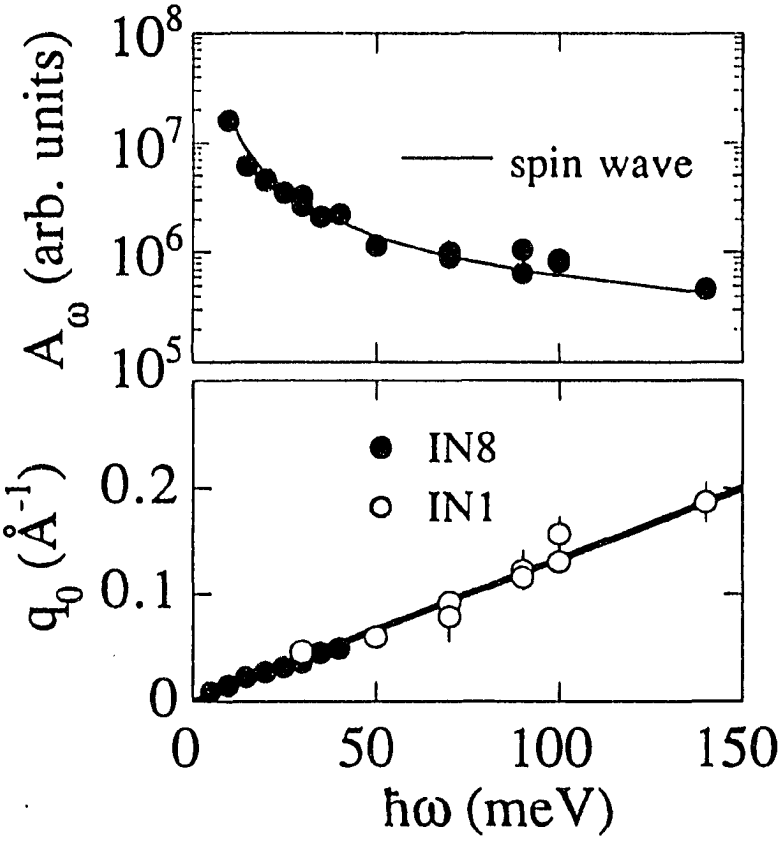


Figure 1.7 Fits to the magnetic excitations in $La_2CuO_4$ using the conventional spin-wave theory. The experimental data were collected at T = 296 K on a sample with $T_N$ = 290±5 K. The upper and lower frame are fitted spin-wave amplitudes and wave vectors, respectively. The solid and open symbols in the lower frame represent data measured with different instruments. (After Ref. 22)

Numerous non-spin-polarized band theoretical calculations [26] have been carried out to study the paramagnetic state of $La_2CuO_4$. In all cases, band-calculation results suggest that the Cu 3d hybridize strongly with O 2p orbitals forming bonding and antibonding bands. The Fermi energy cuts through a single antibonding band arising from hybridization between the Cu $3d_{x^2-y^2}$ and the nearest-neighbor in-plane O $2p_x$ and $2p_y$ orbitals. A $Cu^{2+}$ has 9 electrons on the 3d shell, thus the $d_{x^2-y^2}$ antibonding band is half filled and it should account for most of the magnetic behavior in this compound.

The investigation of the antiferromagnetic state within the local spin-density approximation was initiated by Leung, Wang, and Harmon [27], followed by a number of other groups [26]. None of their calculations, however, found a stable antiferromagnetic ground state. This is contrary to the experimental observations and is regarded as a breakdown of band theory, which is one-electron mean-field theory, in treating the strong on-site Coulomb correlations within the local spin-density approximation.

From the experimental perspective, the most direct method of establishing the nature of the electronic ground state would be to determine the complete charge density distribution in the solid, but this is a complex task and there are as yet no experiments of sufficient accuracy reported.

Alternatively, we may determine the spin density, or more precisely the magnetization density, if there is an orbital angular momentum contribution to the moment, of these materials through a Fourier transform of the magnetic form factor measured by neutron diffraction experiments. This is not as simple to interpret as the charge density, because the magnetization density depends on the difference between the charge density and the relative population of the spin-up and spin-down states.

Furthermore, in antiferromagnetic materials, it is possible to measure two different magnetization densities. The antiferromagnetic magnetization density may be determined by accurately measuring the structure factor of the magnetic Bragg reflections. The magnetization density thus obtained must reflect the symmetry of the antiferromagnetic state and address the question of the ground state wavefunctions. There is also the magnetization density induced by applying a magnetic field to the system and measured with polarized neutrons, which gives the spatial dependence of the susceptibility. These two densities are different as their symmetries are different.

Figure 1.8 shows the antiferromagnetic form factor of $La_2CuO_4$ measured by Freltoft et al. [28]. In a diffraction experiment, one measures the magnetic amplitude $\mu f(\mathbf{Q})$, i.e., the product of the ordered moment and the normalized magnetic form factor. The data presented in Figure 1.8 were scaled [28] by assuming $f(\mathbf{Q}) = 0.835$ for the (1 0 0) reflection. This led to an ordered moment $\mu = 0.30\ \mu_B$ per Cu atom. Two questions are at issue: one is on the relative shape of the form factor and the other on the value of the ordered moment. We shall address the second question in the latter part of this chapter.

As shown in Figure 1.8, the experimentally determined form factor appears to exhibit a plateau at low Q values (up to about 3 $Å^{-1}$). Consequently, the experimental data cannot be satisfactorily fitted by the spherical Cu 3d form factor which decreases continuously as a function of Q. The experimental data were also compared with the band theoretical form factor (of the hybridized Cu $3d_{x^2-y^2}$ band) obtained by Leung et al. [27]. In their calculations, about 20% of the moments were contributed by the out-of-plane oxygen atoms. As shown in Figure 1.8, however, the poor agreement with the experimental data does not seem to support such a claim.

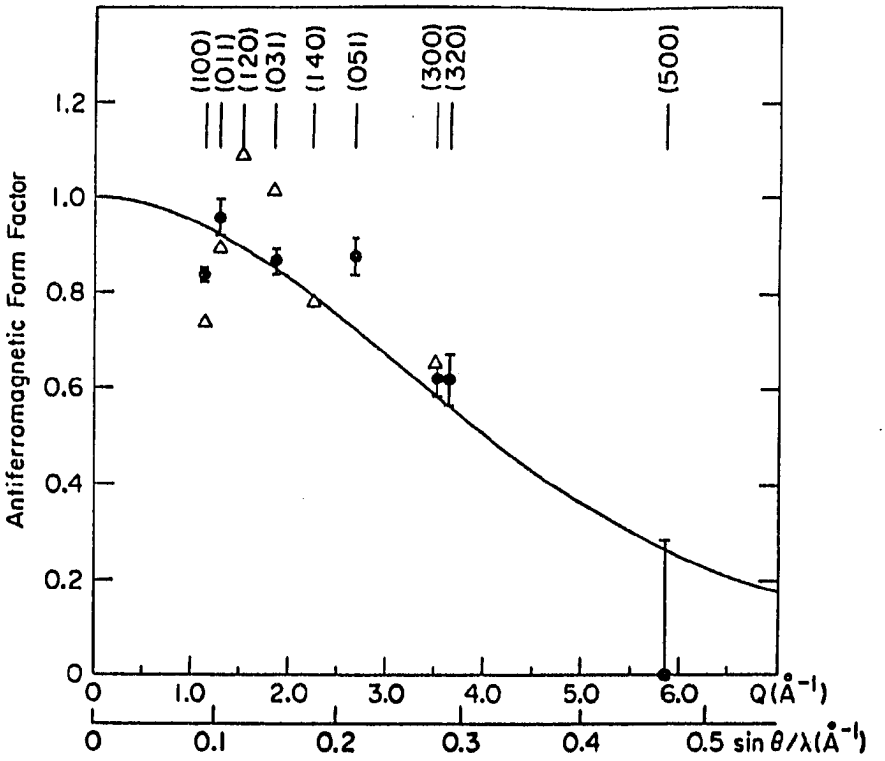


Figure 1.8 The antiferromagnetic form factor of $La_2CuO_4$. The solid circles represent the experimental data with the appropriate reflections indicated above. Notice that the indexes are based upon space group Cmca which is crystallographically equivalent to Bmab used in the preceding sections. The triangles are the band theoretical form factor (see text), and the full curve is a fit using the spherical Cu 3d form factor. (After Ref. 28)

It should be noted that the band theoretical form factor was obtained by applying a field to the paramagnetic state. By definition, it is the field-induced form factor, which is not, at least in principle, the same as the antiferromagnetic form factor. (Direct comparison between the experimental data and band calculations in the antiferromagnetic

state is not possible, as the band theory failed to obtain an antiferromagnetically ordered state.) In order to make fair comparisons with band-structure calculations, Stassis et al. [29] conducted polarized neutron measurements. They found, to within experimental precision, the filed-induced form factor was not in agreement with band calculations. In fact, as shown in Figure 1.9, the experimental field-induced form factor is quite consistent with the spherical $Cu^{2+}$ 3d form factor.

We notice that the polarized neutron experiments were conducted at T = 330 K on a sample with $T_N$ = 304 K. At this temperature, although the 3D long-range order has vanished, the compound is not yet in a true paramagnetic state because the spins are still two-dimensionally correlated in the Cu-O planes [17-19]. Therefore, it is inappropriate to compare the measured magnetic response at this temperature with the band-structure calculations obtained for the paramagnetic state. We speculate this may present a dilemma in understanding the experimental field-induced magnetic form factor from the band-calculation perspective. On one hand, the true paramagnetic state can only be realized for temperatures above 1300-1400 K [24], but at these temperatures, the compound decomposes. On the other hand, the mean-field band theory is unable to account for spin correlations (or fluctuations) and, therefore, cannot be used to calculate magnetic properties in a regime where spin correlations are important.

Another interesting aspect is that the experimental antiferromagnetic form factor and field-induced form factor are not consistent among themselves. Of course, these two form factors correspond to different magnetization densities and, indeed, there is no reason to believe that they should be the same. However, such a large difference between these form factors has not been reported in the past for transition metal ions.

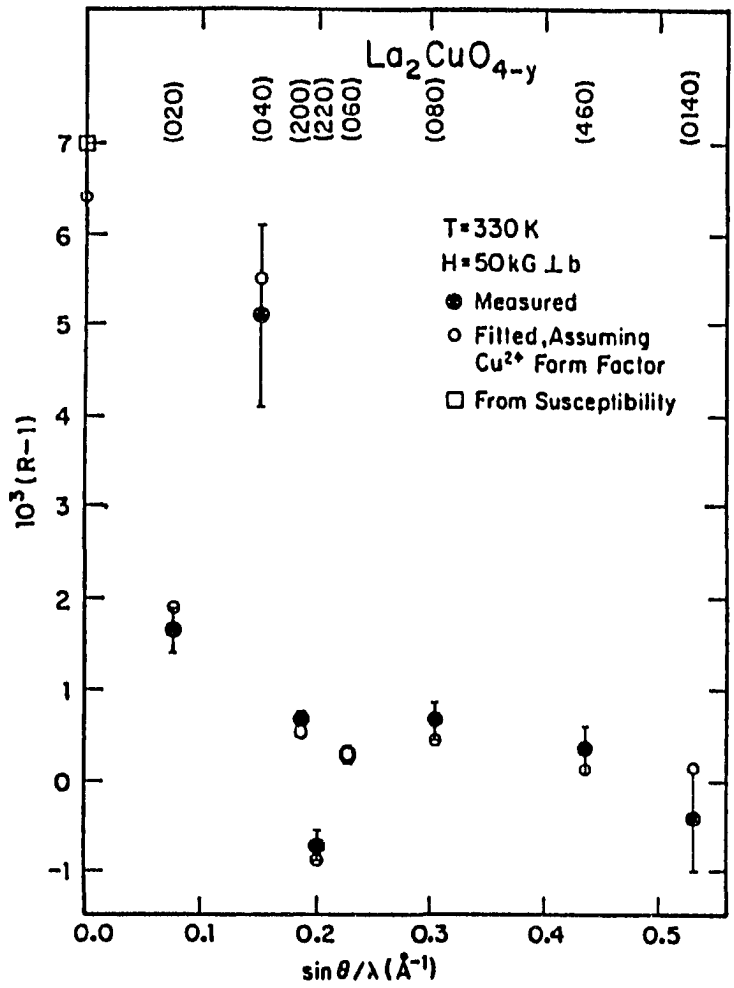


Figure 1.9 Measured field-induced response in $La_2CuO_4$. The solid circles are the experimental data. The open circles are the fitted values using the spherical $Cu^{2+}$ 3d form factor. The point in the forward direction, represented by a square, was calculated from the measured susceptibility. The indices are based on space group Cmca. (After Ref. 29)

We now return to comment on the ordered moment of $La_2CuO_4$. Notice that for the sample whose antiferromagnetic form factor was cited in Figure 1.8, the moment is quite small, only 0.3 $\mu_B$. Yamada et al. [16] found that the ordered moment varied monotonously as a function of the Néel temperature of the sample, with the maximum value (record so far) ~ 0.60±0.05 $\mu_B$ (Figure 1.10). These moments were evaluated by assuming $f(\mathbf{Q}) = 0.835$ for the (1 0 0) magnetic reflection. This value was obtained by interpolating the $K_2CuF_4$ form factor measured by Akimitsu and Ito [30]. We argue that such scaling is inappropriate. $K_2CuF_4$ is a ferromagnet and, as demonstrated by neutron diffraction [30-31] and NMR [32] measurements, exhibits considerable covalency effects between Cu and the nearest-neighbor O atoms. As a result, its magnetic form factor [30-31] is characterized by a forward peak for $\sin\theta/\lambda < 0.1$ Å$^{-1}$ followed by a plateau and a smoothly decreasing tail which approaches the appropriate $Cu^{2+}$ form factor at sufficiently high Q (Figure 1.11). The forward peak is associated with the ferromagnetic nature of the compound. Since $La_2CuO_4$ is an antiferromagnet, it is inappropriate to take the form factor of $K_2CuF_4$ for granted, particularly in the region where $\sin\theta/\lambda < 0.1$ Å$^{-1}$. In fact, if one believes that the antiferromagnetic form factor of $La_2CuO_4$ is indeed flat at low Q as suggested by Figure 1.8, one may choose to scale the data by assuming $f(\mathbf{Q}) = 1$ for the first few reflections. In this way, all moments in Figure 1.10 should scale down by a factor of 0.835/1. = 0.835. The maximum moment thus becomes 0.50±0.04 $\mu_B$. This value is still far less than that expected for a $Cu^{2+}$ ion, which is about 1.1 $\mu_B$ (assuming g ~ 2.2). It is well known that the 2D quantum spin fluctuations can reduce the moment of $Cu^{2+}$ ions. Yet spin-wave theory [33-34] shows that the reduction is only 1/3, thus the expected moment after spin fluctuations are taken into account is ~ 0.7 $\mu_B$. So where is the other 0.2 $\mu_B$?

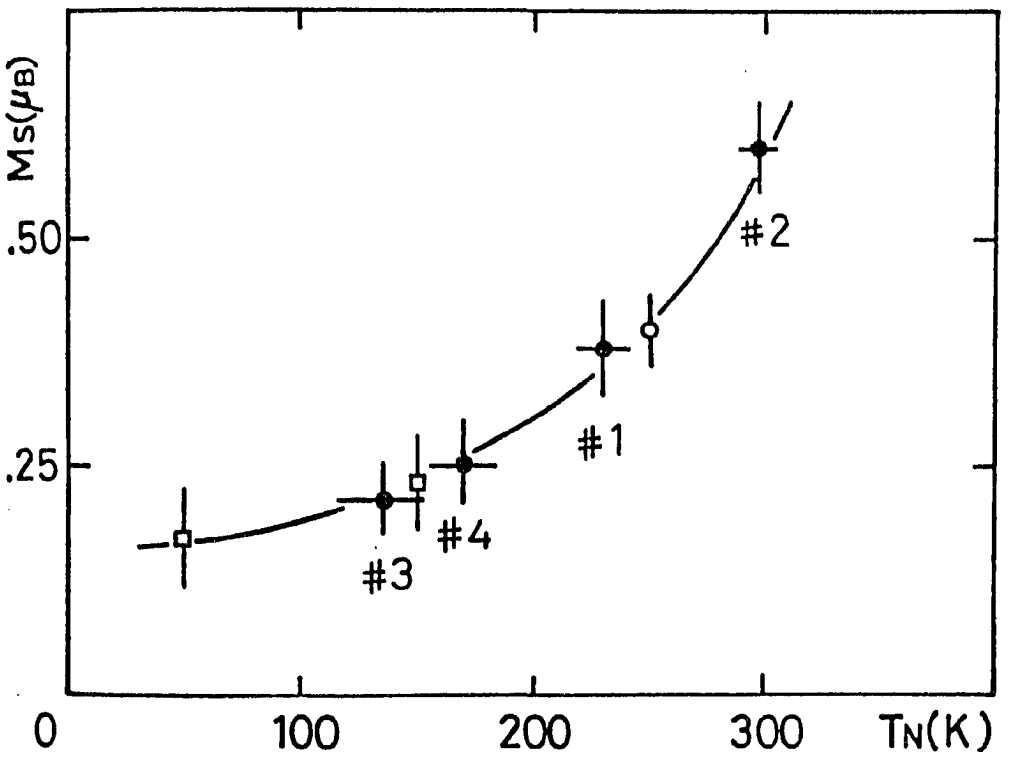


Figure 1.10 Ordered moment of $La_2CuO_4$ as a function of Néel temperature. Different symbols represent measurements by various research groups. The solid curve is a guide to the eye. (After Ref. 16)

## D. Motivation of This Study

The aim of this study was to assess the origins of the observed plateau in the antiferromagnetic form factor and the reduced moments of $La_2CuO_4$. To approach this problem, we studied two other compounds: $Sr_2CuO_2Cl_2$ and $La_2NiO_4$. $Sr_2CuO_2Cl_2$ was

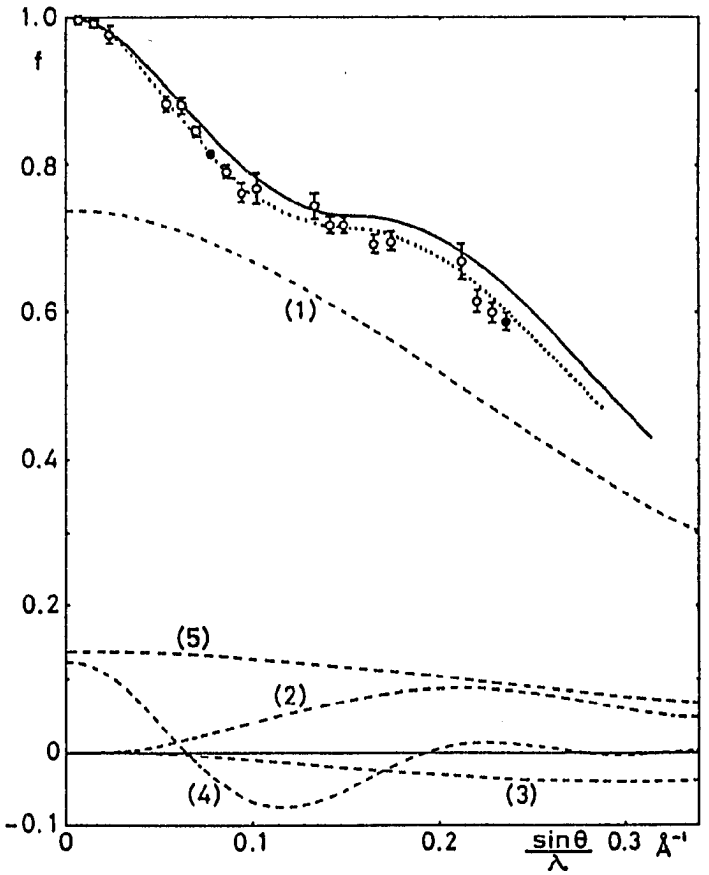


Figure 1.11 Magnetic form factor of $K_2CuF_4$. The open circles were obtained from critical scattering measurements in the paramagnetic state for Q parallel to the tetragonal c-axis and the closed circles were obtained from polarized neutron measurements. The full curve is the calculated form factor which includes covalency effects between the Cu $d_{x^2-y^2}$ and O $2p_{x,y}$ orbitals. The numbered broken lines are various components in the calculations. (After Ref. 31)

chosen here because, in this compound, the Cl atoms occupy the out-of-plane oxygen positions [35]. Studies of this sort would shed light on the role played by out-of-plane oxygen atoms. The antiferromagnetic form factor measurements on the Cu compounds are difficult because the intensities of the magnetic reflections are weak (of the order of $10^{-4}$ of a typical nuclear reflection). A much more favorable situation exists for the Ni compound, since the magnetic intensity is proportional to the square of the magnetic moment, and for a $Ni^{2+}$ ion, a moment as large as 2 $\mu_B$ is expected. Therefore, we chose $La_2NiO_4$ as another candidate.

The format of this dissertation is as follows. In Chapter II we review some fundamentals of neutron scattering theory. The experimental setup and data analysis method are described in Chapter III. In Chapters IV and V, we present the experimental data for $Sr_2CuO_2Cl_2$ and $La_2NiO_4$, respectively, and the preliminary analysis of these experimental data. In Chapter VI, we develop covalency models. We shall show that the experimental data of $Sr_2CuO_2Cl_2$ and $La_2NiO_4$ measured in the present work as well as the data of $La_2CuO_4$ measured by Freltoft et al. [28] can be reasonably understood in terms of covalency models.

# II. FUNDAMENTALS OF NEUTRON SCATTERING THEORY

## A. Theoretical Framework

In this section, we shall proceed to outline the basic formulas for calculating neutron scattering cross sections. Detailed derivations are covered in standard textbooks [36-38] and will not be repeated here.

### 1. Neutron scattering cross section

Consider a simple neutron scattering experiment schematically shown in Figure 2.1. Suppose we have a monochromatic neutron beam with a wave vector $\mathbf{k}_0$ incident on a sample and scattered to a final state with a wave vector $\mathbf{k}_1$. (Throughout this dissertation, we shall use subscripts 0 and 1 to denote the initial and final state, respectively.) The scattering intensity is characterized by a *double differential cross section* defined as

$$\frac{d^2\sigma}{d\Omega dE} = \frac{C}{\Phi N (\Delta\Omega) (\Delta E)}, \qquad (2.1)$$

where C is the count rate for a given interval $\Delta E$ of the neutron energy transfer, $\Phi$ the flux of the incident neutron beam, N the number of scattering units in the sample, and $\Delta\Omega$ the solid angle subtended by the detector towards the sample. Integrating over all energy transfer, we obtain the *differential cross section*

$$\frac{d\sigma}{d\Omega} = \frac{C}{\Phi N (\Delta\Omega)}. \qquad (2.2)$$

Suppose the incident neutrons interact via a potential V with the scattering system whose quantum state is specified by an index $\lambda$. Given the validity of the Born approximation, the count rate C (number of transitions per unit time) can be evaluated through the transition matrix element using *Fermi's Golden Rule*. Substituting the expression of C into Equation (2.1), we obtain

$$\left(\frac{d^2\sigma}{d\Omega dE}\right)_{k_0,\lambda_0 \to k_1,\lambda_1} = \frac{1}{N}\left(\frac{k_1}{k_0}\right)\left(\frac{m}{2\pi\hbar^2}\right)\cdot$$

$$\cdot \left|\langle \mathbf{k}_0\,\lambda_0 \,|\, V \,|\, \mathbf{k}_1\,\lambda_1 \rangle\right|^2 \cdot \delta\left[(E_0 - E_1) + (E_{\lambda_0} - E_{\lambda_1})\right] , \qquad (2.3)$$

where m is the neutron mass.

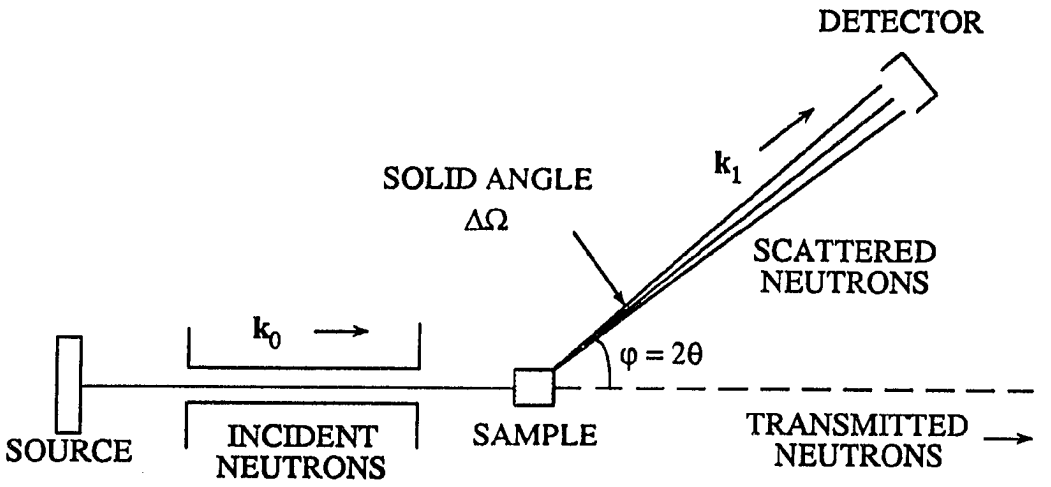


Figure 2.1 A schematic diagram of a neutron scattering experiment. (Adapted from Ref. 39)

To include all possible scattering processes, we must sum (2.3) over all the final states ($\lambda_1$) and average the sum over all the initial states ($\lambda_0$), which occur with a probability, say, $p_{\lambda_0}$. In addition, the spin states of neutrons must also be properly included. Denote the spin states by $\sigma$ and the corresponding probability distribution by $p_\sigma$. The double differential cross section then becomes

$$\left(\frac{d^2\sigma}{d\Omega dE}\right)_{k_0,\sigma_0,\lambda_0 \to k_1,\sigma_1,\lambda_1} = \frac{1}{N}\left(\frac{k_1}{k_0}\right)\left(\frac{m}{2\pi\hbar^2}\right)\sum_{\lambda_0} p_{\lambda_0}\sum_{\sigma_0} p_{\sigma_0}\cdot$$

$$\cdot \left|\langle \mathbf{k}_0\,\sigma_0\,\lambda_0|V|\mathbf{k}_1\,\sigma_1\,\lambda_1\rangle\right|^2 \cdot \delta\left[(E_0-E_1)+(E_{\lambda_0}-E_{\lambda_1})\right] . \qquad (2.4)$$

In the following context, we shall omit the subscripts on the left hand side for convenience. Equation (2.4) is called the "master formula" which provides a basis to relate the experimental observations with the physical properties of the scattering system. For thermal neutrons, $|\mathbf{k}\rangle$ is simply a plane wave. Thus, the key element to evaluate (2.4) lies in finding the explicit expressions for V and $|\lambda\rangle$.

2. Nuclear scattering

We consider a collection of atoms whose positions are specified by vectors $\mathbf{R}_j$. In general, the nuclear scattering potential is very difficult to calculate. But for the low-energy thermal neutrons, the scattering potential is well approximated by the so-called *Fermi pseudopotential*,

$$V_j(\mathbf{r}) = \frac{2\pi\hbar^2}{m} b_j\,\delta(\mathbf{r}-\mathbf{R}_j) , \qquad (2.5)$$

where $b_j$ is called the (nuclear) *scattering amplitude* [38] or *scattering length.* Such a scattering potential corresponds to a constant differential cross section. In fact, it is easy to show

$$\frac{d\sigma}{d\Omega} = b_j^2 \quad . \tag{2.6}$$

The total scattering potential is simply the superposition of $V_j$'s.

To facilitate the calculations in (2.4), in many cases, an integral representation of the δ-function is preferred. In this way, with the individual scattering potential given by (2.5), the double differential cross section can be written in a more concise form

$$\left(\frac{d^2\sigma}{d\Omega dE}\right) = \left(\frac{k_1}{k_0}\right)\left(\frac{m}{2\pi\hbar^2}\right)\sum_{jj'} b_j\, b_{j'} \cdot$$

$$\cdot \int_{-\infty}^{\infty} \left\langle \exp\left\{-i\mathbf{Q}\cdot \mathbf{R}_j(0)\right\} \exp\left\{i\mathbf{Q}\cdot \mathbf{R}_{j'}(t)\right\} \right\rangle \exp(-iEt/\hbar)\, dt \quad . \tag{2.7}$$

In this expression,

$$E = E_1 - E_0$$

is the energy transfer of neutrons, $\mathbf{R}_j(t)$ is the time-dependent Heisenberg operator defined by

$$\mathbf{R}_j(t) = \exp(-iHt/\hbar)\mathbf{R}_j \exp(iHt/\hbar) \quad , \tag{2.8}$$

where H is the Hamiltonian of the scattering system, and < > represents the thermal average of the expectation value in the initial states,

$$\langle\ \rangle = \sum_{\lambda_0} p_{\lambda_0} \langle \lambda_0 |\ \ | \lambda_0 \rangle \quad . \tag{2.9}$$

Assume the scattering system consists of a single element. For such a simple system, the scattering amplitude may vary from one nucleus to another owing to the orientation of the nuclear spin or the presence of isotope or both. To account for the distribution of the scattering amplitude, the product $b_j \cdot b_{j'}$ must be averaged. Assuming there is no correlation between the scattering amplitudes of different nuclei, we have

$$\overline{b_j\, b_{j'}} = (\bar{b})^2 \ , \qquad \text{if } j \neq j', \tag{2.10}$$

and

$$\overline{b_j\, b_{j'}} = \overline{b^2} \ , \qquad \text{if } j = j', \tag{2.11}$$

or in general

$$\overline{b_j\, b_{j'}} = (\bar{b})^2 - \delta_{jj'}\left(\overline{b^2} - (\bar{b})^2\right) \quad . \tag{2.12}$$

Now Equation (2.7) is divided into two terms: the first term is known as *coherent* and second term as *incoherent* scattering cross section. Thus,

$$\left(\frac{d^2\sigma}{d\Omega dE}\right)_{coh} = \left(\frac{k_1}{k_0}\right)\left(\frac{1}{2\pi\hbar}\right)\sum_{jj'} (\bar{b})^2 \cdot$$

$$\cdot \int_{-\infty}^{\infty} \left\langle \exp\left\{-i\mathbf{Q}\cdot\mathbf{R}_j(0)\right\} \exp\left\{i\mathbf{Q}\cdot\mathbf{R}_{j'}(t)\right\} \right\rangle \exp(-iEt/\hbar)\, dt \ , \tag{2.13}$$

and

$$\left(\frac{d^2\sigma}{d\Omega dE}\right)_{inc} = \left(\frac{k_1}{k_0}\right)\left(\frac{1}{2\pi\hbar}\right)\sum_{j} \left(\overline{b^2} - (\bar{b})^2\right) \cdot$$

$$\cdot \int_{-\infty}^{\infty} \left\langle \exp\left\{-i\mathbf{Q}\cdot \mathbf{R}_j(0)\right\} \exp\left\{i\mathbf{Q}\cdot \mathbf{R}_j(t)\right\} \right\rangle \exp(-iEt/\hbar)\, dt \quad . \tag{2.14}$$

Equations (2.13) and (2.14) can be easily generalized to scattering systems containing more than one element. In these circumstances, it is convenient to replace the subscript j in the above equations with a double-index ($l$ d), where d indicates the type of element. With this notation, the coherent and incoherent scattering cross sections are respectively given by

$$\left(\frac{d^2\sigma}{d\Omega dE}\right)_{coh} = \left(\frac{k_1}{k_0}\right)\left(\frac{1}{2\pi\hbar}\right) \sum_{\substack{l\,d \\ l'\,d'}} \bar{b}_d \bar{b}_{d'} \cdot$$

$$\cdot \int_{-\infty}^{\infty} \left\langle \exp\left\{-i\mathbf{Q}\cdot \mathbf{R}_{l\,d}(0)\right\} \exp\left\{i\mathbf{Q}\cdot \mathbf{R}_{l'\,d'}(t)\right\} \right\rangle \exp(-iEt/\hbar)\, dt \quad , \tag{2.15}$$

and

$$\left(\frac{d^2\sigma}{d\Omega dE}\right)_{inc} = \left(\frac{k_1}{k_0}\right)\left(\frac{1}{2\pi\hbar}\right) \sum_{l\,d} \left(\overline{b_d^2} - (\bar{b}_d)^2\right) \cdot$$

$$\cdot \int_{-\infty}^{\infty} \left\langle \exp\left\{-i\mathbf{Q}\cdot \mathbf{R}_{l\,d}(0)\right\} \exp\left\{i\mathbf{Q}\cdot \mathbf{R}_{l\,d}(t)\right\} \right\rangle \exp(-iEt/\hbar)\, dt \quad . \tag{2.16}$$

3. Magnetic scattering

Apart from the nuclear scattering described above, there is also magnetic scattering arising from the interaction between the magnetic moments of the incident neutrons and the magnetic field due to unpaired electrons in an atom. In general, the magnetic field contains two terms, the first arises from the spin and the second from the orbital motion of unpaired electrons. Unlike the nuclear interaction, the exact expression for the

magnetic interaction is obtainable by simply following the standard electromagnetism [36-37]. In fact, it is found that $\langle \mathbf{k}_0 | V_m | \mathbf{k}_1 \rangle$ can be written in a rather simple form,

$$\langle \mathbf{k}_0 | V_m | \mathbf{k}_1 \rangle = \frac{1}{2} \gamma r_0 \sigma \cdot \mathbf{M}_\perp(\mathbf{Q}) \quad , \tag{2.17}$$

where

$$r_0 = \frac{e^2}{m_e c^2}$$

is the classical radius of an electron and has the value $0.2818 \times 10^{-12}$ cm, $\gamma = 1.91$ is the gyromagnetic ratio of a neutron, $\sigma$ is the neutron spin operator, and $\mathbf{M}_\perp(\mathbf{Q})$ is the vector projection of $\mathbf{M}(\mathbf{Q})$, the Fourier transform of the total magnetization density $\mathbf{M}(\mathbf{r})$, on to the plane perpendicular to the scattering vector. An important feature of (2.17) is that the scattering intensity is related to the Fourier transform of the total magnetization density. Thus, by performing a Fourier transform, one can experimentally determine the magnetization distribution of the scattering units. In addition, the dependence on $\sigma$ allows the experimenter to separate the magnetic scattering from the nuclear scattering by utilizing polarization analysis, for the latter is polarization independent.

In the following, we shall restrict our discussions to systems of localized moments. Furthermore, we shall assume dipole approximation, i.e., the spatial extent of the electron wavefunctions is much less than $|\mathbf{Q}|^{-1}$, as is often satisfied in practice. With those conditions and in unpolarized neutron experiments, $\mathbf{M}(\mathbf{Q})$ can be effectively written as [40]

$$\mathbf{M}(\mathbf{Q}) = \mu f(\mathbf{Q}) \quad , \tag{2.18}$$

where $\mu$ is the total magnetic moment and $f(\mathbf{Q})$ is the normalized magnetic form factor of the atom, i.e., $f(0) = 1$. In Chapter VI, we shall discuss in detail how to compare the observed $f(\mathbf{Q})$ with theoretical atomic calculations. By analogy with (2.7), we may obtain the double differential cross section for a magnetic scattering process,

$$\left(\frac{d^2\sigma}{d\Omega dE}\right) = \left(\frac{k_1}{k_0}\right)\left(\frac{1}{2\pi\hbar}\right)\sum_{jj'}\left(\frac{1}{2}\gamma r_0 f_j(\mathbf{Q})\right)\left(\frac{1}{2}\gamma r_0 f_{j'}(\mathbf{Q})\right)^* \cdot \sum_{\alpha\beta}\left(\delta_{\alpha\beta} - \hat{Q}_\alpha\hat{Q}_\beta\right)\cdot$$

$$\cdot \int_{-\infty}^{\infty}\left\langle \exp\left\{-i\mathbf{Q}\cdot\mathbf{R}_j(0)\right\}\mu_j^\alpha(0)\exp\left\{i\mathbf{Q}\cdot\mathbf{R}_{j'}(t)\right\}\mu_{j'}^\beta(t)\right\rangle \exp(-iEt/\hbar)\,dt \quad . \quad (2.19)$$

The extra geometric factor $\left(\delta_{\alpha\beta} - \hat{Q}_\alpha\hat{Q}_\beta\right)$, $\alpha$=x,y,z, comes from the evaluation of the product $\sigma\cdot\mathbf{M}_\perp(\mathbf{Q})$. Usually, the orientation of magnetic moments introduces a very small correction to the interatomic forces hence on the motion of the nuclei. Therefore, to a good approximation, the motion of the magnetic moments can be decoupled from the motion of the nuclei, and the thermal average can be evaluated separately. This gives

$$\left(\frac{d^2\sigma}{d\Omega dE}\right) = \left(\frac{k_1}{k_0}\right)\left(\frac{1}{2\pi\hbar}\right)\sum_{jj'}\left(\frac{1}{2}\gamma r_0 f_j(\mathbf{Q})\right)\left(\frac{1}{2}\gamma r_0 f_{j'}(\mathbf{Q})\right)^* \cdot \sum_{\alpha\beta}\left(\delta_{\alpha\beta} - \hat{Q}_\alpha\hat{Q}_\beta\right)\cdot$$

$$\cdot \int_{-\infty}^{\infty}\left\langle \exp\left\{-i\mathbf{Q}\cdot\mathbf{R}_j(0)\right\}\exp\left\{i\mathbf{Q}\cdot\mathbf{R}_{j'}(t)\right\}\right\rangle\left\langle \mu_j^\alpha(0)\,\mu_{j'}^\beta(t)\right\rangle \exp(-iEt/\hbar)\,dt \quad . \quad (2.20)$$

Recall that in arriving at (2.20), we have made four assumptions: (a) unpolarized neutron experiments; (b) localized moments; (c) dipole approximation; (d) the orientation of the magnetic moments is independent of the motion of the nuclei. Caution must be taken if one of the conditions is not met. For unpolarized neutron experiments, there is no

interference between the nuclear and magnetic scattering, so the total scattering cross section is simply given by the sum of (2.7) and (2.20).

## B. Bragg Scattering by Crystals

In this section, we shall discuss the scattering cross section pertinent to our measurements, i.e., the diffraction — elastic scattering — from crystalline samples.

A crystal is formed by the repetition of small units called unit-cells. Each unit-cell may contain one or more atoms. Within a unit-cell, at a given time, atoms move around their equilibrium positions due to thermal vibrations. Thus, in general, the instantaneous position of the dth atom in unit-cell $l$ is given by

$$\mathbf{R}_{l\,d} = \mathbf{R}_l + \mathbf{r}_d + \mathbf{u}_{l\,d} \,, \tag{2.21}$$

where $\mathbf{R}_l + \mathbf{r}_d$ is the equilibrium position and $\mathbf{u}_{l\,d}$ is the displacement from the equilibrium position (Figure 2.2). Inserting (2.21) in (2.15), we obtain,

$$\left(\frac{d^2\sigma}{d\Omega dE}\right)_{coh} = \left(\frac{k_1}{k_0}\right)\left(\frac{1}{2\pi\hbar}\right)\sum_{\substack{l\,d\\ l'd'}} \bar{b}_d\,\bar{b}_{d'}\,\exp\left\{iQ\cdot\left(\mathbf{R}_{l'} + \mathbf{r}_{d'} - \mathbf{R}_l - \mathbf{r}_d\right)\right\}$$

$$\cdot\int_{-\infty}^{\infty}\left\langle \exp\left\{-iQ\cdot\mathbf{u}_{l\,d}(0)\right\}\exp\left\{iQ\cdot\mathbf{u}_{l'd'}(t)\right\}\right\rangle \exp(-iEt/\hbar)\,dt \,. \tag{2.22}$$

This is the coherent scattering cross section for all processes, both elastic and inelastic.

In a crystal, the thermal displacements of atoms constitute collective motions known as *phonons*. Assuming the interatomic forces are harmonic, i.e., the forces are linear functions of displacements, we may express the displacement $\mathbf{u}_{l\,d}$ as the superposition of *normal modes*. Given a set of force constants, the normal modes can be

determined by solving the dynamic matrix [41]. For simple systems such as *bcc* or *fcc* metals, an analytic solution may be obtained. If, for some complex systems, an analytic solution is difficult to obtain, the normal modes can always be solved numerically.

In general, $\mathbf{u}_{l\,d}(0)$ and $\mathbf{u}_{l'd'}(t)$ are correlated and the exact calculation of the thermal average $< >$ is difficult. A traditional approach is to expand the average $< >$ into a series of terms using so-called phonon expansions. The first term in the expansion is a constant and gives elastic scattering. The scattering occurs only if $\mathbf{Q} = \tau$, where $\tau$ is a reciprocal lattice vector. This leads to the familiar *Bragg's Law*

$$\lambda = 2d \sin\theta \,, \tag{2.23}$$

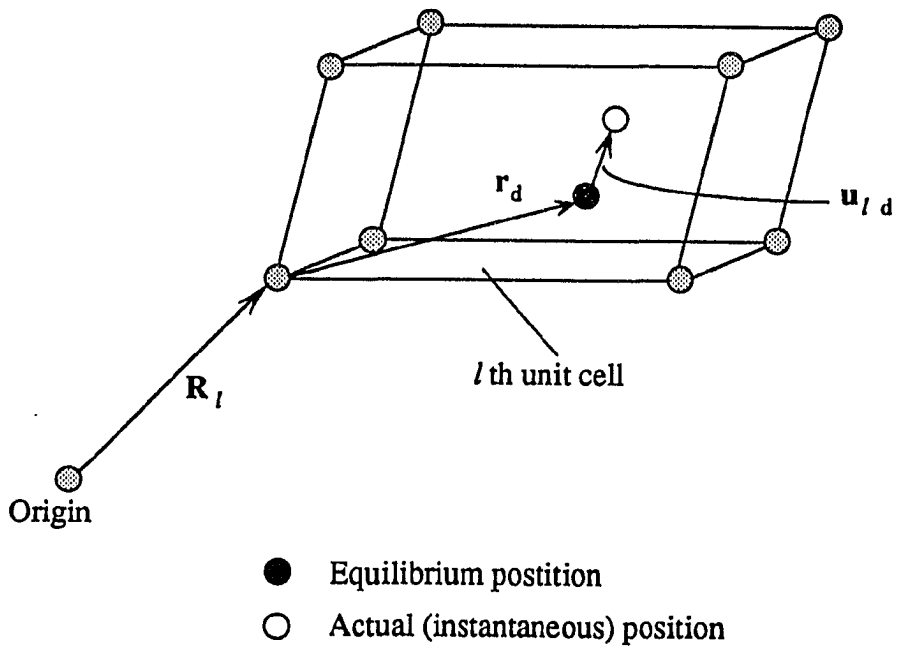


Figure 2.2 The position vector of the atom ($l$, d) in a crystal. (Adapted from Ref. 37)

where $d$ is the spacing between the reflection planes, thus the coherent elastic scattering is simply *Bragg* scattering. The second term, which contains phonon frequency $\omega$ and wave vector $\mathbf{q}$, gives one-phonon inelastic scattering. The scattering occurs only when both $\mathbf{Q} = \tau + \mathbf{q}$ and $E = \hbar\omega$ are satisfied. This leads to peaks in the inelastic scattering scans and measurements of this kind can be used to determine the *phonon dispersion curves*. The third and higher terms are multi-phonon scattering, which usually just add to the background scattering. The cross sections for these scattering processes decrease rapidly as the order increases.

If we are only concerned with the elastic scattering process, there is an alternative to evaluate the thermal average $\langle\ \rangle$ by taking time $t \rightarrow \infty$. In this regime, we are probing the *static* order. Obviously, as $t \rightarrow \infty$, $\mathbf{u}_{l'd'}(t)$ will not remember the influence from $\mathbf{u}_{l\,d}(0)$. Therefore, there will be no correlation between them, and the thermal average $\langle\ \rangle$ can be evaluated separately,

$$\left\langle \exp\left\{-i\mathbf{Q}\cdot \mathbf{u}_{l\,d}(0)\right\} \exp\left\{i\mathbf{Q}\cdot \mathbf{u}_{l'd'}(t)\right\} \right\rangle$$

$$= \left\langle \exp\left\{-i\mathbf{Q}\cdot \mathbf{u}_{l\,d}(0)\right\} \right\rangle \cdot \left\langle \exp\left\{i\mathbf{Q}\cdot \mathbf{u}_{l'd'}(t)\right\} \right\rangle . \qquad (2.24)$$

In the harmonic approximation, it can be shown [36-37]

$$\left\langle \exp\left\{i\mathbf{Q}\cdot \mathbf{u}_{l\,d}(t)\right\} \right\rangle = \exp\left\{ \frac{1}{2} \left\langle \left(i\mathbf{Q}\cdot \mathbf{u}_{l\,d}(t)\right)^2 \right\rangle \right\}$$

$$= \exp\left\{ -\frac{1}{2} \left\langle \left(\mathbf{Q}\cdot \mathbf{u}_{l\,d}(t)\right)^2 \right\rangle \right\} . \qquad (2.25)$$

The average $\langle(\mathbf{Q}\cdot\mathbf{u}_{l\,d}(t))^2\rangle$ reflects the mean-squares thermal displacement along the direction of the scattering vector. Apparently, it does not vary with time and, for a crystal lattice, is independent of index $l$ [36-37]. Denote it by $e^{-W_d}$, known as the Debye-Waller

factor [42], and notice that the integrand now is a constant. Equation (2.23) then becomes

$$\left(\frac{d^2\sigma}{d\Omega dE}\right)_{coh} = \left(\frac{k_1}{k_0}\right)\sum_{\substack{l\,d\\ l'd'}} \bar{b}_d\,\bar{b}_{d'}\,\exp\left\{iQ\cdot\left(\mathbf{R}_{l'}+\mathbf{r}_{d'}-\mathbf{R}_l-\mathbf{r}_d\right)\right\} e^{-w_d-w_{d'}}\,\delta(E) \qquad (2.26)$$

The lattice sum can be written in the form

$$\sum_l\sum_{l'}\exp\left\{iQ\cdot\left(\mathbf{R}_{l'}-\mathbf{R}_l\right)\right\} = N\frac{(2\pi)^3}{v_0}\sum_\tau \delta(Q-\tau) \qquad (2.27)$$

where $\tau$ is a reciprocal lattice vector and $v_0$ is the volume of the unit-cell. Hence,

$$\left(\frac{d^2\sigma}{d\Omega dE}\right)_{coh} = \left(\frac{k_1}{k_0}\right)\cdot N\frac{(2\pi)^3}{v_0}\sum_\tau \delta(Q-\tau)\cdot\left|\sum_d \bar{b}_d e^{iQ\cdot r_d} e^{-w_d}\right|^2 \delta(E) \qquad (2.28)$$

It can seen that elastic scattering occurs only when $\mathbf{Q} = \tau$. In a diffraction experiment, there is no energy analyzer; scattered neutrons of all energies are collected by the detector. Integrating over the energy transfer, we obtain the differential cross section for nuclear coherent scattering,

$$\left(\frac{d\sigma}{d\Omega}\right)_{coh} = N\frac{(2\pi)^3}{v_0}\sum_\tau \delta(Q-\tau)\cdot\left|F_N(Q)\right|^2 \qquad (2.29)$$

where

$$F_N(Q) = \sum_d \bar{b}_d e^{iQ\cdot r_d} e^{-w_d} \qquad (2.30)$$

is known as the *nuclear unit-cell structure factor*. Equations (2.29) and (2.30) form the basis of neutron crystallography.

Applying the same technique, we may obtain the cross section for incoherent scattering

$$\left(\frac{d\sigma}{d\Omega}\right)_{inc} = N \sum_d \left\{\overline{b_d^2} - (\overline{b_d})^2\right\} e^{-2w_d} \quad . \tag{2.31}$$

From (2.31), we see that the elastic incoherent scattering does not lead to peaks in the reciprocal space. This is because the incoherent scattering involves the correlation of the *same* nucleus (at different times of course). As a result, the exponential phase factor cancels and there are no interference effects. In fact, the only **Q** dependence lies in the Debye-Waller factor. However, the Debye-Waller factor is quite close to unity as long as the temperature is not too high. Thus generally speaking, the elastic incoherent scattering is quite isotropic. As shall be seen later, this property can be used for calibration of the incident neutron spectrum.

For magnetic scattering, there is an additional *magnetic* correlation term to be considered [see Equation (2.20)]. Following previous practice, as $t \rightarrow \infty$, we have

$$\left\langle \mu_j^\alpha(0)\, \mu_j^\beta(t) \right\rangle = \left\langle \mu_j^\alpha(0) \right\rangle \left\langle \mu_j^\beta(t) \right\rangle \quad . \tag{2.32}$$

Assume we have a simple magnetic structure consisting of a single magnetic ion and the averaged magnetic moments are either parallel or antiparallel to an easy axis $\hat{\eta}$, i.e.,

$$\left\langle \mu_j^\alpha(t) \right\rangle = \delta_{\alpha\eta} \sigma_j \mu \quad , \tag{2.33}$$

where $\sigma_j = \pm 1$ and $\mu$ is the average *ordered* magnetic moment per magnetic ion. It follows that

$$\sum_{\alpha\beta}\left(\delta_{\alpha\beta}-\hat{Q}_\alpha\hat{Q}_\beta\right)\left\langle \mu_j^\alpha(0)\ \mu_{j'}^\beta(t)\right\rangle$$

$$=\sum_{\alpha\beta}\left(\delta_{\alpha\beta}-\hat{Q}_\alpha\hat{Q}_\beta\right)\delta_{\alpha\eta}\delta_{\beta\eta}\sigma_j\sigma_{j'}\,\mu^2$$

$$=\left(1-(\hat{Q}\cdot\hat{\eta})^2\right)\sigma_j\sigma_{j'}\,\mu^2 \quad . \tag{2.34}$$

Replace j by ($l$ d), where $l$ stands for the $l$ th *magnetic unit-cell* and d stands for the dth magnetic ion. $\sigma_j$ now changes to $\sigma_d$. Using the results of (2.25) and (2.27), and integrating over the energy transfer, we obtain

$$\left(\frac{d\sigma}{d\Omega}\right)_{mag} = N_m\frac{(2\pi)^3}{v_{0m}}\cdot\left(1-(\hat{Q}\cdot\hat{\eta})^2\right)\cdot\sum_{\tau}\delta(Q-\tau_m)\cdot|F_m(Q)|^2 \quad , \tag{2.35}$$

where

$$F_m(Q)=\frac{1}{2}\gamma r_0\,\mu f(Q)\sum_d\sigma_d e^{iQ\cdot r_d}e^{-w_d} \quad , \tag{2.36}$$

is known as the *magnetic unit-cell structure factor*. In Equations (2.35) and (2.36), all variables with the subscript m are quantities associated with the magnetic unit-cell which may be different from the nuclear unit-cell. By comparison with the nuclear unit-cell structure factor, it can be seen that the effective scattering amplitude for magnetic scattering [38] may be characterized by $p=\frac{1}{2}\gamma r_0\,\mu f(Q)$. Unlike the nuclear scattering amplitude, however, the magnetic scattering amplitude $p$ is Q dependent.

For a ferromagnet ($\sigma_d$ = 1 for all d), the magnetic unit-cell is identical to the nuclear unit-cell and the magnetic reflections appear at exactly the same positions of the nuclear Bragg reflections. For an antiferromagnet, however, the magnetic unit-cell often is different from the nuclear unit-cell and the magnetic reflections appear at positions

forbidden by the crystal structure. A typical antiferromagnetic structure is shown in Figure 2.3 for AuMn. For this compound, the magnetic moments point alternately up and down along the b-axis, thus the magnetic unit-cell doubles in this direction. The corresponding magnetic reflections are (h k+$\frac{1}{2}$ *l*) instead of (h k *l*) for the nuclear Bragg reflections.

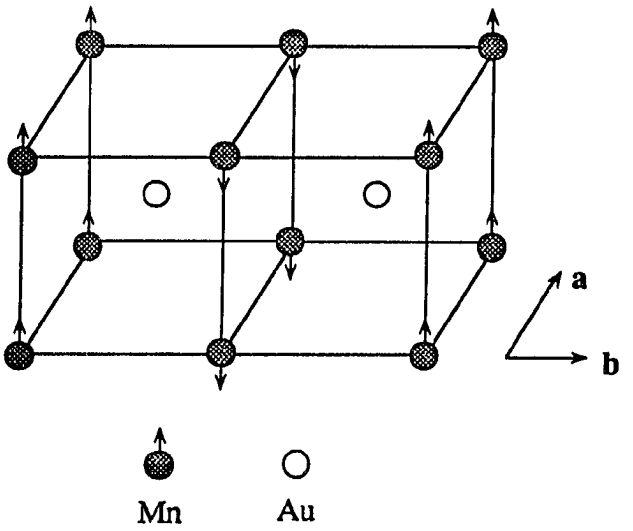


Figure 2.3 Illustration of the doubling of a magnetic unit-cell: The antiferromagnetic structure of AuMn. The magnetic moments are parallel to the c-axis. The magnetic unit-cell doubles along the b-axis. The magnetic propagation wave vector is [0 $\frac{1}{2}$ 0]. (Adapted from Ref. 38)

Without utilizing polarization analysis, there are usually two methods to identify whether the forbidden reflections are of magnetic origin. The first is to follow the temperature dependence of these reflections. Above the ordering temperature, the magnetic reflections should disappear. The second method is to examine a number of forbidden reflections over a broad Q range. For magnetic reflections, the observed structure factor, which is proportional to the magnetic form factor, should fall off at high Q values.

For convenience, we define the magnetic interaction vector [38]

$$\mathbf{q} = \hat{\mathbf{Q}}\left(\hat{\mathbf{Q}}\cdot\hat{\eta}\right) - \hat{\eta} \quad . \tag{2.37}$$

It is easy to show that

$$\left(1 - \left(\hat{\mathbf{Q}}\cdot\hat{\eta}\right)^2\right) = q^2 \quad , \tag{2.38}$$

and Equation (2.35) can be rewritten as

$$\left(\frac{d\sigma}{d\Omega}\right)_{mag} = N_m \frac{(2\pi)^3}{v_{0m}} \cdot q^2 \cdot \sum_{\tau} \delta(\mathbf{Q} - \tau_m) \cdot |F_m(\mathbf{Q})|^2 \quad . \tag{2.39}$$

In the presence of multiple magnetic domains, $q^2$ must be averaged over all magnetic domains. Thus in general,

$$\left(\frac{d\sigma}{d\Omega}\right)_{mag} = N_m \frac{(2\pi)^3}{v_{0m}} \cdot \langle q^2 \rangle \cdot \sum_{\tau} \delta(\mathbf{Q} - \tau_m) \cdot |F_m(\mathbf{Q})|^2 \quad , \tag{2.40}$$

where < > represents the average over the magnetic domains.

# III. EXPERIMENTAL METHOD AND DATA ANALYSIS

## A. Pulsed Neutron Source

There are primarily two types of neutron sources for neutron scattering study in condensed matter physics. The most widely used are the steady-state reactors which provide continuous neutron beams. The other major type of neutron source, developed rather recently in the past ten years, is the pulsed spallation source. Unlike a reactor, where neutrons are produced through a nuclear fission process, the spallation source produces neutrons through the *spallation* process when the targets (e.g., $^{238}U$) are bombarded by high-energy protons. Spallation is a violent interaction with a nucleus that results in emissions of various kinds (primarily neutrons) and numbers of light fragments. Historical developments and recent technologies of neutron sources are summarized in an excellent review article by Carpenter and Yelon [43].

Neutrons generated in both fission and spallation process are fast neutrons. They must be slowed down by moderators from energies of the order of *MeV* to energies appropriate for neutron scattering studies which are of the order of 1-100 *meV* depending on individual problems. The moderators are usually constructed from dense hydrogenous materials to take advantage of the large scattering cross section of hydrogen atoms. For a reactor source, neutrons emerging from a moderator have a Maxwellian energy distribution characterized by the temperature of the moderator. For a pulsed spallation source, there is an additional slowing-down term that rises at thermal energies and flattens out at epithermal energies (~ eV). Figure 3.1 shows the neutron energy spectrum from an ambient-temperature polyethylene moderator of the Intense Pulsed Neutron

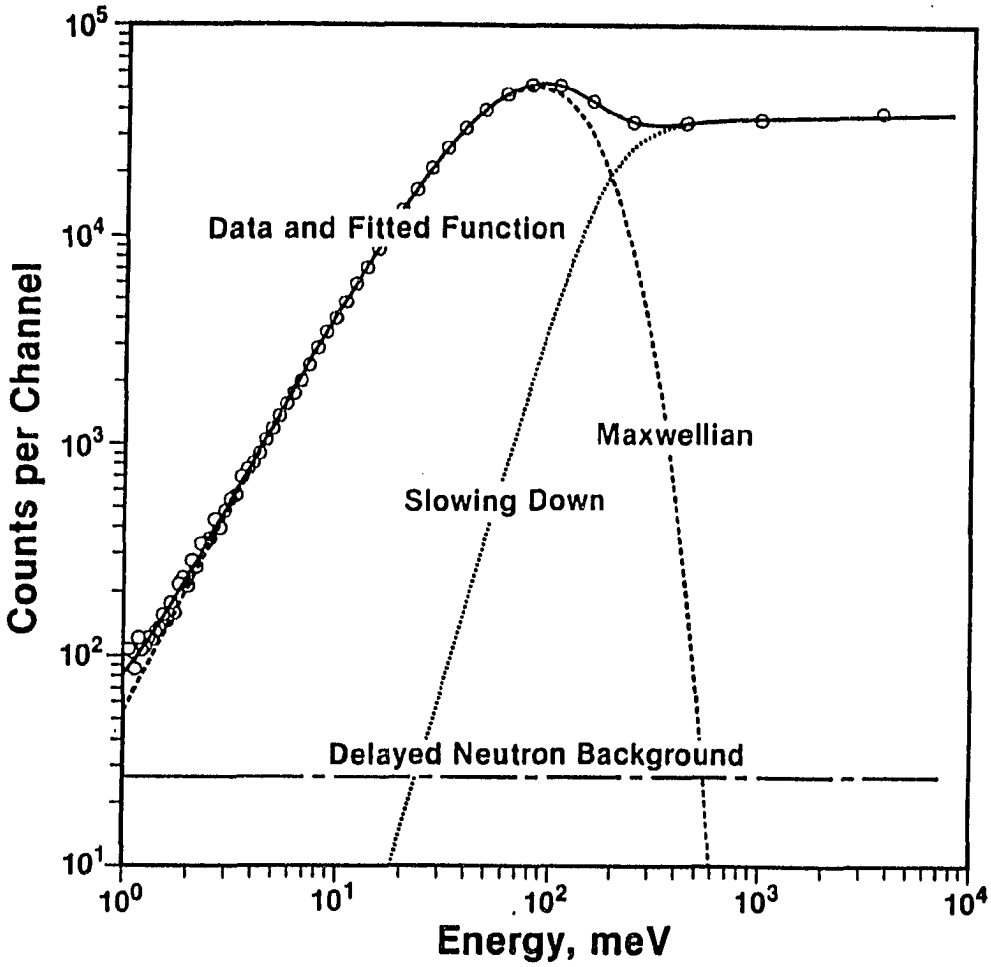


Figure 3.1 The time-averaged spectrum of neutrons from an ambient-temperature polyethylene moderator of the Intense Pulsed Neutron Source (IPNS) of Argonne National Laboratory. The Maxwellian temperature is $T_{eff}$ = 475 K (41 meV). The delayed-neutron background arises from products of fission in the $^{238}U$ target. (After Ref. 43)

Source (IPNS) of Argonne National Laboratory. The time-independent delayed neutrons result from a small amount of fission reactions accompanying the spallation process. As we shall discuss in Section B, the intense neutron flux in the epithermal region is one of the unique advantages of the pulsed spallation source over the conventional reactor source. Figure 3.2 shows a typical pulse shape as a function of time-of-flight (see Section B) for 1.6-Å neutrons from the liquid methane moderator of IPNS. As can be seen, the pulse shape is very asymmetric.

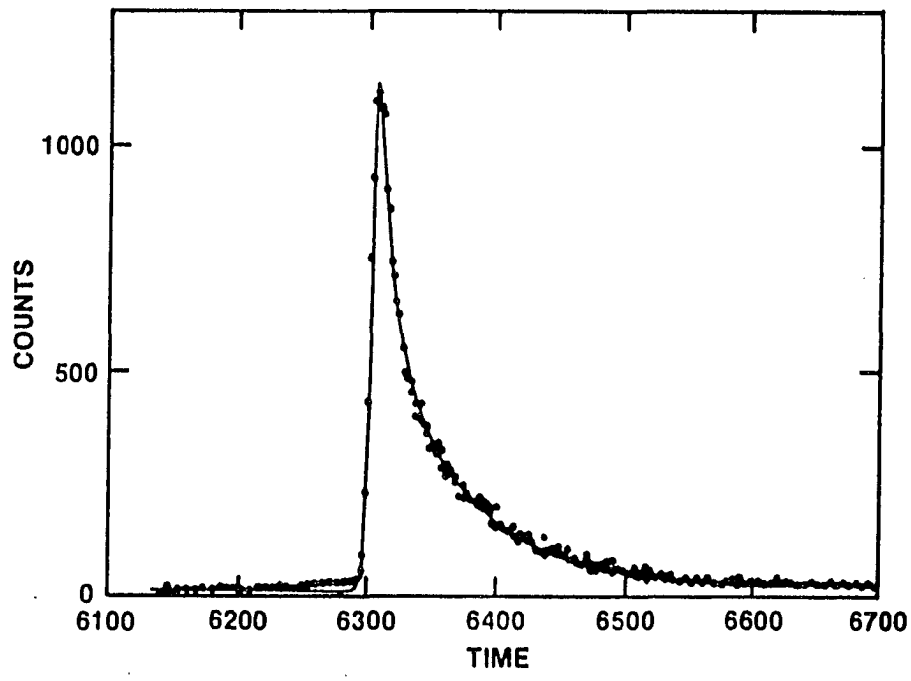


Figure 3.2 The pulse shape of 1.6-Å neutrons from a liquid methane moderator of IPNS (After Ref. 43)

## B. Time-of-flight Diffractometry

Pulsed neutron sources and reactors are complimentary in neutron scattering study. The choice of a particular instrument depends entirely on the problem of interest. Our experiments were conducted on a pulsed spallation source, the Intense Pulsed Neutron Source of Argonne National Laboratory.

Time-of-flight techniques are ideally suited for pulsed neutron sources, because the detectors can be naturally synchronized to the source for time-of-flight detection. For this reason, nearly all instruments on a pulsed neutron source employ time-of-flight techniques to give a continuous-wavelength scan at one or more fixed angles [44]. Suppose that the total flight path is L, which is conventionally measured from the moderator to the detector. It is easy to show that the neutron wavelength is proportional to its time-of-flight,

$$\lambda = \left(\frac{h}{m L}\right) t \quad . \tag{3.1}$$

A typical experimental arrangement of a time-of-flight diffractometer is schematically shown in Figure 3.3. In this diagram, a white neutron beam is incident on a sample (single-crystal or powder) and the detector is fixed at an angle $\varphi = 2\theta$. The diffraction pattern is recorded as a function of time-of-flight, which can be easily converted to $\lambda$ and other related quantities (e.g., d-spacing).

To resolve the fine details of a crystal structure, it is necessary to measure reflections at Q values as high as possible. According to Bragg's law [Equation (2.23)], this requires the use of short-wavelength or high-energy neutrons, which presents a real challenge to the reactor-based diffractometers because of the Maxwellian distribution of

the neutron energy spectrum. On a pulsed spallation neutron source, however, the slowing-down term can well meet the requirement (Figure 3.1).

Another important advantage of time-of-flight diffractometer is that the resolution is constant for reflections at all d-spacings. This can be easily realized by differentiating Bragg's law,

$$\frac{\Delta\lambda}{\lambda} = \frac{\Delta d}{d} + \cot\theta \cdot \Delta\theta \quad . \tag{3.2}$$

But

$$\frac{\Delta\lambda}{\lambda} = \frac{\Delta L}{L} \quad , \tag{3.3}$$

and since $\Delta\theta$ is dependent of $\Delta L$, we have

$$\frac{\Delta d}{d} = \sqrt{\left(\frac{\Delta L}{L}\right)^2 + \left(\cot\theta \cdot \Delta\theta\right)^2} \quad . \tag{3.4}$$

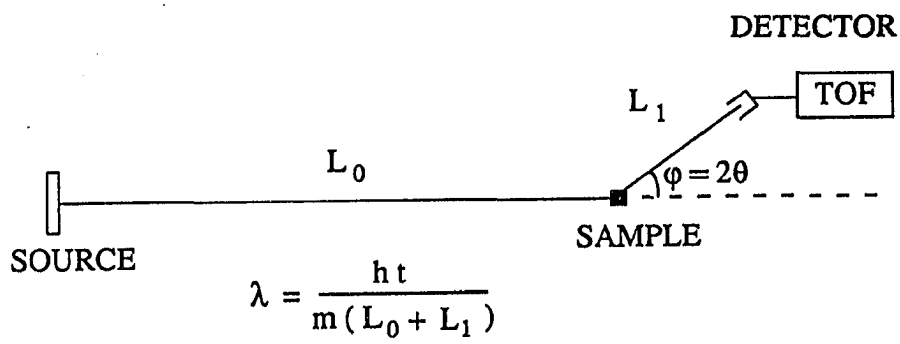


Figure 3.3 A typical experimental arrangement of a time-of-flight diffractometer (Adapted after Ref. 44)

Given a fixed scattering angle θ, we see that the resolution $\frac{\Delta d}{d}$ is a constant. Notice that $\cos\theta \rightarrow 0$ as $\theta \rightarrow 90°$. Therefore, for back scattering geometry, the resolution is dominated by $\frac{\Delta L}{L}$, which is essentially the effective moderator thickness as a fraction of the total flight path. The disadvantage of back scattering is that the maximum d-spacing that can be reached is dictated by the source period T owing to the frame-overlap problem [44],

$$d_{max} = \frac{1}{2\sin\theta} \cdot \frac{h}{m L} \cdot T \qquad (3.5)$$

To overcome this, we may combine the back scattering detectors with a set of detectors extending to low angles. The quality of the data taken at low angles are restricted, however, by the resolution which becomes progressively worse as the scattering angle decreases. Hence, some sort of compromise must be made in order to optimize the instrument.

## C. Single Crystal Diffraction and Data Analysis

### 1. Experimental method

In this work, all single-crystal diffraction experiments were conducted at IPNS using the time-of-flight single-crystal diffractometer (SCD). The diffractometer, as schematically shown in Figure 3.4, is based on the Laue method and is equipped with a large position sensitive area ($30\times30$ cm$^2$) detector. The detector consists of multiple Auger scintillators. Scintillations from neutrons absorbed in a lithium-loaded glass emit several light quanta which are later detected by more than one photomultiplier to give a

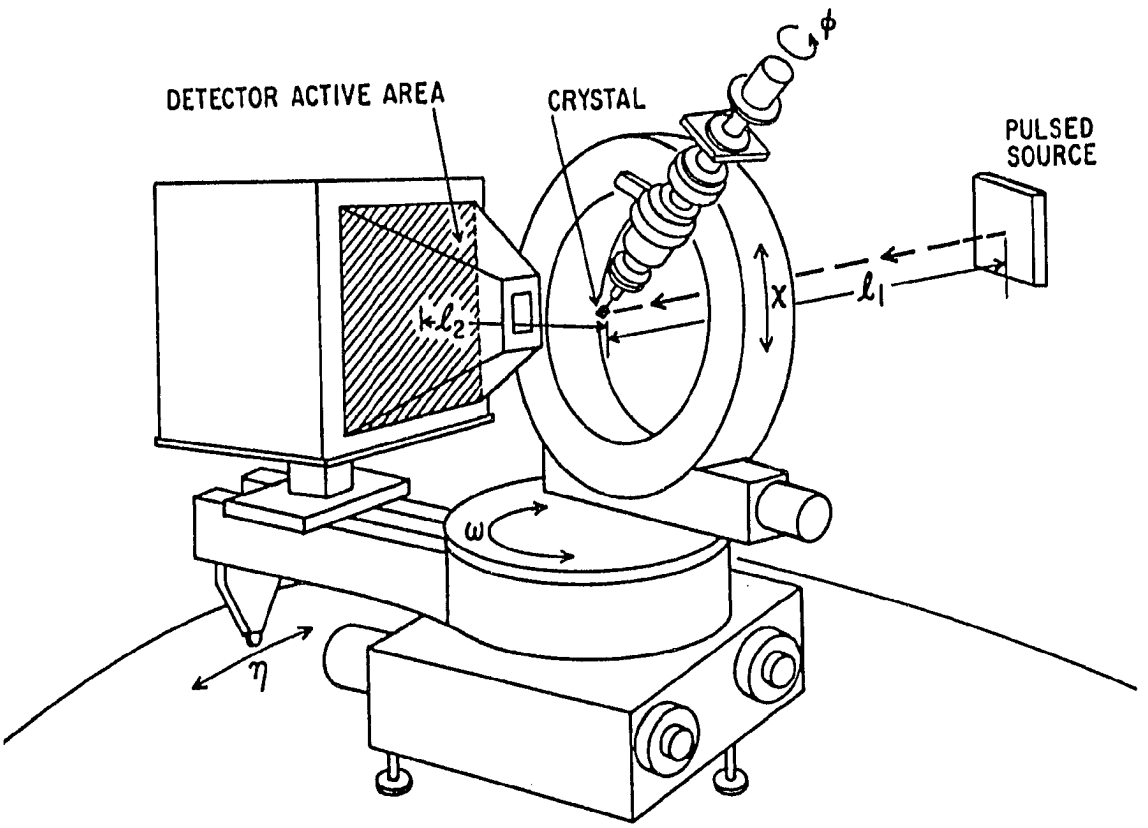


Figure 3.4 A schematic diagram of the single-crystal diffractometer IPNS. The position sensitive area (30×30 $cm^2$) detector is in the shielded enclosure on the detector arm. The flight paths for $l_1$ and $l_2$ are 950 and 25 cm, respectively. The nominal resolution is $\Delta d/d \sim 1\%$. (After Ref. 45)

positional accuracy of a few millimeters [44-45]. The detector has 85×85 cells and each cell contains 120 time-of-flight channels.

The large position-sensitive area detector coupled with the time-of-flight techniques has three distinct advantages over reactor-based diffractometers. First, because of the white incident beam used here, many diffraction peaks over a large volume of reciprocal space can be measured simultaneously with the crystal held at a fixed orientation, as illustrated in Figure 3.5. (An actual example is shown in Figure 5.5 for the (0 k *l*) reflections of $La_2NiO_4$ measured in one crystal setting.) Second, by rotating the crystal, one can measure the same diffraction peak over a wide range of neutron wavelengths. As shall be discussed in Chapter V, this capacity is very useful in assessing the possible contamination of the data by multiple Bragg scattering, which is not negligible in these experiments. Finally, there is no contamination due to higher-order reflections, because reflections of different orders are separated by time-of-flight.

2. Data reduction

In a diffraction experiment, all scattering intensities other than the coherent elastic scattering are considered background. For single-crystal experiments, rather than measuring the differential cross section directly, one measures the integrated intensity of a diffraction peak. The integrated intensity, as measured by the Laue method [36-37], is given by

$$I = \frac{N}{v_0} \varphi(\lambda) \frac{\lambda^4}{2 \sin^2\theta} |F_N(\tau)|^2 , \qquad (3.6)$$

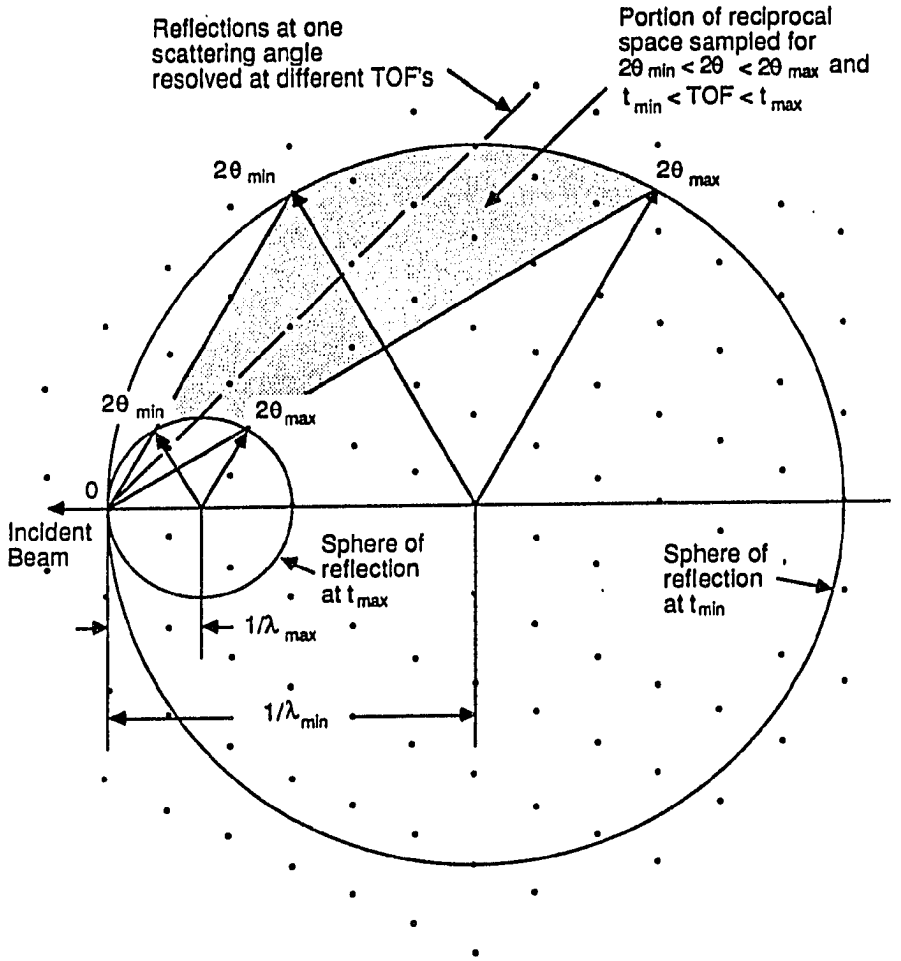


Figure 3.5 **Construction in reciprocal space to illustrate the use of multiwavelength radiation in single-crystal diffraction. The circles with radii $1/\lambda_{min}$ and $1/\lambda_{max}$ are drawn through the origin. In this two-dimensional diagram, all reciprocal lattice points within the shaded area may be sampled by a linear position-sensitive detector spanning from $2\theta_{min}$ to $2\theta_{max}$. With a position-sensitive area detector, a three-dimensional portion of reciprocal space may be sampled. (After Ref. 45)**

where $\varphi(\lambda)$ is the incident neutron spectrum normalized to total monitor counts. The intensity expressed in (3.6) is the theoretical value and subjects to a number of corrections in actual measurements, including the detector efficiency $\varepsilon(\lambda)$, the absorption correction $A(\lambda)$, and the extinction correction $y(\lambda)$. Taking these factors into account, we may write the observed integrated intensity as

$$I_{obs} = k\,\varepsilon(\lambda)\,\varphi(\lambda)\,A(\lambda)\,y(\lambda)\frac{\lambda^4}{2\sin^2\theta}|F_N(\tau)|^2 \quad , \qquad (3.7)$$

where we have used a scale factor k to replace the constant $\frac{N}{v_o}$.

Before applying Equation (3.7) to obtain the structure factors for structure refinement, one must ensure that the integrated intensities computed from the diffraction data are reliable. There are presently two computer programs [46-47], INTSCD and PEAKINT, in the SCD data analysis package that perform the integration of the 3-dimensional (x, y, and t) data profile. In INTSCD, reflections are categorized into strong and week reflections. For strong reflections, the program integrates all intensities in an ellipsoid envelope defined by some prefixed contour levels. It then proceeds to minimize $\sigma/I$ as a function of contour levels to obtain the optimum value for the integrated intensity and stores the ellipsoid parameters in a separate file. For weak reflections, the program uses the ellipsoid parameters of the nearest strong reflection to define an integration envelope and calculates the total intensity within the envelope. PEAKINT, on the other hand, uses a much simpler scheme. It simply calculates the total intensities in two fixed size envelopes (boxes); the large box (5×5×5) is for strong reflections whereas the small box (3×3×3) is for weak reflections. In both programs, intensities outside the integration envelope are treated as background.

PEAKINT is easy to use and works well for good-quality single-crystal samples [48]. For these samples, the reflections are sharp, so either set of intensities may be used to represent the true integrated intensities. In fact, for weak reflections it was shown [48] there was a significant gain in counting statistics by using the small box in PEAKINT, which leads to an overall improvement in the results of the data analysis. Problems develop, however, as we experienced in our study of $La_2NiO_4$ compound, if the peaks are broad. In those circumstances, the intensities are often underestimated and one may have to switch to the relatively sophisticated INTSCD.

The incident spectrum and detector efficiency are routinely calibrated by measuring the scattering from the polycrystalline vanadium sample. For vanadium, the coherent scattering amplitude $\bar{b} = -0.4\ fm$, as opposed to the incoherent scattering amplitude $b_i = 6.4\ fm$, so the scattering from vanadium sample is predominantly incoherent which is, as discussed before, quite isotropic for temperatures around and below the ambient-temperature. After corrected for the wave length dependent absorption (see below), the detector count rate should be proportional to the product $\varepsilon(\lambda)\cdot\varphi(\lambda)$.

Sample absorption (by nuclear capture process) is corrected using the formula

$$A(\lambda) = \exp\left\{ -\mu(\lambda) \cdot \bar{l} \right\} , \qquad (3.8)$$

where $\bar{l}$ is the total path length through the crystal and $\mu(\lambda)$ is the linear absorption coefficient. For most elements, to a good approximation, $\mu(\lambda)$ is proportional to the wavelength. Therefore, in order to correct for the absorption, we only need to know the value of the absorption coefficient for any given wavelength. The values of the linear absorption coefficients for $\lambda = 1.08$ Å are conveniently tabulated in Ref. 38.

Apart from the sample absorption of the incident beam, there may be an additional decrease in the integrated intensity of the diffracted beam due to the so-called *extinction effects*. Two sources may contribute to the extinction effects. In a *perfect* crystal (one in which the atoms are arranged in a perfectly periodic array), the extinction effects can be regarded as the destructive interference between the forward-travelling waves and the repeatedly reflected components travelling in the same direction with the opposite phase. In such a case, effective reflections take place only in a very thin layer, a penetration distance on the order of $10^{-4}$ cm. Extinction in this case is called *primary extinction.* Most crystals are, however, far from being perfect, and the ideal lattice regularity only extends over small regions known as *mosaic blocks*. These blocks are tilted slightly in orientation with respect to each other. As a result, the incident beam will be able to penetrate much more deeply into the crystal. In this case, *secondary extinction* may occur when the beam eventually reaches mosaic blocks in identical orientation with the ones through which the beam travelled at the surface. In neutron scattering experiments, this is the primary source for the extinction effects. In x-ray measurements, however, secondary extinction is negligible because the penetration capacity of x-ray beam is rather limited by the large absorption process; the dominating factor in this case is primary extinction.

The evaluation of the extinction corrections is a very complex subject. Up to now, there has not been a universally applicable theory to address this problem. Consequently, several models were proposed. These models have been incorporated into the least-squares refinement program [46] to allow simultaneous refinement of the extinction parameter along with the structural parameters. In this study, we adopt Becker-Coppen's model [49].

The accuracy of the diffractometer and the data analysis programs was demonstrated by Jauch et al. [50-52] on single-crystal samples of $Cs_3Si$ and $MnF_2$, which had been previously studied by other diffraction techniques. For both samples, the comparisons showed that very accurate crystal structure parameters can be obtained from the single crystal time-of-flight technique. In addition, it was shown [50] that severely extinguished neutron data may be corrected properly on the basis of conventional extinction models. By far, the largest crystal structure successfully refined is an organic compound with 47 independent atoms in an asymmetric unit-cell [53].

In diffraction studies of crystal structures, we use Equation (3.7) to obtain the quantity $k \cdot y(\lambda) \cdot |F_N(\tau)|^2$ for least-squares refinement. For magnetically ordered compounds, if k and the extinction parameter have been determined from the crystal structure refinement, (3.7) can be used to obtain the magnetic structure factor hence the magnetic amplitude $\mu f(\mathbf{Q})$.

## D. Powder Diffraction and Data Analysis

### 1. Experimental method

The instrument used for powder diffraction experiments is the General Purpose Powder Diffractometer (GPPD) at IPNS. Figure 3.6 shows the schematic layout of the diffractometer.

Powder samples are sealed in a sample can. The standard sample can is a cylinder, 2-inch long and 1/2-inch in diameter, and it is made of thin-wall vanadium in order to minimize the Bragg scattering from the can. However, the drawback of the vanadium can is that it can give rise to considerable background scattering because vanadium is a

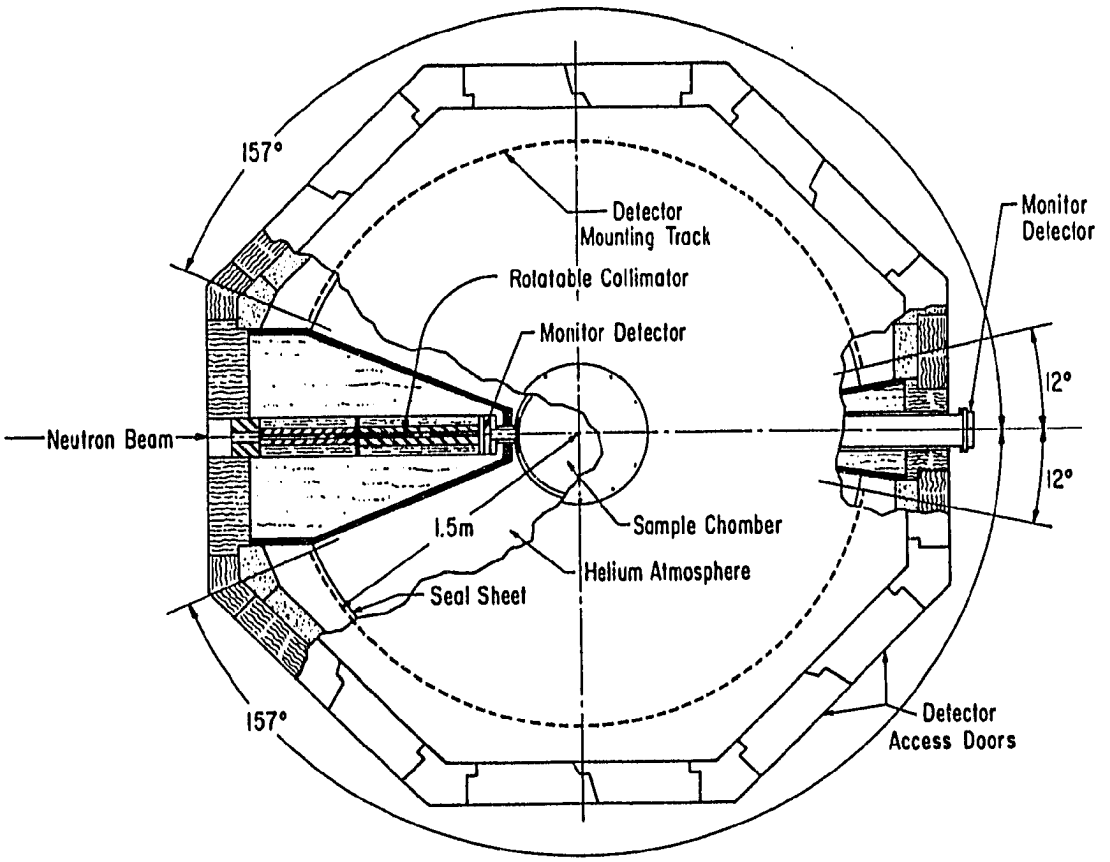


Figure 3.6 A schematic layout of the General Purpose Powder Diffractometer at IPNS. Neutrons enter from the left through a 20-m flight path. There are four detector groups centered around 30, 60, 90, and 150 degrees. The detectors within each group are electronically "binned" together using time-focusing techniques to increase count rate. (After Ref. 44)

strong incoherent scatterer. Therefore, in some experiments, particularly those searching for small peaks, sample cans made from other materials (e.g., aluminum) may be helpful.

There are four detector groups centered at 30, 60, 90, 150 degrees. To increase the detector count rate, the detectors within each group are "binned" together using time-focusing techniques [54] as described below.

From (3.1) and (2.23), we see the lattice spacing d as a function of the time-of-flight is given by

$$d = \frac{1}{2\sin\theta} \cdot \frac{h}{mL} \cdot t \quad . \tag{3.9}$$

If $L \cdot \sin\theta$ = constant, neutrons scattered from the same lattice spacing will be detected at the same time, and the diffraction patterns recorded in different detectors can be added up to improve the counting statistics while maintaining resolution nominally equal to that of the center detector. In the past, time-focusing was achieved mechanically by distributing numerous detectors on a curve satisfying $L \cdot \sin\theta$ = constant. Nowadays, with the aid of computer data acquisition systems, this can be rather easily achieved electronically by converting the actual time-of-flight to a *pseudo* time defined by

$$t^* = \frac{L_0 \sin\theta_0}{L \sin\theta} \cdot t \quad , \tag{3.10}$$

where $\theta_0$ and $L_0$ (which may be different from L) are, respectively, the reference angle and flight path of the detector group. Neutron intensities recorded by different detectors at a particular $t^*$ correspond to scattering from the same lattice spacing and, therefore, can be directly superimposed.

2. Data analysis — Rietveld refinement

The diffraction data are analyzed using the IPNS Rietveld data analysis package. Rietveld analysis is essentially a least-squares program that compares the measured profile intensity with the calculated intensity. The quality of the refinement is measured by the R factor defined by

$$R = \frac{\sum_i | I_{obs}(t_i) - I_{cal}(t_i) |}{\sum_i I_{obs}(t_i)} \quad . \tag{3.11}$$

A complete description of the method and relevant references can be found in *Users Manual For Rietveld Analysis at IPNS* [55]. The following is an outline and some remarks about the method.

The intensity observed by a detector group at a particular time-of-flight is modelled by a calculated intensity

$$I_{cal}(t) = \sum_\tau I_\tau \cdot F(\Delta_\tau) + y_b(t) \quad . \tag{3.12}$$

In this equation, the first term is the sum of the integrated intensity $I_\tau$ broadened by the peak shape function $F(\Delta_\tau)$, and the second term is the background intensity.

In powder diffraction experiments, for a specific reflection $\tau$ =(h k *l*), the wave vector of scattered neutrons $\mathbf{k}_1$ lies on a cone known as the *Debye-Scherrer* cone. If the neutron detector is located at a distance r from the sample and has an effective diameter D, it intercepts only a fraction, $D/(2\pi r \sin\theta)$, of the neutrons in the cone. After taking this fraction into account, it can be shown that the integrated intensity measured in time-of-flight powder diffraction experiments [38] is given by

$$I_\tau = \frac{N}{v_0}\varphi(\lambda)\, d^4 \sin\theta \cdot m(\tau)\,|F_N(\tau)|^2 \frac{D}{\pi r} , \qquad (3.13)$$

where $m(\tau)$ is the multiplicity of the reflection. It is important to notice that $I_\tau \propto d^4$, thus the time-of-flight diffraction method gives a favorable response for reflections of large d-spacings which would otherwise have very small intensities due to the Maxwellian distribution of the neutron spectrum at the low-energy side.

If we define

$$i_\tau = d^4\, m(\tau)\,|F_N(\tau)|^2 , \qquad (3.14)$$

(3.13) can be conveniently written as

$$I_\tau = k\,\varphi(\lambda)\, i_\tau = k\,\varphi(t_\tau)\, i_\tau , \qquad (3.15)$$

where $t_\tau$ is the center of reflection in the time-of-flight profile and k is regarded as an instrumental constant. Now we have

$$I_{cal}(t) = k \sum_\tau \left\{\varphi(t_\tau)\, i_\tau \cdot F(\Delta_\tau)\right\} + y_b(t) . \qquad (3.16)$$

In order to calculate the profile intensity, it is necessary first of all to establish the peak shape function $F(\Delta_\tau)$, where $\Delta_\tau = t - t_\tau$. This is to be contrasted to the least-squares refinement of the single-crystal data, which compares essentially the observed and calculated integrated intensity, and does not require the knowledge of the peak shape. For a time-of-flight powder diffractometer on a pulsed spallation source, $F(\Delta_\tau)$ is described by the convolution of a moderator pulse shape and a sample-dependent Gaussian distribution. The moderator pulse shape, such as the one shown in Figure 3.2, has been well established by an empirical formula [56] and the parameters in the formula are determined from the fit to the experimental data of an aluminum standard. The

parameters in the Gaussian distribution, which vary with samples, are to be refined along with the structural parameters.

As in the case of single-crystal diffraction, the incident spectrum $\varphi(t_\tau)$ is calibrated using a vanadium standard. Sometimes it is also necessary to make corrections for absorptions and extinction effects, both of which are wavelength dependent. These features constitute the main disadvantage of this technique as compared to the constant-wavelength powder diffraction based on a reactor source.

The direct assessment of the background intensities is quite difficult. Consequently, several empirical models have been proposed, each containing a few parameters to be refined in the least-squares program. Each model emphasizes a particular side of physics that may contribute to the background intensities, and is to be applied on a case-by-case basis.

Clearly, the one-dimensional powder data cannot yield more information than single crystal data. Nevertheless, it was demonstrated [57] that Rietveld refinement of high-resolution powder data can be used to obtain accurate positional parameters and reasonable temperature factors (see Chapter IV) for moderately complex structures. Of course, powder techniques are particularly valuable when large single crystals are unavailable.

# IV. NEUTRON DIFFRACTION STUDY OF $Sr_2CuO_2Cl_2$

## A. Crystal Structure

$Sr_2CuO_2Cl_2$ powder sample was prepared [58] using predried $SrCO_3$ (99.99%) $SrCl_2$, and CuO (99.99%) as starting materials. In the beginning, an intermediate material $SrCuO_2$ was synthesized by reacting stoichiometric amounts of starting materials at 925° C in air for two days with an intermediate grinding. The x-ray pure $SrCuO_2$ was then mixed with a stoichiometric amount of $SrCl_2$ and reacted for one more day, producing monophasic $Sr_2CuO_2Cl_2$.

Neutron powder diffraction measurements were performed on a 15 gram polycrystalline $Sr_2CuO_2Cl_2$ using the GPPD at IPNS. The pellet-like samples were ground into fine powders and then sealed in a thin-wall vanadium can under 1 atm of He gas at room temperature. Temperatures between 300 and 25 K were achieved using a standard closed-cycle He refrigerator. The aim of this experiment was to verify the room-temperature crystal structure proposed by Grande and Muller-Buschbaum [35], especially the location of Cl atoms, and to examine whether the compound would display the HTT-LTO structure transition.

Four data sets, at 300, 200, 65, and 25 K, were collected. At each temperature, data were collected by banks of detectors centered at scattering angles of 30°, 60°, 90°, and 150°. The data were analyzed by the Rietveld structure-refinement technique. The results of our analysis are consistent with the room temperature structure found earlier using x-ray techniques by Grande and Muller-Buschbaum [35]: $Sr_2CuO_2Cl_2$ is a body-centered tetragonal of $K_2NiF_4$ type with space group I 4/mmm. As noted in Chapter I, the structure is the same as that of (tetragonal) $La_2CuO_4$, with the oxygen atoms at the

apices of the $CuO_6$ octahedra replaced by Cl atoms. The fitting of the data by this structure was good at all temperatures. In particular, to within our experimental precision, we found no evidence between 25 and 300 K of an orthorhombic distortion from the tetragonal symmetry. The lattice parameters at the four temperatures are listed in Table I. In Figure 4.1, we plotted the lattice parameters and the unit-cell volume as a function of temperature.

Table I. Temperature dependence of the lattice parameters of $Sr_2CuO_2Cl_2$.

| | Lattice parameters (Å) | |
|---|---|---|
| Temperature (K) | a | c |
| 25 | 3.9625(1) | 15.5303(2) |
| 65 | 3.9629(1) | 15.5353(2) |
| 200 | 3.9670(1) | 15.5757(2) |
| 300 | 3.9716(1) | 15.6126(2) |

Since the coherent nuclear scattering amplitudes of the Cl and O atoms are considerably different, the neutron diffraction data are quite sensitive to the position disorder between the Cl and O atoms. Particularly sensitive to the disorder of this type are the (2 0 2) and (0 0 8) reflections. From the refinement of the site occupancies, we found that the position disorder between Cl and O atoms is quite small, (2.0±0.5)%. To verify this, we also refined the data with a fixed amount of disorder and examined the variation of the R factor and the fits to the (2 0 2) and (0 0 8) peaks as a function of the

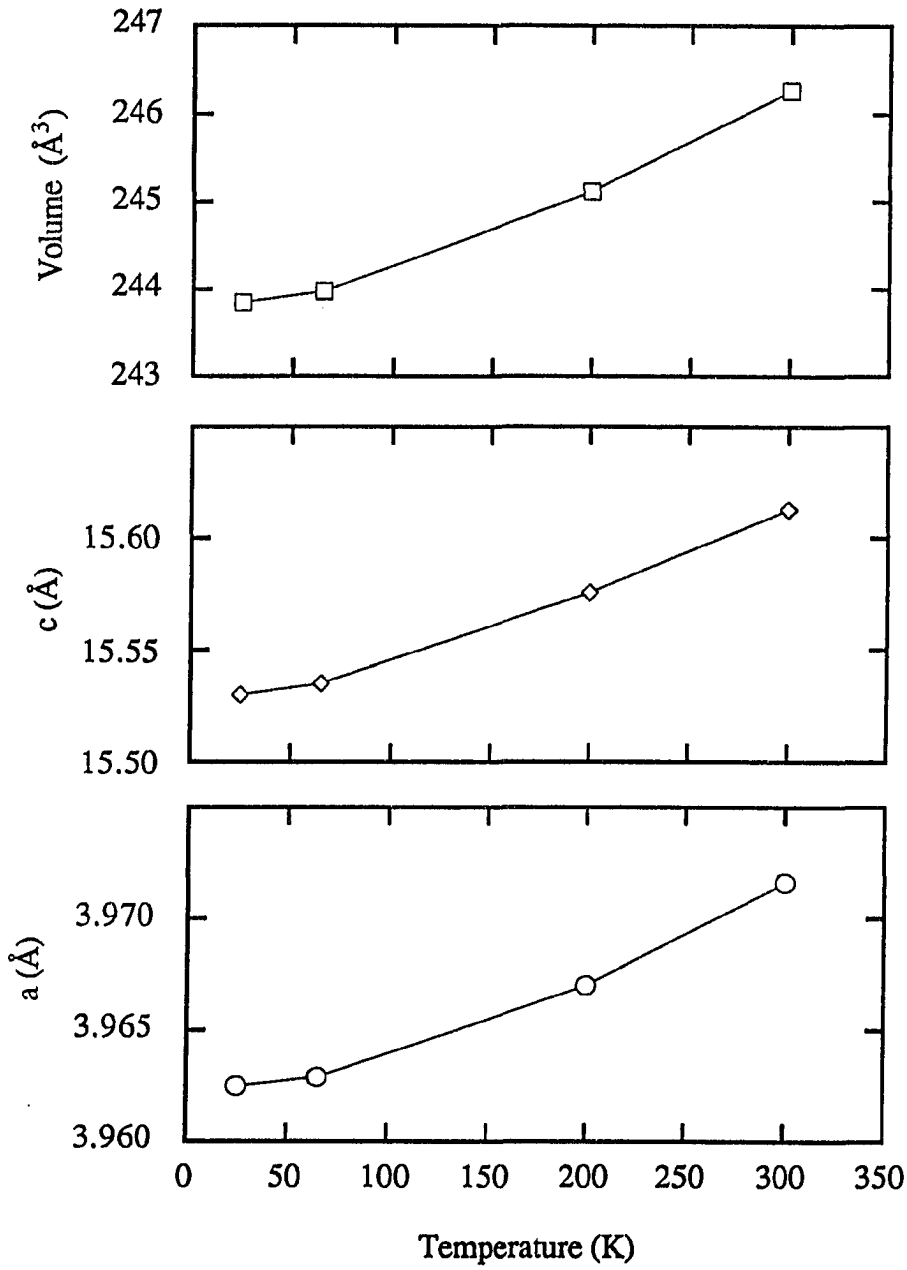


Figure 4.1 Temperature dependence of the lattice parameters and the unit-cell volume of $Sr_2CuO_2Cl_2$.

disorder. As shown in Figure 4.2, the best fits to (2 0 2) and (0 0 8) were obtained when disorder = 2.0%. At the mean time, the R factor also reached the minimum.

From our refinement we also obtained the anisotropic temperature factors $U_{ij}$ of $Sr_2CuO_2Cl_2$. These factors are the elements of a 3×3 matrix $\underline{B}$ [42] defined so that the mean-squared displacement $< u_n^2 >$ [see Equation (2.25)] of an atom along an arbitrary direction defined by the unit vector **n** is given by

$$\left\langle u_n^2 \right\rangle = \tilde{\mathbf{n}}\,\underline{B}\,\mathbf{n} \quad , \tag{4.1}$$

where $\tilde{\mathbf{n}}$ is the transpose of the column vector **n**. In the case of $Sr_2CuO_2Cl_2$, the symmetry requires that for all atoms the matrix $\underline{B}$ is diagonal ($U_{ij} = 0$ for $i \neq j$). In addition, for Sr, Cu, and Cl atoms, $U_{11} = U_{22}$.

The structure parameters obtained at 300 K for $Sr_2CuO_2Cl_2$ are listed in Table II; they are in good agreement with those obtained by Grande and Muller-Buschbaum [35]. In Appendix I, we list the structure factors calculated using these parameters. A typical fit of the data obtained at 25 K is shown in Figure 4.3. An ORTEP drawing of the structure is shown in Figure 4.4. Selected interatomic distances are listed in Table III. The temperature dependence of the thermal factors are shown in Figure 4.5. We found that the thermal motion of the Cl atoms is isotropic to within the experimental precision. This is to be contrasted with the large anisotropy of the thermal motion of the out-of-plane oxygen atoms in isostructural $La_{1.85}Sr_{0.15}CuO_4$ [59]. The thermal motion of the in-plane oxygen atoms is anisotropic in both compounds: It is smaller along the Cu-O-Cu chain than in the perpendicular directions.

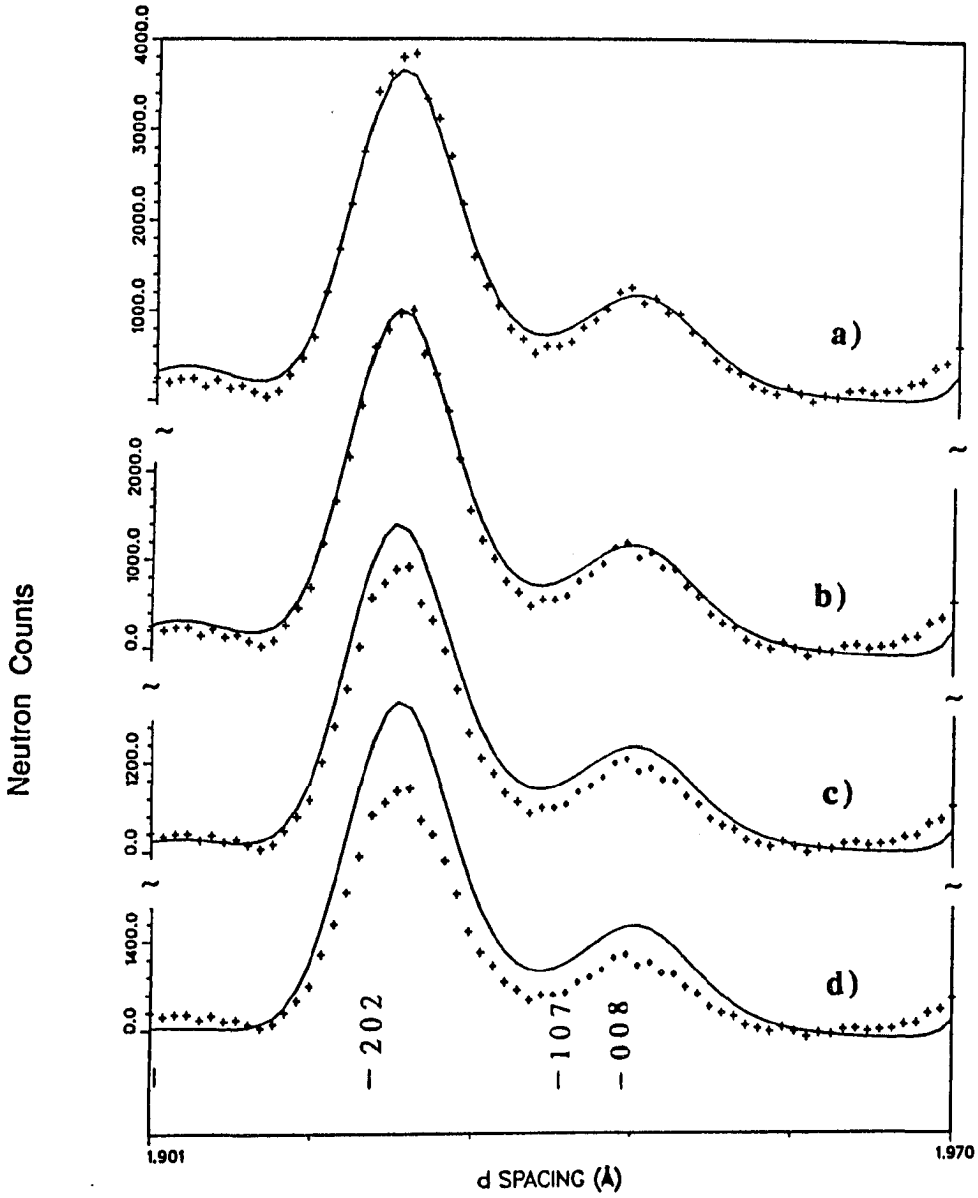


Figure 4.2 A section of the fit to the diffraction data of $Sr_2CuO_2Cl_2$ at 25 K as a function of the position disorder between Cl and O atoms. The crosses are the experimental data and the solid curves are the fits. a) No disorder, R=4.40%. b) 2.0% disorder, R=4.38%. c) 10% disorder, R=4.54%. d) 20% disorder, R=5.21%.

Table II. Structural parameters obtained for polycrystalline $Sr_2CuO_2Cl_2$ from the 90° neutron powder diffraction data set at 300 K. The lattice parameters are a = 3.9716(1) Å and c = 15.6126(2) Å, $V^{cell}$ = 246.27 $Å^3$, space group I 4/mmm, and $\rho^{calc}$ = 4.606 g/cm. Weighted profile R: 4.07%; expected R: 2.00%.

| | Atomic positions | | |
|---|---|---|---|
| Atom | *x* | *y* | *z* |
| Sr (4*e*) | 0 | 0 | 0.39259(7) |
| Cu (2*a*) | 0 | 0 | 0 |
| O (4*c*) | 0 | 1/2 | 0 |
| Cl (4*e*) | 0 | 0 | 0.18309(6) |

Cl - O disorder: (2.0±0.5)%

| | Temperature factors ($10^{-3}$ $Å^2$) | | |
|---|---|---|---|
| Atom | $U_{11}$ | $U_{22}$ | $U_{33}$ |
| Sr | 8.7(3) | 8.7(3) | 12.3(5) |
| Cu | 7.5(4) | 7.5(4) | 14.5(7) |
| O | 11.4(6) | 6.9(6) | 14.1(7) |
| Cl | 13.7(3) | 13.7(3) | 13.9(4) |

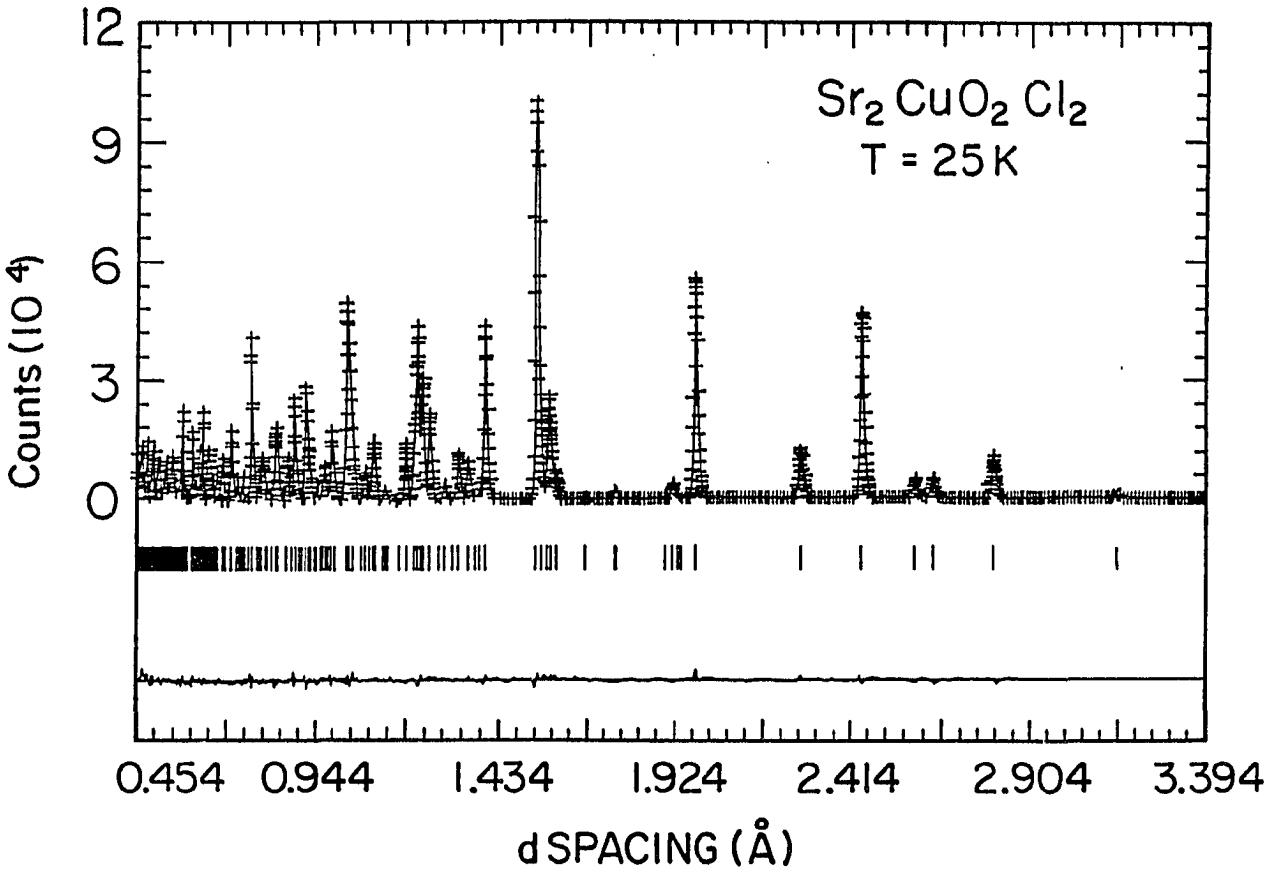


Figure 4.3 Fit to the neutron diffraction data of $Sr_2CuO_2Cl_2$ at 25 K based on I4/mmm model. The crosses are the experimental data, the solid line is the fit, and the difference plot is given at the bottom. The tick marks are the calculated peak positions.

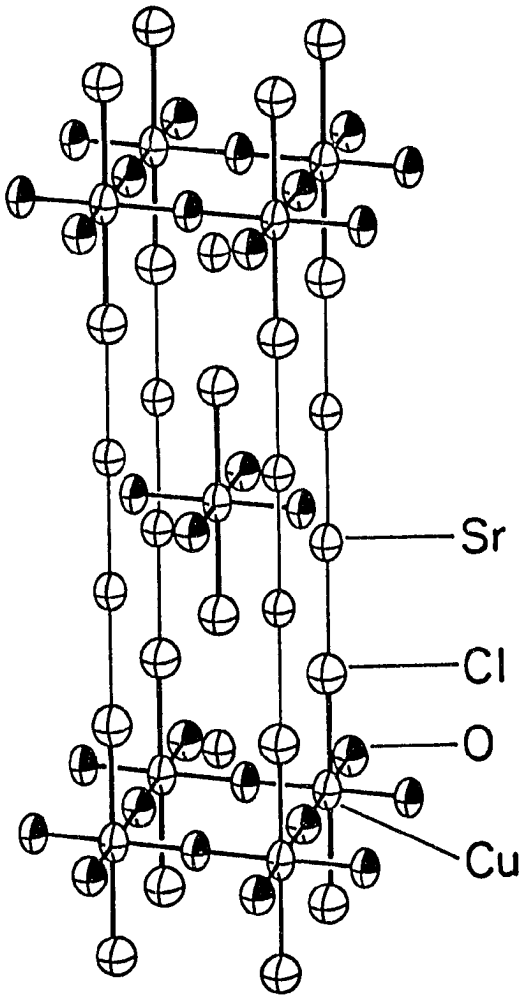


Figure 4.4 An ORTEP drawing of the crystal structure of $Sr_2CuO_2Cl_2$. The size of a thermal ellipsoid corresponds to a 99.4% probability of finding the corresponding atom within that ellipsoid.

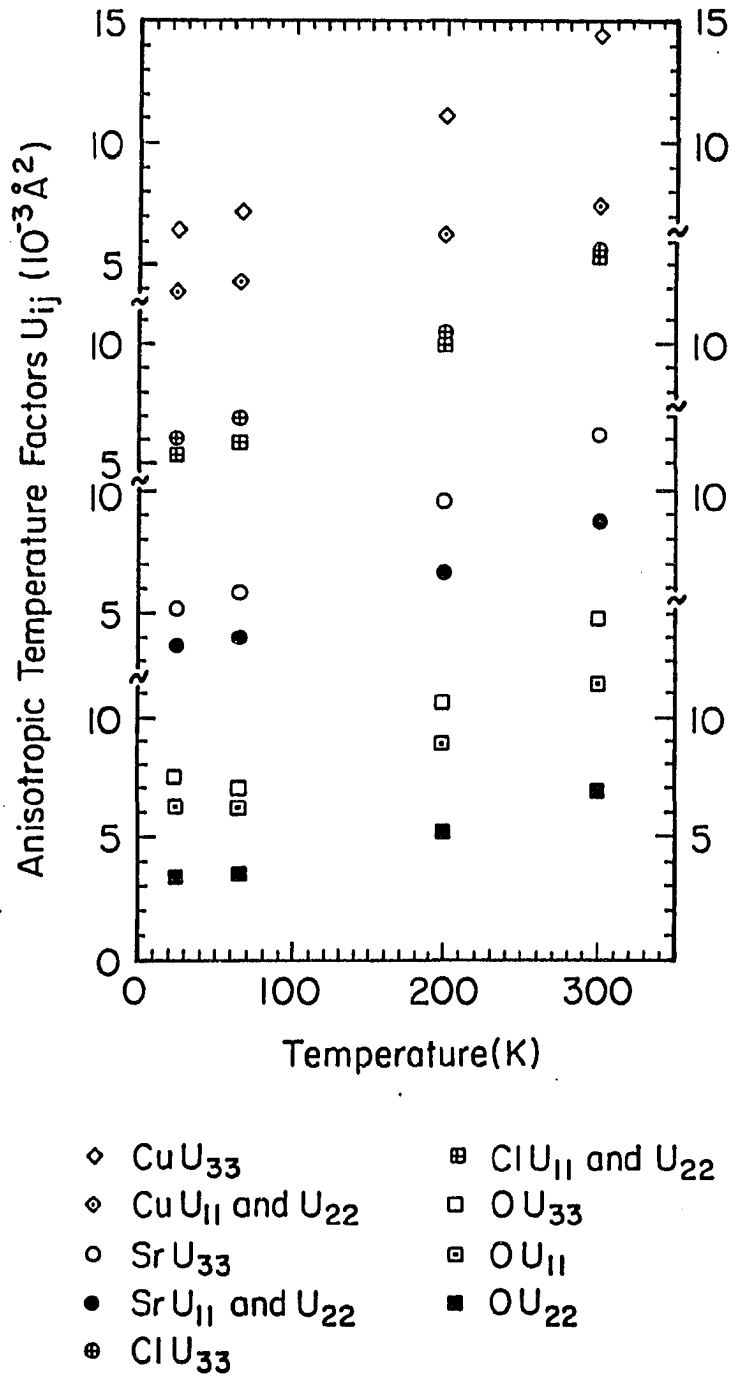


Figure 4.5 Temperature dependence of thermal factors $U_{ij}$ of $Sr_2CuO_2Cl_2$. The sizes of the symbols indicate the precision of the experimental data.

Table III. Selected interatomic distances (Å) at room temperature in $Sr_2CuO_2Cl_2$ and in isotypic (Ref. 59) $La_{1.85}Sr_{0.15}CuO_4$. The calculated average values (given in parentheses) were obtained using the effective ionic radii in Ref. 60.

| $Sr_2CuO_2Cl_2$ | | $La_{1.85}Sr_{0.15}CuO_4$ | |
|---|---|---|---|
| Cu-O (4x) | 1.986 | Cu-O2 (4x) | 1.896 |
| Cu-Cl (2x) | 2.859 | Cu-O1 (2x) | 2.406 |
| Average | 2.277 (2.27) | Average | 2.067 (2.13) |
| | | | |
| Sr-Cl (4x) | 3.047 | (La,Sr)-O1 (4x) | 2.745 |
| Sr-O (4x) | 2.599 | (La,Sr)-O2 (4x) | 2.639 |
| Sr-Cl (1x) | 3.271 | (La,Sr)-O1 (1x) | 2.353 |
| Average | 2.873 (2.94) | Average | 2.645 (2.63) |
| | | | |
| O-Cu (2x) | 1.986 | O2-Cu (2x) | 1.898 |
| O-Sr (4x) | 2.599 | O2-(La,Sr) (4x) | 2.639 |
| Average | 2.395 (2.44) | Average | 2.392 (2.46) |
| | | | |
| Cl-Sr (4x) | 3.047 | O1-(La,Sr) (4x) | 2.745 |
| Cl-Sr (1x) | 3.271 | O1-(La,Sr) (1x) | 2.353 |
| Cl-Cu (1x) | 2.859 | O1-Cu (1x) | 2.406 |
| Average | 3.053 (3.02) | Average | 2.632 (2.54) |

The average interatomic distances within the coordination polyhedra in $Sr_2CuO_2Cl_2$ are within ≈ 2% of those calculated using the effective ionic radii of Shannon [60], as shown in Table III. With the exception of the Sr *z* value, the fractional coordinates of the atoms within the unit cell are essentially the same as in $La_{1.85}Sr_{0.15}CuO_4$. The larger radius of $Cl^-$ relative to $O^{-2}$ causes the Sr atoms to move towards the $CuO_2$ plane and away from the Cl plane, so that the SrCl "rocksalt layer" is much more puckered than the (La,Sr)O layer in $La_{1.85}Sr_{0.15}CuO_4$. The Sr ions are closer to the Cl ions in their own SrCl layer than to Cl ions in the adjacent SrCl layer, whereas in $La_{1.85}Sr_{0.15}CuO_4$, the rare-earth is closer to the O in its own layer, Further, the Cl atoms reside inside a much more spherical cation environment, which may account for the isotropic thermal parameters of this atom, in contrast to the anisotropic parameters of the out-of-plane O1 ions in $La_{1.85}Sr_{0.15}CuO_4$. In both compounds, the a-axis parameters is smaller than expected (4.16 Å) for sixfold-coordinated Cu and O, indicating that the strong Cu-O bonding within the $CuO_2$ plane primarily determines a. In contrast, c-axis values of 14.67 and 12.61 were calculated for $Sr_2CuO_2Cl_2$ and $La_{1.85}Sr_{0.15}CuO_4$, respectively, using the ionic radii for CuVI, OVI, ClVI, LaXI, and SrIX, where the coordination numbers are given by roman numerals; these c values are both smaller than the observed values of 15.61 and 13.19 Å, respectively.

## B. Magnetic Form Factor

The measurements of the antiferromagnetic form factor were performed on a single-crystal sample of $Sr_2CuO_2Cl_2$ using the SCD at IPNS. The single crystal (of dimensions 5.0×5.7×0.3 $mm^3$) used in the present experiment was grown [61] by melting in air prereacted $Sr_2CuO_2Cl_2$ in an alumina boat at 1135°C and cooling to room

temperature at a rate of 3°C/hr. The crystal was mounted to the cold block of a closed-cycle He refrigerator installed on the sample table of the diffractometer.

Detailed neutron diffraction patterns were obtained at 300 and 15 K. The diffraction patterns and the lattice constants obtained at both temperatures are consistent with the crystal structure determined by both x-ray [35] and neutron powder diffraction measurements (see Section A). At 15 K, the neutron diffraction pattern revealed a set of peaks not present in the room temperature pattern. These peaks were identified as $(\frac{1}{2}+h\ \frac{1}{2}+k\ l)$ magnetic reflections. Their intensities were found to be consistent with the low temperature magnetic structure proposed by Vaknin et al. [61]. Figure 4.6 shows the neutron intensities of the (1/2 1/2 0) reflection at two temperatures.

The antiferromagnetic form factor was obtained, at 15 K, by measuring the integrated intensities of the (1/2 1/2 0), (1/2 1/2 2), (1/2 1/2 3), (3/2 3/2 0), (3/2 3/2 6), (3/2 5/2 1), (3/2 3/2 8), and (5/2 5/2 0) magnetic reflections. The integrated intensities were computed from the diffraction data profile using the PEAKINT program in the SCD data analysis package. The measured integrated intensities were corrected for background, detector efficiencies and dead time, sample absorption, and incident neutron spectrum. Assuming the magnetic structure determined by Vaknin et al. [61], the measured magnetic integrated intensities can be used to obtain quantities proportional to $\mu f(\mathbf{Q})$, where $\mu$ is the ordered moment and $f(\mathbf{Q})$ the normalized magnetic form factor. The scale factor was obtained by fitting the observed nuclear integrated intensities to those calculated from the known crystal structure. To avoid uncertainties due to extinction effects, only weak nuclear reflections were used in the fitting. The experimentally determined $\mu f(\mathbf{Q})$ values are listed in Table IV.

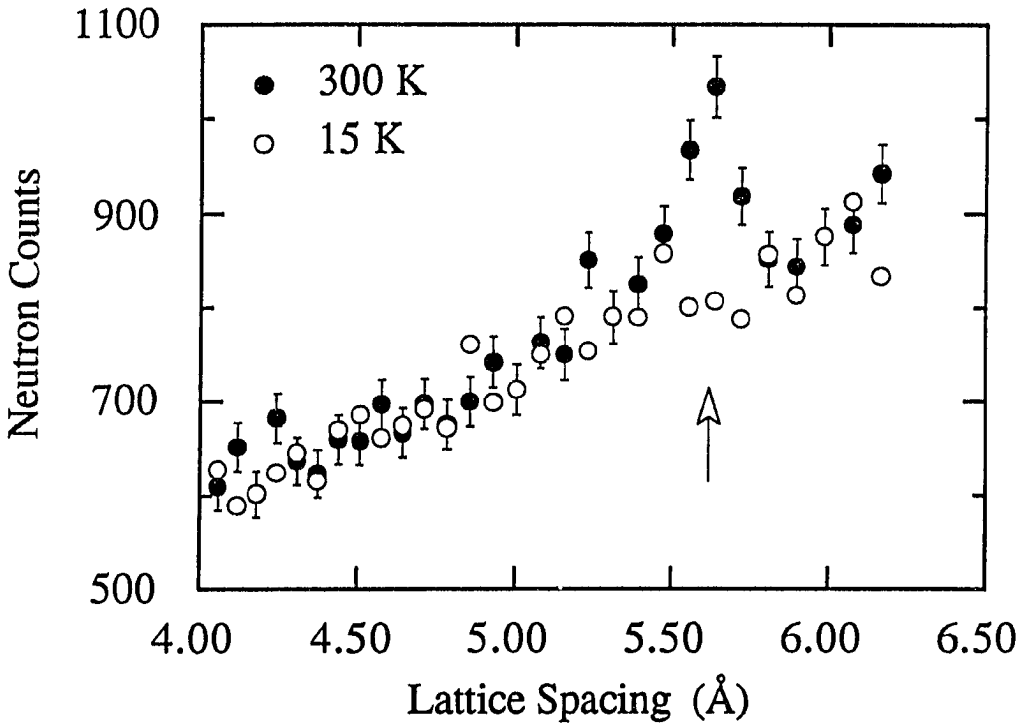


Figure 4.6 The intensity of the (1/2 1/2 0) reflection of $Sr_2CuO_2Cl_2$ as a function of lattice spacing at 15 and 300 K. The intensity is the total counts within a 5×5 cells (see section C.1, Chapter III). The background intensity was due to delayed neutrons (see section A of Chapter III).

The data are compared with the results of Freltoft et al. [28] on $La_2CuO_4$ in Figure 4.7. It is seen (Figure 4.7) that the magnetic form factor of $Sr_2CuO_2Cl_2$ is quite similar to that of $La_2CuO_4$. This seems to suggest that the antiferromagnetic form factor of these Cu compounds is rather determined by the properties of the Cu-O plane and it is unlikely that any significant moments exist on the out-of-plane oxygen (or Cl) ions, as suggested by band theory.

Table IV. Measured $\mu f(\mathbf{Q})$ values for $Sr_2CuO_2Cl_2$. The $\mu f(\mathbf{Q})$ values are expressed in Bohr magneton. Also listed are the calculated amplitudes $\mu f_{Cu}$, $\mu f_b$, and $\mu f_m$ obtained by fitting the data to the spherical $Cu^{2+}$ form factor, band theoretical calculations (Ref. 27), and a model assuming a dipolar spin polarization on the in-plane oxygen atoms (see text).

| (h k *l*) | Q (Å$^{-1}$) | sinθ/λ (Å$^{-1}$) | $\mu f(\mathbf{Q})$ | $\mu f_{Cu}(\mathbf{Q})$ | $\mu f_b(\mathbf{Q})$ | $\mu f_m(\mathbf{Q})$ |
|---|---|---|---|---|---|---|
| (1/2 1/2 0) | 1.121 | 0.0892 | 0.26(2)[a] | 0.2841 | 0.2020. | 0.2587 |
| (1/2 1/2 2) | 1.383 | 0.1100 | 0.26(1) | 0.2751 | 0.2834 | 0.2639 |
| (1/2 1/2 3) | 1.652 | 0.1315 | 0.28(2) | 0.2644 | 0.2933 | 0.2685 |
| (3/2 3/2 0) | 3.364 | 0.2677 | 0.23(2)[a] | 0.1818 | 0.1741 | 0.2377 |
| (3/2 3/2 6) | 4.148 | 0.3301 | 0.20(3) | 0.1453 | 0.1552 | 0.2093 |
| (3/2 5/2 1) | 4.641 | 0.3693 | 0.16(3)[b] | 0.1246 | 0.1388 | 0.1376 |
| (3/2 3/2 8) | 4.668 | 0.3715 | 0.22(3) | 0.1235 | 0.1452 | 0.1948 |
| (5/2 5/2 0) | 5.606 | 0.4461 | 0.00(14) | 0.0901 | 0.0908 | 0.0762 |
| reduced $\chi^2$ | ... | ... | ... | 3.7 | 4.5 | 0.4 |
| $\mu$ ($\mu_B$) | ... | ... | ... | 0.30 | 0.41 | 0.47 |

[a] This value is the average of two equivalent reflections.

[b] This value is the average of three equivalent reflections.

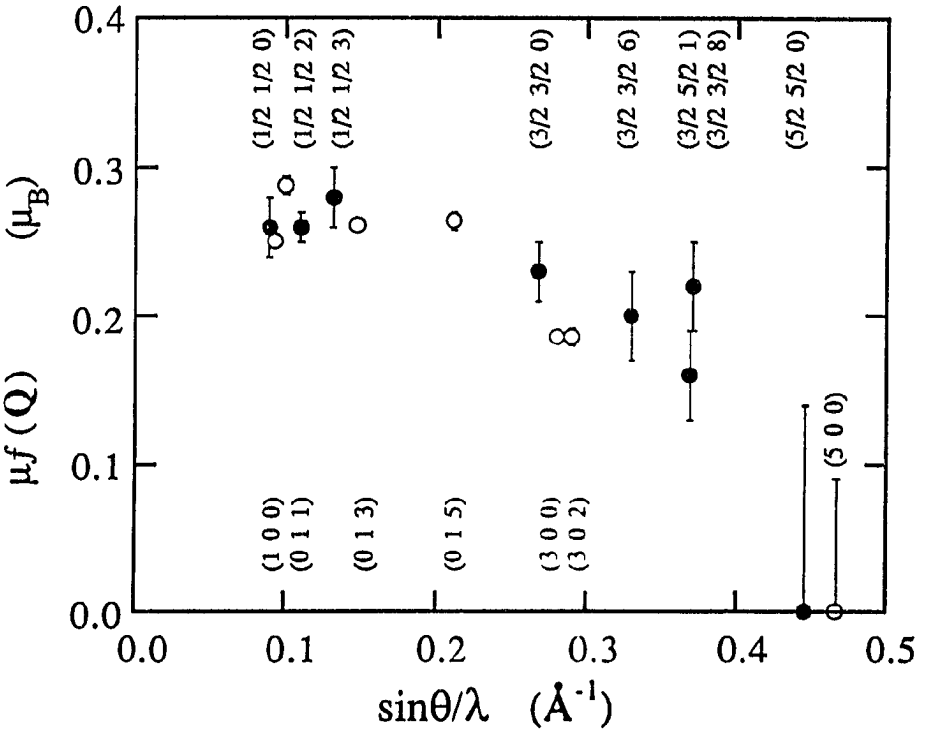


Figure 4.7 Comparison of the experimentally determined $\mu f(Q)$ values of $Sr_2CuO_2Cl_2$ with those of $La_2CuO_4$. Solid circles: $Sr_2CuO_2Cl_2$. Open circles: $La_2CuO_4$. Note that the $La_2CuO_4$ reflections (bottom row) are indexed by reference to the orthorhombic cell.

The experimental data were fitted (Figure 4.8) to the spherical form factor of $Cu^{2+}$ and to the results of spin-polarized band calculations for $Sc_2CuO_4$ [27]. As in the case of $La_2CuO_4$, the fits of the experimental data to both of these theoretical form factors are not very good. As we mentioned above, there is no evidence that any significant moments exist on the (out-of-plane) Cl ions, or for that matter on the in-plane oxygen atoms. Another possibility is that a dipolar spin polarization develops on the in-plane oxygen

ions [62]. In fact, by assuming a model with the in-plane oxygen 2p spin-up orbital forming an antibonding molecular orbital with the nearest neighbor spin-up Cu $3d_{x^2-y^2}$ orbital on one side and similarly for the spin-down orbitals on the other side, a much improved fit to the experimental data is obtained (Figure 4.9). As shall be seen in Chapter VI, this is essentially a special case of the well known covalency model, where the mixing parameter was fixed at 1 (one). To assess whether such a model is valid, more precise and extensive measurements of the magnetic form factors of $La_2CuO_4$, $Sr_2CuO_2Cl_2$, and related compounds are needed.

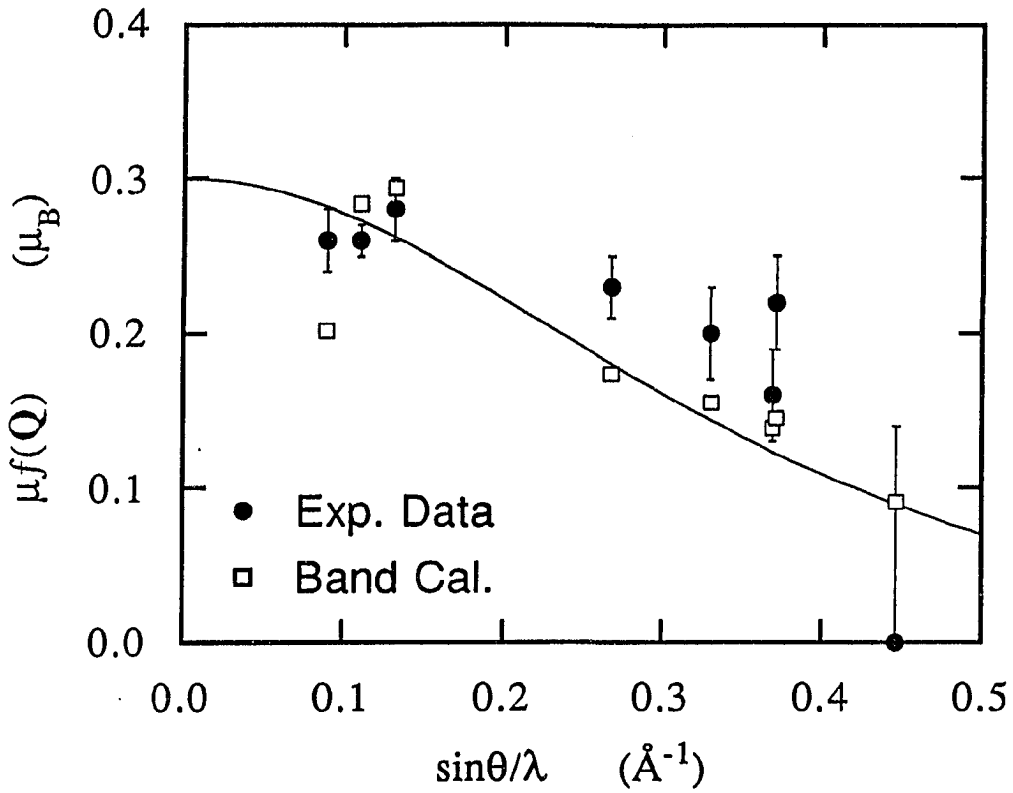


Figure 4.8 Fits of the $Sr_2CuO_2Cl_2$ experimental data to the spherical $Cu^{2+}$ form factor and the results of band theoretical calculations. Solid circles: experimental values of $\mu f(\mathbf{Q})$. Squares: band calculations. Solid curve: the spherical $Cu^{2+}$ form factor.

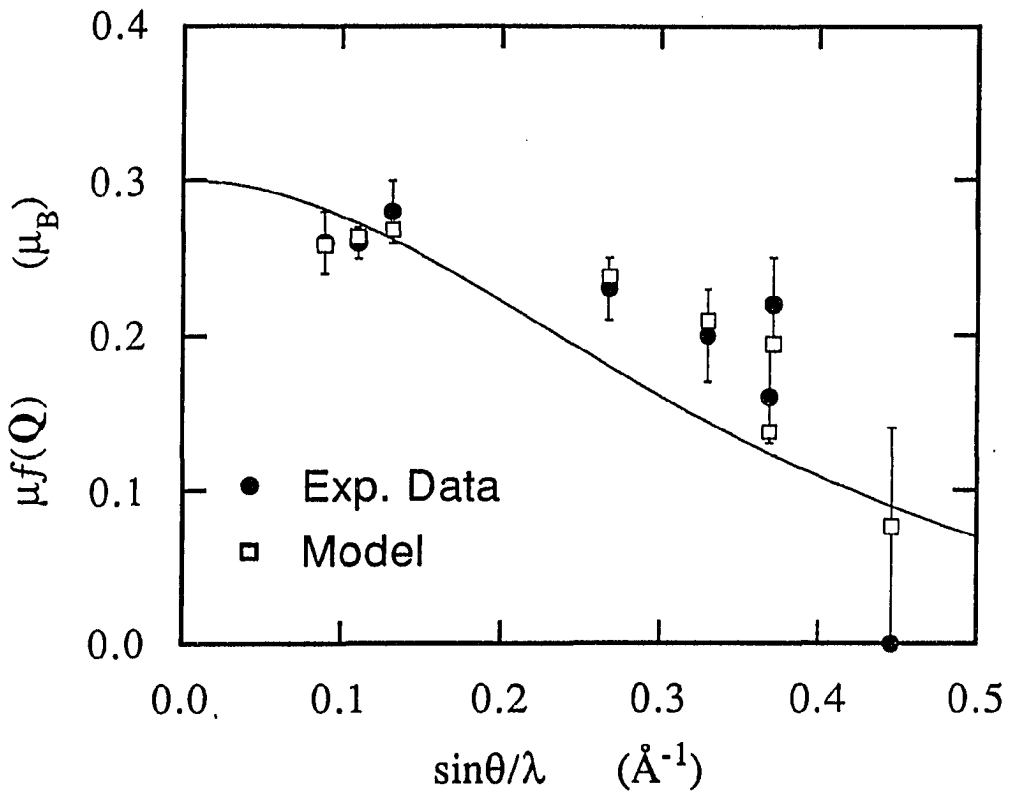


Figure 4.9 Fit of the $Sr_2CuO_2Cl_2$ experimental data to the dipolar spin polarization model (see text). Solid circles: experimental values of $\mu f(\mathbf{Q})$. Solid curve: the spherical $Cu^{2+}$ form factor. Squares: model calculations.

# V. NEUTRON DIFFRACTION STUDY OF $La_2NiO_4$

In a continuing endeavor to characterize the antiferromagnetic form factor of the high-$T_c$ parent compounds, we performed neutron diffraction measurements of $La_2NiO_4$ on a single-crystal sample using the SCD at IPNS. The crystal used in the present experiment was the same one used by Lander et al. [9] in their studies on the crystal structure and field-induced magnetization density of the compound. The sample is stoichiometric as determined from chemical analysis and later confirmed by structure refinement. The crystal [8-9] and magnetic [63-64] structure of the stoichiometric $La_2NiO_4$ have been well established (see below). However, it is also well known that the stoichiometric $La_2NiO_4$ is very sensitive to oxygen and can easily become over-oxidized [8], and the magnetic properties of $La_2NiO_{4+\delta}$ vary widely with the oxygen content [63-64]. We therefore decided to carry out some preliminary measurements to verify and further characterize the crystal and magnetic structure of the sample before detailed measurements of the antiferromagnetic form factor were performed.

## A. Crystal and Magnetic Structure

The crystal used in the preliminary experiment was of volume ~ 60 $mm^3$. It was encapsulated in an aluminum can, as was received, and mounted to the cold block of a closed-cycle He refrigerator installed on the sample table.

$La_2NiO_4$ is isostructural to $La_2CuO_4$. The HTT-LTO transition takes place at ~ 700 K [65], so at room temperature, the stoichiometric $La_2NiO_4$ is already in the LTO phase, with space group Bmab. At ~ 70 K, below the transition temperature, the crystal structure further transforms to the LTT phase, with space group $P4_2/ncm$. Accompanying the transition, there is a sudden change of the rotation axis of the $NiO_6$ octahedra, from

the LTO [1 0 0] direction to the LTO <1 1 0> direction. The transition has two observable consequences. First, as the structure transforms from the LTO to the LTT phase, the (h 0 0) and (0 h 0) reflections, which were separated in the reciprocal space due to the orthorhombic twins, now emerge to a single peak. Second, below the transition temperature, a new set of reflections appears because the crystal symmetry is lower. All these results were confirmed in our experiments.

In Figure 5.1(a)-(b), we show the measured lattice parameters obtained from the least-squares fit of more than 40 reflections at three temperatures, 15, 150, and 300 K. At 15 K, there is no discernable difference between a and b to within the experimental precision. For comparison, we also plotted the lattice parameters reported by Lander et al. [9] for the same sample. As can be seen, the agreement is fair, considering that the instrument resolution is only of ~ 1%. Figure 5.1(c) shows the unit-cell volume as a function of temperature.

In the LTO phase, $La_2NiO_4$ has twined structure and the common axis for the twining is in the <1 1 0 > direction [9]. As schematically shown in Figure 5.2, all reflections except (h h 0) split into two peaks, one from each of the twined domains. Below 70 K, the twins collapse as the crystal structure reverts to tetragonal. The splitting was not evident in our measurements due to the relatively poor resolution of the instrument. Therefore, the integrated intensity and the peak width discussed hereafter should be regarded as the quantities associated with the A(h k *l*) and B(k h *l*) twins, but not individual reflections. In general, the domain population $\alpha_A$ and $\alpha_B$ need not be equal. Nevertheless, for the present crystal, the least-squares refinement shows that, to within statistics, $\alpha_A = \alpha_B$, i.e., the twined domains are indeed equally populated.

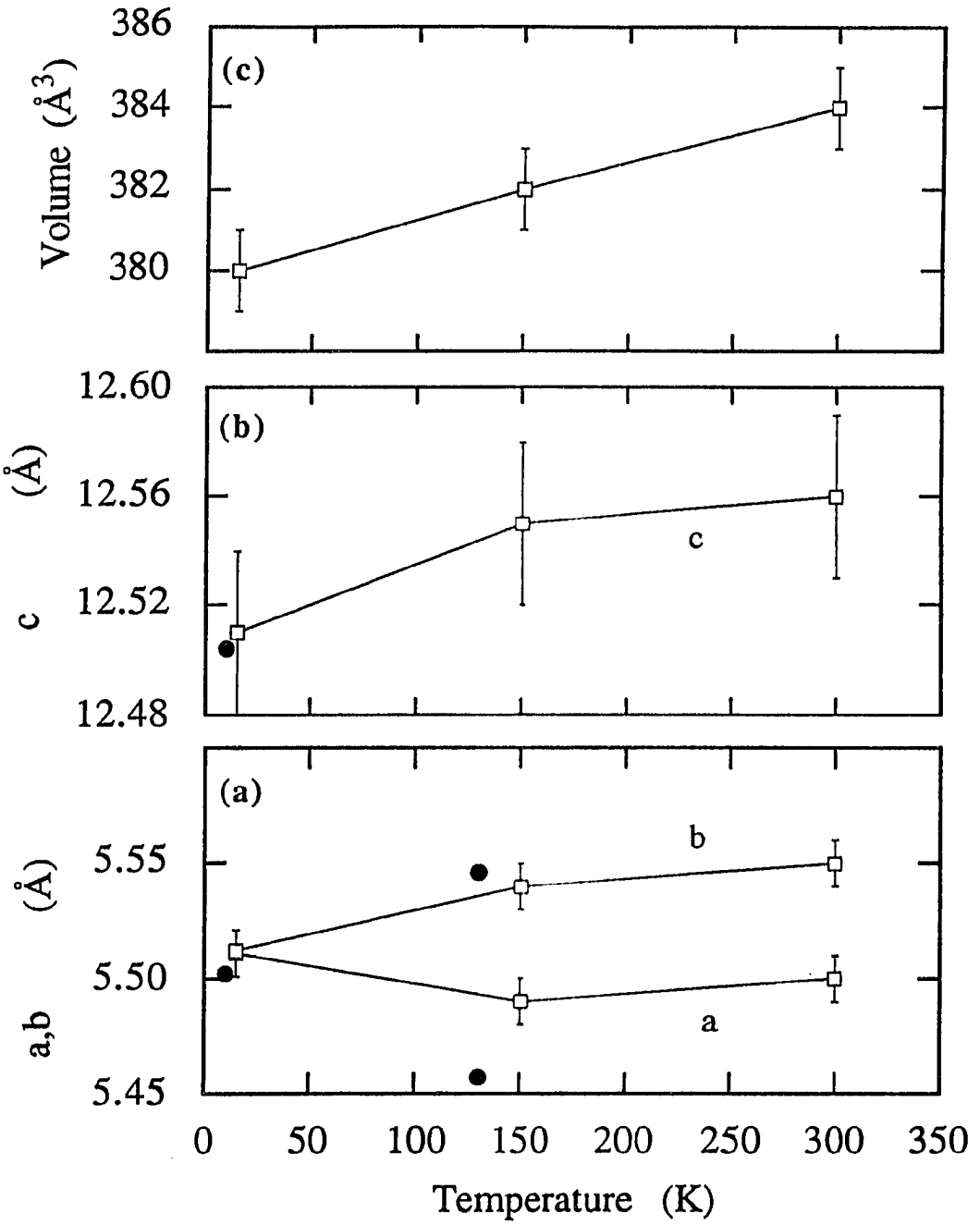


Figure 5.1 The lattice parameters and unit-cell volume of $La_2NiO_4$ as a function of temperature. The open squares were obtained in the present experiment; the solid symbols are the values reported in Ref. 9 for the same sample.

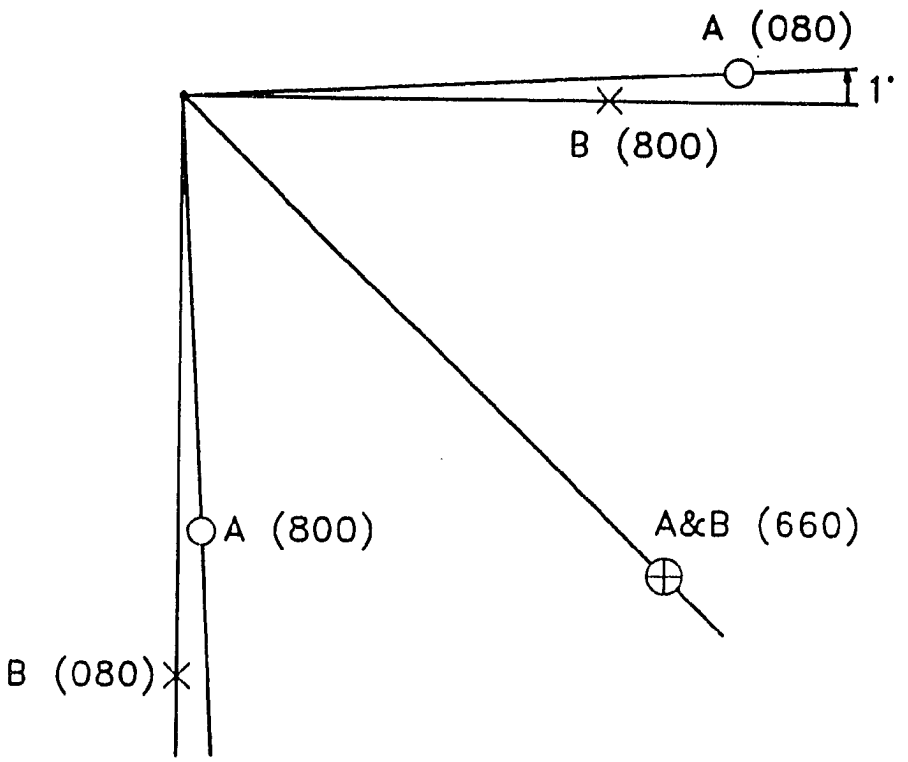


Figure 5.2 Schematic of the reciprocal space of $La_2NiO_4$ in the LTO phase. A and B refer to the domains in the orthorhombic phase. (After Ref. 9)

The diffraction profile measured by SCD is 3-dimensional (x, y, and t). There has not been a unique definition of the peak width. In one way, one may use a fractional intensity, i.e., the ratio of the total intensity over a small integration volume, say 3×3×3, versus the integrated intensity as a measure of the peak width. If the peaks are sharp, this can be rather easily obtained by using the computer program PEAKINT (see Chapter III), because in this case, the total intensity over the large integration volume, 5×5×5, gives a good account of the integrated intensity. The peaks measured in the present experiment

are, however, broad due to the twined domains. To obtain reliable integrated intensities, we used the program INTSCD that performs the contour integration (see Chapter III). In Figure 5.3(a) we show the fractional intensity, defined as the ratio of the intensity over the 3x3x3 integration volume obtained using PEAKINT versus the integrated intensity obtained using INTSCD, of the (0 2 2) reflection as a function of temperature. Between 80 and 300 K, the orthorhombic strain develops as the temperature decreases. As a result, the peak broadens. Below 70 K, the peak sharpens abruptly as the crystal structure reverts to tetragonal and the orthorhombic twins collapse.

Below 70 K, a new set of Bragg reflections, which are forbidden by the LTO structure, appears due to the sudden change of the rotation axis of the $NiO_6$ octahedra. A subset of these new reflections is the (h h *l*) type of reflections, with h + *l* = odd. In the present experiment, we observed intensities at the (3 3 4), (3 3 6), (2 2 3) and (1 1 2) positions. Figure 5.3(b) shows the temperature dependence of the integrated intensity (obtained using INTSCD) of the (2 2 3) reflection. In addition, at the transition temperature, we also observed a discontinuity in the integrated intensities of those nuclear reflections with h + k = odd and k + *l* = even. An example is shown in Figure 5.3(b) for the (4 1 7) reflection. These observations confirmed that the rotation axis of the $NiO_6$ octahedra indeed changed at the LTO-LTT transition, because the appearance of these reflections in the LTO phase was associated with the rotation of the $NiO_6$ octahedra. Notice that the intensity of (4 17) reflection has a magnetic component (from the (1 4 7) reflection of the other domain), but the magnetic intensity is estimated to be no more than 5% of the total intensity. For comparison, the intensity of the (0 2 2) reflection is also plotted.

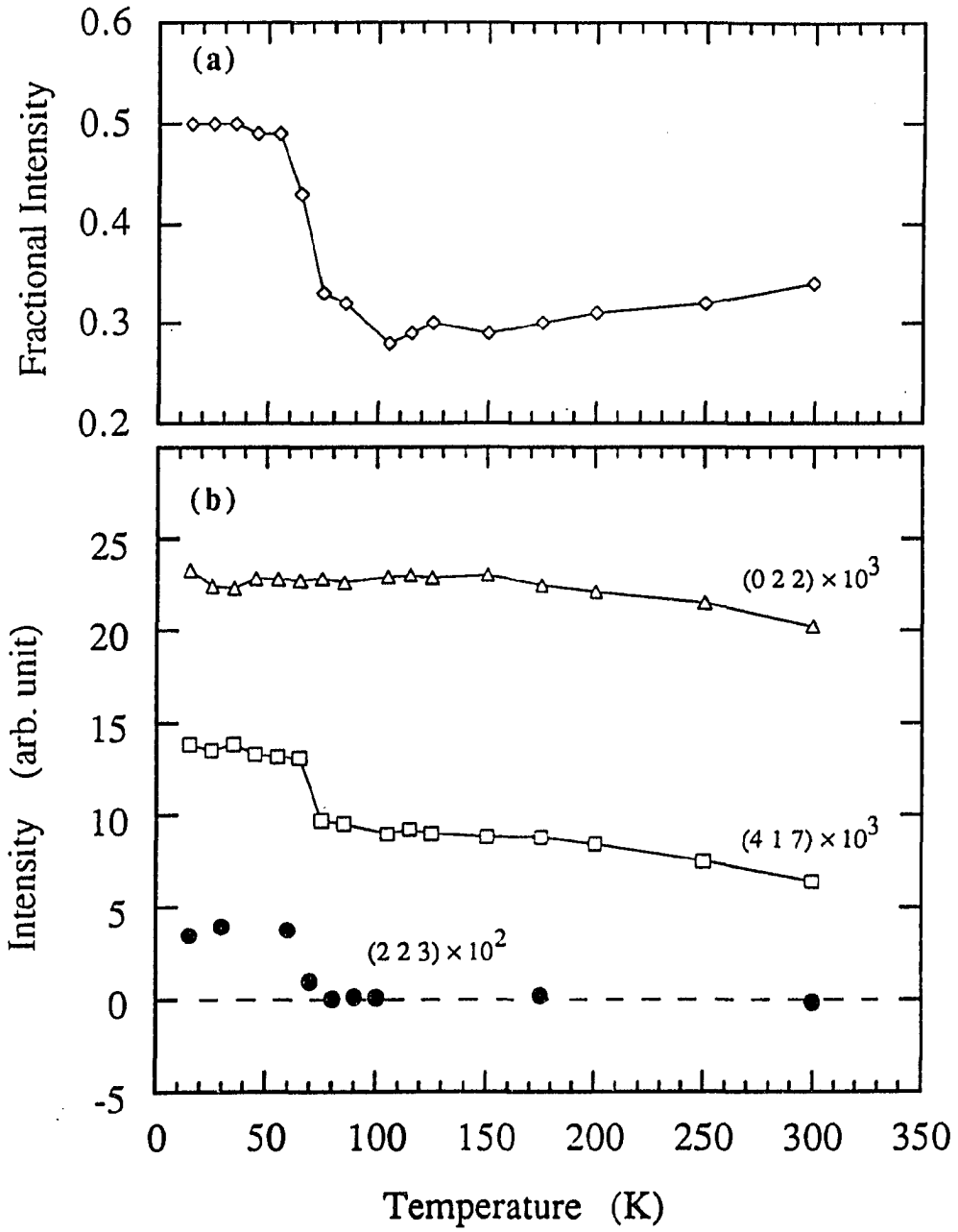


Figure 5.3 **The LTO-LTT phase transition in $La_2NiO_4$. (a) The fractional intensity (see text) of the (0 2 2) reflection. (b) The integrated intensity of the (0 2 2), (2 2 3), and (4 1 7) reflections.**

The crystal structure parameters at 10 K have been refined and given in Ref. 9. For convenience, we list them again in Table V. In Appendix II, we list the structure factors calculated using these parameters.

Stoichiometric $La_2NiO_4$ orders antiferromagnetically with $T_N \sim 650$ K [66]. The magnetic structure in the LTO phase has been well established [63-64] by both unpolarized and polarized neutron experiments: The spins and the magnetic propagation wave vector are parallel to the [1 0 0] direction. Just like the crystal structure, the magnetic structure in the LTO phase is also twined. Since our instrument did not have sufficient resolution to separate the twined reflections, the observed intensity at each (h k *l*) position was actually the sum of the A(h k *l*) and B(k h *l*) twins.

Table V. Structural parameters obtained for single-crystal $La_2NiO_4$ at T = 10 K (Ref. 9). The lattice parameters are a = 5.502(3) Å and c = 12.504(11) Å, $V^{cell} = 378.5$ Å$^3$, space group $P4_2/ncm$. $B_{iso}$ is the isotropic thermal factor [42]. R factor: 6.4%.

| Atom | | *x* | *y* | *z* | $B_{iso}$ (Å$^{-2}$) |
|---|---|---|---|---|---|
| La | (8*m*) | -0.0076(2) | -0.0076(2) | 0.3641(1) | 0.21(3) |
| Ni | (4*d*) | 0 | 0 | 0 | 0.23(3) |
| O(1) | (4*e*) | 1/4 | 1/4 | -0.0142(2) | 0.30(3) |
| O(1') | (4*a*) | 3/4 | 1/4 | 0 | 0.32(3) |
| O(2) | (8*m*) | 0.0296(3) | 0.0296(3) | 0.1769(1) | 0.47(3) |

Our form factor measurements (see below) were conducted at 15 K, i.e., with the compound in the LTT phase. Based on the previously reported observations that there is no change in the intensity of the (0 1 1) magnetic reflection through the transition temperature (~ 70 K), it was argued [8-9] that the magnetic structure remained unchanged at the LTO-LTT transition. To verify this, we measured the temperature dependence of the (0 1 1) and (0 3 3) magnetic reflections (Figure 5.4). To within experimental precision, we found no evidence of any intensity change around 70 K. It should be pointed out, however, that these results do not rule out [8-9,11] the possibility of a more complicated 2**k** magnetic structure. However, our analysis of the magnetization density does not depend on whether we have a single or multiple **k** structure. In the former case, we measure the total magnetization density; in the latter we measure a particular component only. Assuming a single **k** magnetic structure, there will be two equally populated magnetic domains with spins parallel to [1 0 0] and [0 1 0], respectively, because of the tetragonal symmetry in the LTT phase. Under the same assumption, it is easy to show that only magnetic reflections (h k *l*) with h + k = odd are allowed. Reliable measurements of the magnetic intensities can be obtained for the (0, odd, odd) and (odd, even, 0) type of reflections, since the nuclear structure factors of these reflections are zero in the LTT crystal structure.

## B. Magnetic Form Factor

Detailed measurements of the antiferromagnetic intensities were performed on a small crystal of approximate dimensions 1.5×1.5×4.0 $mm^3$ extracted from the sample used in the previous experiment. The crystal was kept at 15 K using a closed-cycle He refrigerator throughout the measurements.

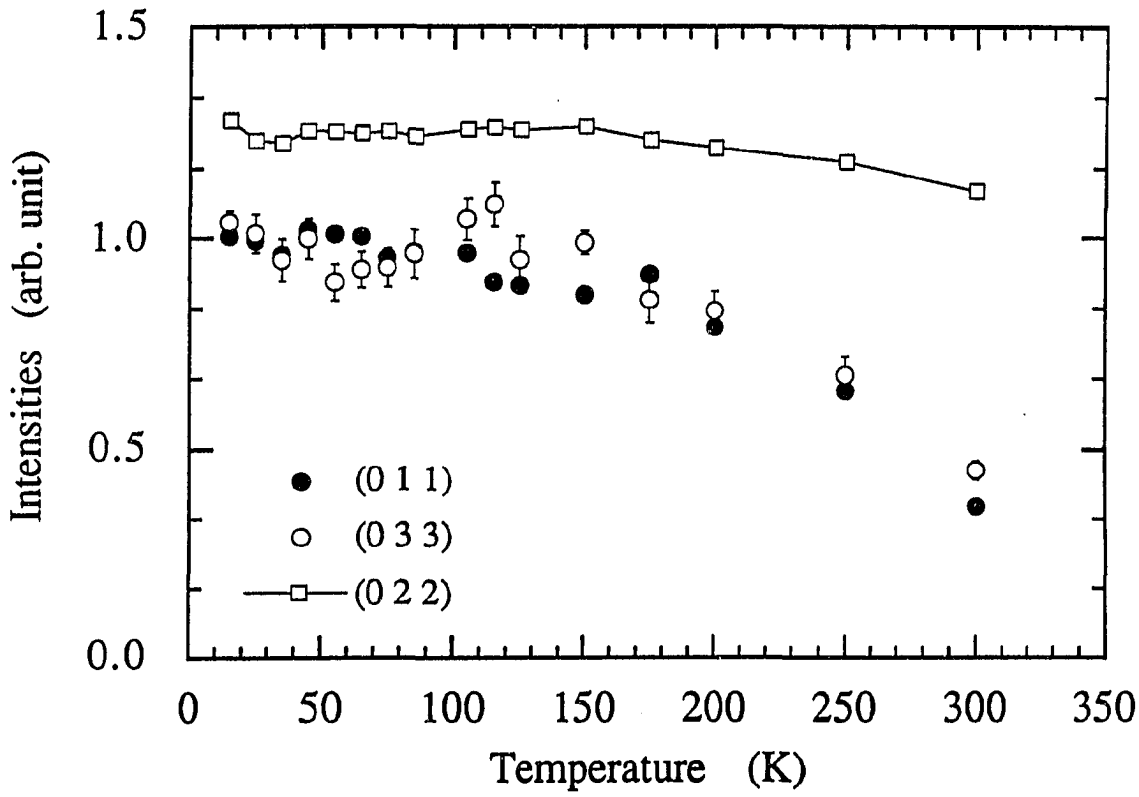


Figure 5.4 Temperature dependence of the integrated intensity of the (0 1 1) and (0 3 3) magnetic reflection of $La_2NiO_4$. Compared to the (0 2 2) reflection, the intensities of (0 1 1) and (0 3 3) drop faster with the increase of temperature, confirming that these two reflections are of magnetic origin.

A typical 2-dimensional diffraction pattern is shown in Figure 5.5 for the (0 k *l*) reflections measured in one crystal setting. This figure also demonstrates that, with this diffractometer, a large volume of reciprocal space can be sampled simultaneously. This is precisely one of the unique advantages of a time-of-flight diffractometer, as discussed in Chapter III.

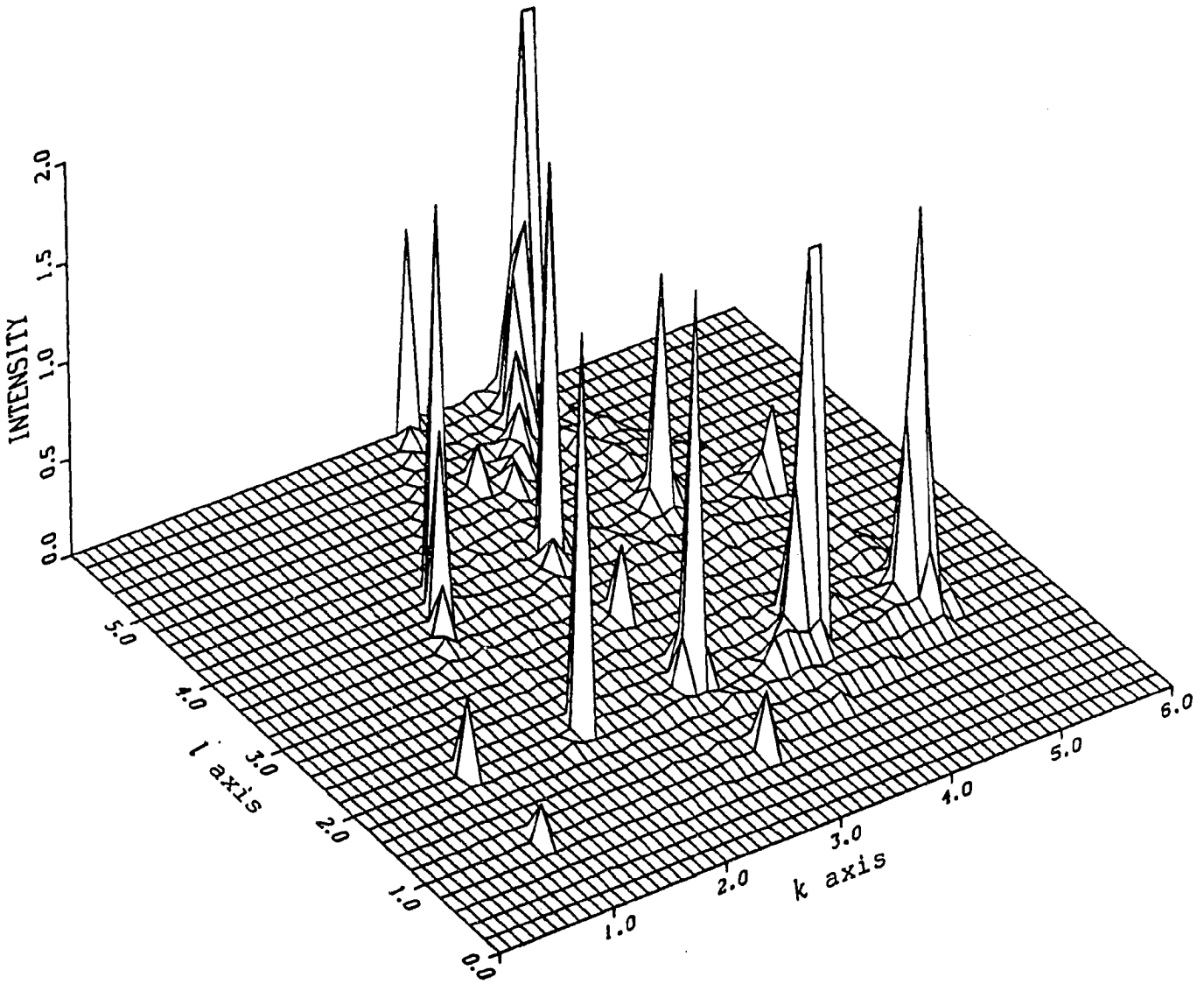


Figure 5.5 The diffraction pattern of the (0 k *l*) reflections of $La_2NiO_4$ measured by SCD. Notice that (0 1 1), (0 1 3), (0 3 3), and (0 3 5) are pure magnetic reflections. The intensity is in an arbitrary unit. The strong nuclear reflections have been truncated to promote the visibility of the weak magnetic reflections.

1. Intensity normalization

To obtain the antiferromagnetic form factor, we measured the integrated intensity of several magnetic Bragg reflections. The integrated intensities were computed from the diffraction data profile using the program INTSCD because the reflections are broad.

The measured integrated intensities corrected for sample absorption, the detector efficiency, dead-time loss, and the incident neutron spectrum, are proportional to $<q^2>|F_m|^2$. To determine the scale factor, we fitted the corrected integrated intensities of a selected number of nuclear reflections to the structure factors evaluated using the structure parameters in Table V (Ref. 9). In Figure 5.6 and Table VI, we compare the normalized integrated intensities of these reflections with the calculated structure factors.

2. Extinction effects

In principle, in the above fitting procedure, we should have included all measured nuclear reflections. That only selected reflections were used here was based on extinction considerations. In their structure work using constant wavelength neutrons ($\lambda$=1.18 Å), Lander et al. [9] found that the extinction corrections to most reflections were small, with a maximum of 23% for the strong (4 0 0) reflection. In the present experiment, however, reflections were measured using neutrons over a broad range of wavelengths, from 1.0 to 9.0 Å. Since the experiment was designed to measure the relatively weak magnetic reflections, most of the nuclear reflections accessible with the instrument were the low index (usually strong) reflections measured at long wavelengths and, therefore, subject to large extinction corrections. In fact, we found that the intensities of some strong reflections reduced as much as 50%. This makes it difficult to correct for these intensities, since any extinction corrections more than 30% are usually unreliable.

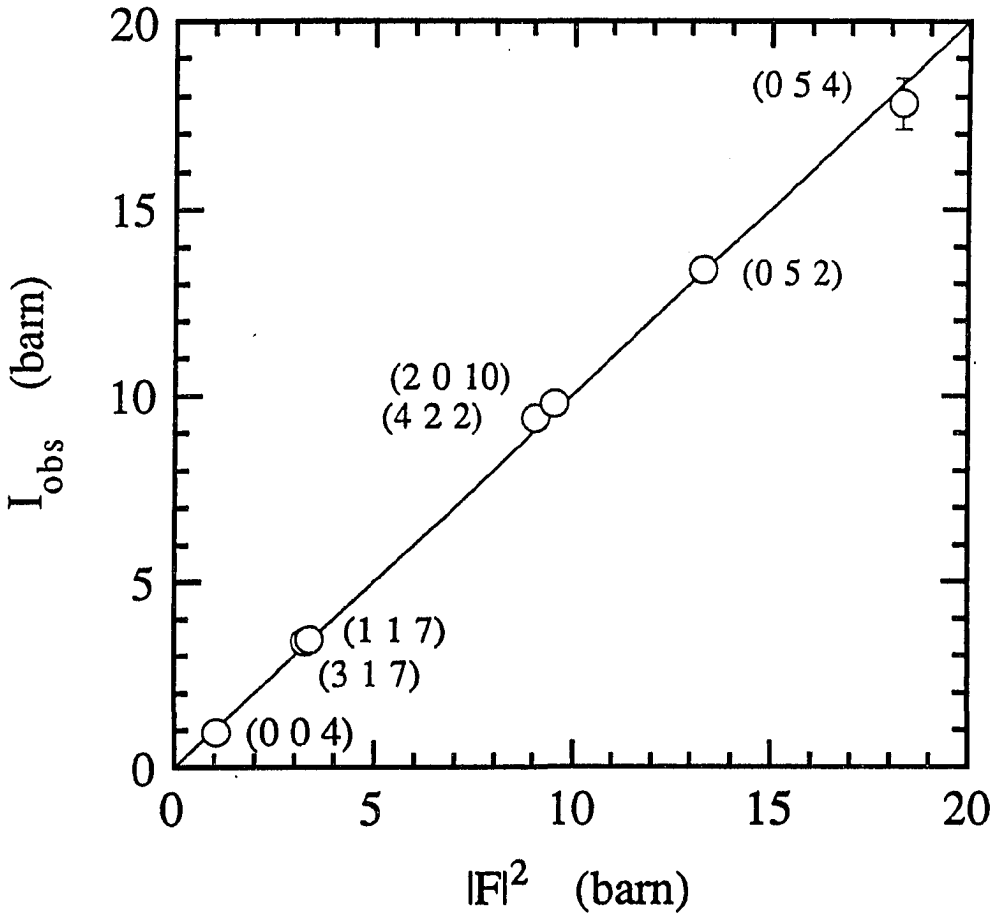


Figure 5.6 Comparison of the measured integrated intensity of $La_2NiO_4$ with the calculated structure factor for the nuclear Bragg reflections used in the normalization procedure. $I_{obs}$: measured. $|F|^2$: calculated. Notice that $I_{obs}$ has been normalized by the scale factor (see text).

Table VI. Comparison of the measured integrated intensity of $La_2NiO_4$ with the calculated structure factor for the nuclear Bragg reflections used in the normalization procedure. $I_{obs}$: measured. $|F|^2$: calculated. Notice that $I_{obs}$ has been normalized by the scale factor (see text).

| (h k *l*) | Number of Measurements | Neutron Wavelength λ (Å) | $I_{obs}$ (barn) | $\|F\|^2$ (barn) |
|---|---|---|---|---|
| (0 0 4) | 4 | 3.95—4.61 | 0.95±0.03 | 1.04 |
| (3 1 7) | 3 | 1.70—2.02 | 3.39±0.25 | 3.28 |
| (1 1 7) | 4 | 2.00—2.60 | 3.44±0.19 | 3.39 |
| (4 2 2) | 4 | 1.62—1.93 | 9.40±0.24 | 9.07 |
| (2 0 10) | 4 | 1.61—1.79 | 9.79±0.15 | 9.54 |
| (0 5 2)[a] | 5 | 1.27—1.70 | 13.18±0.33 | 13.32 |
| (0 5 4)[a] | 3 | 1.63—1.67 | 17.84±0.68 | 18.32 |

[a] These two reflections are also allowed by the magnetic structure. However, the intensities due to magnetic scattering are estimated to be less than 0.15 barn and, therefore, are insignificant considering the relatively large error bars of the observed intensities.

In order to minimize the uncertainties which may be introduced by extinction corrections, we decided to include only weak nuclear reflections and reflections with moderate nuclear structure factors but measured at relatively short wavelengths.

To estimate the extinction corrections, we used the Becker-Coppens extinction parameter [49] previously determined for this crystal in Ref. 9. The extinction effects

were found to introduce only minor adjustments to the data: a maximum of 10% for the (0 1 1) reflection and much smaller effects for the other reflections. For demonstration purposes, we list in Table VII the extinction and absorption corrections for the (0 1 1) and (1 0 1) reflections measured at a variety of wavelengths.

Table VII. The extinction and absorption corrections for the (0 1 1) and (1 0 1) magnetic reflections of $La_2NiO_4$ measured at a variety of wavelengths. $\overline{T}$ is the neutron penetration distance. $I_{obs}$ is the corrected integrated intensity (before normalized).

| (h k *l*) | λ (Å) | $\overline{T}$ (cm) | A | $Y_{ext}$ | $I_{obs}$ (arb. unit) |
|---|---|---|---|---|---|
| (0 1 1) | 5.8346 | 0.2022 | 0.86 | 0.95 | 235±6 |
| (0 1 1) | 6.5487 | 0.1853 | 0.85 | 0.95 | 202±6 |
| (0 1 1) | 7.1971 | 0.1716 | 0.85 | 0.94 | 196±7 |
| (0 1 1) | 7.7870 | 0.1597 | 0.85 | 0.91 | 226±10 |
| (1 0 1) | 7.3373 | 0.1980 | 0.83 | 0.91 | 225±5 |
| (1 0 1) | 7.8893 | 0.1945 | 0.82 | 0.90 | 249±10 |
| (0 1 1) | 8.1546 | 0.1486 | 0.85 | 0.92 | 205±10 |

3. Multiple Bragg scattering

Special attention was given to possible contamination of the data from multiple Bragg scattering. This is important because the magnetic intensities in $La_2NiO_4$ are weak, and, as a result, can be strongly influenced by the multiple Bragg scattering process

among *nuclear* reflections. The appearance of the additional nuclear reflections in the LTO and the LTT phase greatly increases the possibility for multiple Bragg scattering. This was realized and discussed at length by Freltoft et al. [28] in their studies of $La_2CuO_4$. The multiple Bragg scattering effects were, however, less pronounced in our measurements of $Sr_2CuO_2Cl_2$, for the compound remained in the HTT phase and the possibility for multiple Bragg scattering was much reduced.

Multiple Bragg scattering occurs when more than one reciprocal lattice point lies on the Ewald sphere, and results in an anomalous Bragg reflection intensity for a given neutron wavelength and particular crystal orientation. With a time-of-flight diffractometer, it is possible to measure a specific reflection over a large range of neutron wavelengths, and the measurements that may have been contaminated by multiple Bragg scattering can be identified by examining the wavelength dependence of the reflection. We illustrate the procedure by reference to Figure 5.7. Figure 5.7(a) shows the intensity of the {3 1 1} nuclear reflection as measured at various wavelengths. It can be seen that six of these measurements may have been contaminated by multiple Bragg scattering, while the remaining eight measurements are consistent among themselves and are in agreement with the calculated value which is represented by the dashed line. Figure 5.7 (b) illustrates the application of this procedure to the measurements of the (0 1 9) magnetic reflection; measurements that may be contaminated by multiple Bragg scattering were discarded and the average of the remaining consistent set of data [dashed line in Figure 5.7(b)] was taken as representing the magnetic structure factor for this reflection. This procedure was applied to each of the magnetic reflections as well as the nuclear reflections used in the normalization process.

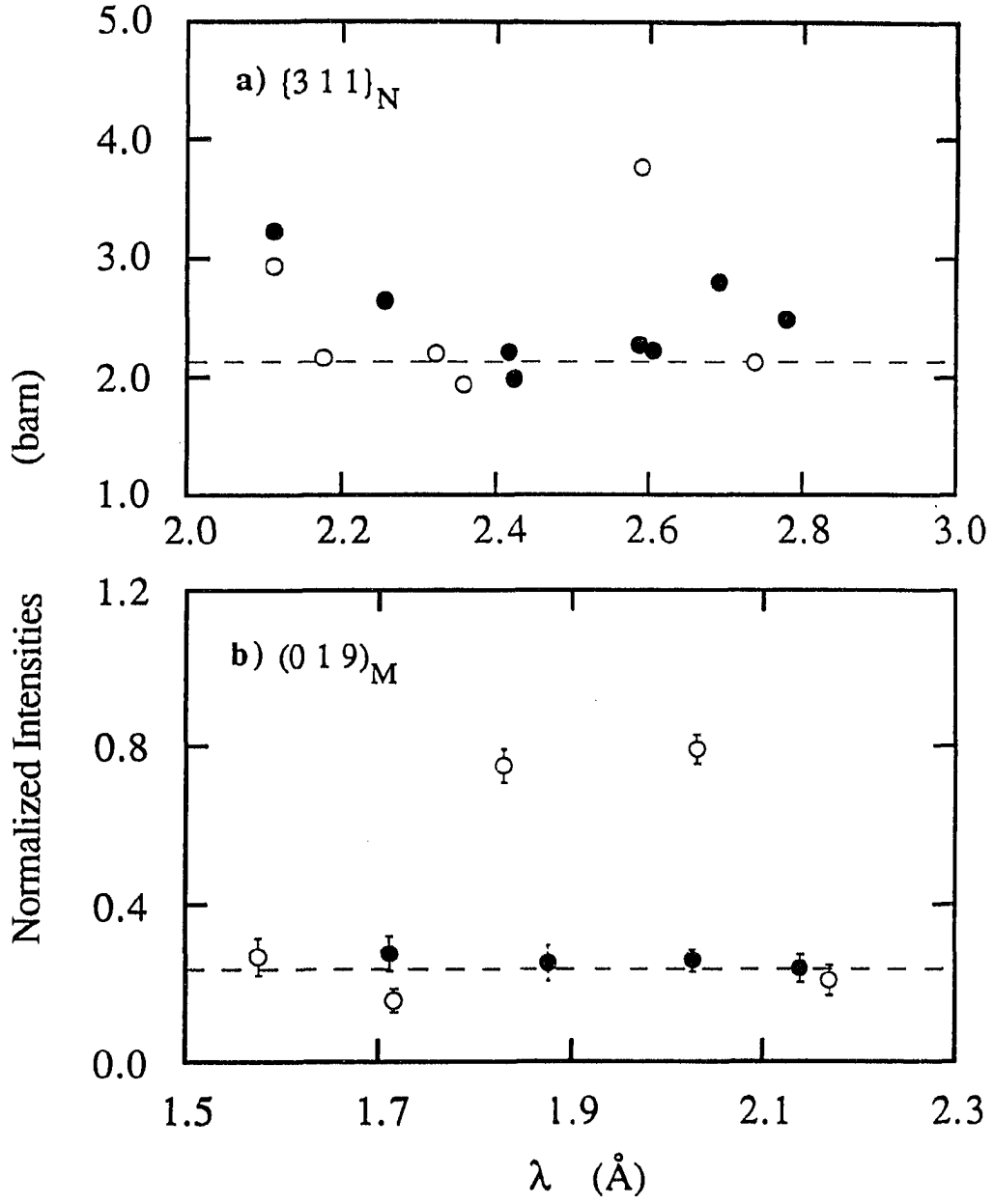


Figure 5.7 **Illustration of multiple Bragg scattering effects in $La_2NiO_4$:** The wavelength dependence of the observed structure factors of the {3 1 1} and (0 1 9) reflections. (a) {3 1 1} nuclear reflections. Open circles: (3 1 -1). Solid circles: (3 1 1). The dashed line is the calculated value. (b) (0 1 9) magnetic reflection. The dashed line is the average of seven self-consistent data points. The open and solid symbols correspond to two different scans.

The magnetic amplitude $\mu f(\mathbf{Q})$, where $\mu$ is the average ordered moment per Ni atom and $f(\mathbf{Q})$ the normalized magnetic form factor, is related to the magnetic structure factor by Equation (2.36). There is no complication of the phase problem because, as shall be discussed in the next section, the magnetization density of this compound is centrosymmetric and the form factor is real. To obtain the magnetic structure factor, we evaluated the $<q^2>$ term using the proposed spin structure (with two equally populated magnetic domains) described earlier in Section A. To estimate the Debye-Waller factor in Equation (2.36), we used the isotropic thermal factor, $B_{iso}$, previously determined for this compound (Table V). In terms of $B_{iso}$, the Debye-Waller factor can be written as [42]

$$e^{-W_d} = e^{-B_{iso}/4d^2} = e^{-B_{iso}(\sin\theta/\lambda)^2} \quad . \tag{5.1}$$

For Ni atoms, $B_{iso} = 0.23$ Å$^2$ [9]. From Equation (5.1), it can be shown that the Debye-Waller factor is not significantly different from unity in the Q range covered in the present experiment. For instance, for the (0 5 3) reflection, $e^{-W_d} = 0.95$. The deduced $\mu f(\mathbf{Q})$ values and the results of these calculations are summarized in Table VIII.

The experimentally determined magnetic amplitudes, $\mu f(\mathbf{Q})$, for $La_2NiO_4$ are compared with those of $La_2CuO_4$ in Figure 5.8. For this comparison, the $La_2CuO_4$ data were multiplied by a factor of four to account for the difference in the ordered moments of these compounds. It can be seen (Figure 5.8) that the magnetic form factors of these compounds are quite similar and are characterized by a plateau at low Q values. In addition, one cannot obtain a satisfactory fit to the data by using a simple ionic form factor. This can be seen by reference to Figure 5.8, where the solid line is a least-squares fit to the $La_2NiO_4$ data using the spherical $Ni^{2+}$ form factor.

Table VIII. Neutron diffraction results of the antiferromagnetic form factor of $La_2NiO_4$ at 15 K for 16 magnetic reflections. N is the number of measurements, $\lambda$ the neutron wavelength, and $I_{obs}$ the normalized intensities of the magnetic reflections.

| (h k *l*) | $\sin\theta/\lambda$ ($Å^{-1}$) | N | $\lambda$ (Å) | $I_{obs}$ (barn) | $<q^2>$ | $\mu f(Q)$ ($\mu_B$) |
|---|---|---|---|---|---|---|
| (0 1 1) | 0.0993 | 7 | 5.83—8.15 | 0.63±0.05 | 0.500 | 1.04±0.05 |
| (0 1 3) | 0.1505 | 5 | 3.81—5.44 | 0.63±0.04 | 0.500 | 1.04±0.04 |
| (0 1 5) | 0.2196 | 10 | 2.64—3.59 | 0.65±0.04 | 0.500 | 1.06±0.04 |
| (0 1 7) | 0.2943 | 11 | 2.03—2.78 | 0.49±0.08 | 0.500 | 0.91±0.08 |
| (0 1 9) | 0.3712 | 7 | 1.58—2.17 | 0.23±0.05 | 0.500 | 0.63±0.07 |
| (0 3 1) | 0.2755 | 7 | 2.11—2.97 | 0.65±0.04 | 0.500 | 1.06±0.04 |
| (0 3 3) | 0.2979 | 7 | 1.94—2.73 | 0.40±0.05 | 0.500 | 0.83±0.06 |
| (0 3 5) | 0.3381 | 6 | 1.69—2.32 | 0.37±0.04 | 0.500 | 0.79±0.05 |
| (0 3 7) | 0.3907 | 3 | 1.70—2.00 | 0.41±0.09 | 0.500 | 0.83±0.10 |
| (1 2 0) | 0.2032 | 8 | 2.95—3.99 | 0.55±0.06 | 0.400 | 1.09±0.06 |
| (3 2 0) | 0.3277 | 3 | 1.97—2.50 | 0.18±0.03 | 0.154 | 0.99±0.08 |
| (1 4 0) | 0.3747 | 10 | 1.55—2.16 | 0.26±0.04 | 0.471 | 0.69±0.06 |
| (0 5 1) | 0.4561 | 7 | 1.29—1.73 | 0.25±0.05 | 0.500 | 0.65±0.08 |
| (0 5 3) | 0.4699 | 3 | 1.63—1.75 | 0.16±0.05 | 0.500 | 0.52±0.09 |
| (1 0 2)[a] | 0.1211 | 4 | 5.01—6.47 | 0.28±0.05 | 0.219 | 1.04±0.09 |
| (1 4 2)[a] | 0.3831 | 13 | 1.57—2.06 | 0.34±0.08 | 0.472 | 0.79±0.08 |

[a] These two reflections were obtained by subtracting the nuclear intensities from the total observed intensities and are possibly subject to larger errors.

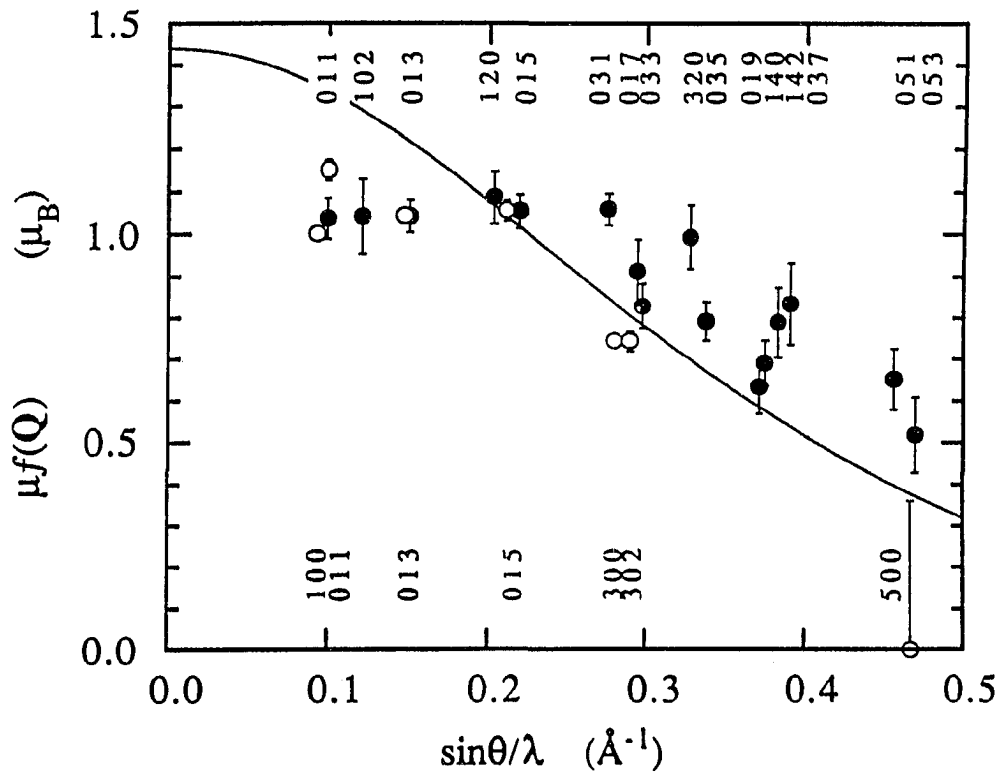


Figure 5.8 The measured $\mu f(\mathbf{Q})$ values for $La_2NiO_4$. For comparison, the experimental data for $La_2CuO_4$ (scaled by a factor four) are also plotted. The solid curve is a fit using an ionic $Ni^{2+}$ form factor. The symbols are: solid circles, $La_2NiO_4$; open circles, $La_2CuO_4$.

## C. Magnetization Density

Given a collinear magnetic structure, the magnetization density may be expressed as a scalar and is given by,

$$M_{exp}(r) = \frac{1}{v_{0m}} \sum_{h,k,\,l=-\infty}^{\infty} [\mu f(Q)]_{exp} \exp\left\{ - i2\pi \left( \frac{h}{a}x + \frac{k}{b}y + \frac{l}{c}z \right) \right\} \quad . \quad (5.2)$$

Due to the limited number of data, the direct transform is not reliable. An alternative is to form the difference density

$$M_{diff}(r) = \frac{1}{v_{0m}} \sum_{h,k,\,l=-\infty}^{\infty} \left\{ [\mu f(Q)]_{exp} - [\mu f(Q)]_{mod} \right\} \exp\left\{ - i2\pi \left( \frac{h}{a}x + \frac{k}{b}y + \frac{l}{c}z \right) \right\} \quad , \quad (5.3)$$

where $[\mu f(Q)]_{mod}$ is the fitting result of a specific model. To minimize the series termination error due to the limited number of data, we averaged [36, 67-68] the difference density over a small box of dimensions $\delta_x \times \delta_y \times \delta_z$. The averaged difference density is given by

$$\overline{M}_{diff}(r) = \frac{1}{v_{0m}} \sum_{h,k,\,l=-\infty}^{\infty} \left\{ [\mu f(Q)]_{exp} - [\mu f(Q)]_{mod} \right\} \exp\left\{ - i2\pi \left( \frac{h}{a}x + \frac{k}{b}y + \frac{l}{c}z \right) \right\} \cdot$$

$$\cdot \frac{\sin(\pi h \delta_x / a)}{\pi h \delta_x / a} \cdot \frac{\sin(\pi k \delta_y / b)}{\pi k \delta_y / b} \cdot \frac{\sin(\pi l \delta_z / c)}{\pi l \delta_z / c} \quad . \quad (5.4)$$

It can be seen that averaging the difference density is essentially multiplying it with a window function.

If M(**r**) is centrosymmetric, as it is for the present compound, the calculation can be much simplified. In such a case, it can be shown that $f(\mathbf{Q})$ is real, i.e.,

$$f(\mathbf{Q})^* = f(\mathbf{Q}) \ , \tag{5.5}$$

and furthermore,

$$f(-\mathbf{Q}) \equiv f(\mathbf{Q})^* = f(\mathbf{Q}) \ . \tag{5.6}$$

It follows that (5.4) can be rewritten as

$$\overline{M}_{diff}(\mathbf{r}) = \frac{8}{v_{0m}} \sum_{h,k,l=0}^{\infty} \left\{[\mu f(\mathbf{Q})]_{exp} - [\mu f(\mathbf{Q})]_{mod}\right\} \cos\left[ - i2\pi \left(\frac{h}{a}x + \frac{k}{b}y + \frac{l}{c}z\right)\right] \cdot$$

$$\cdot \frac{\sin(\pi h\delta_x/a)}{\pi h\delta_x/a} \cdot \frac{\sin(\pi k\delta_y/b)}{\pi k\delta_y/b} \cdot \frac{\sin(\pi l\delta_z/c)}{\pi l\delta_z/c} \ . \tag{5.7}$$

Having established the necessary background information, we now return to the discussion of the experimental data. To obtain some insight regarding the origin of the plateau in the measured form factor, we evaluated the magnetization density corresponding to the difference between the observed density and that predicted by the spherical $Ni^{2+}$ form factor. To minimize series termination errors, the difference density was averaged over a box of dimensions 0.5×0.5×1.0 $Å^3$.

In Figure 5.9 we show the difference magnetization density map in the Ni-O plane. Here all Ni atoms at the corner positions have been defined to have positive density, represented by solid contours. Consequently, because of the antiferromagnetic ordering, the Ni atom at the face-center position has negative density, represented by dashed contours. Since this is a difference density map, there is little density near the Ni atoms.

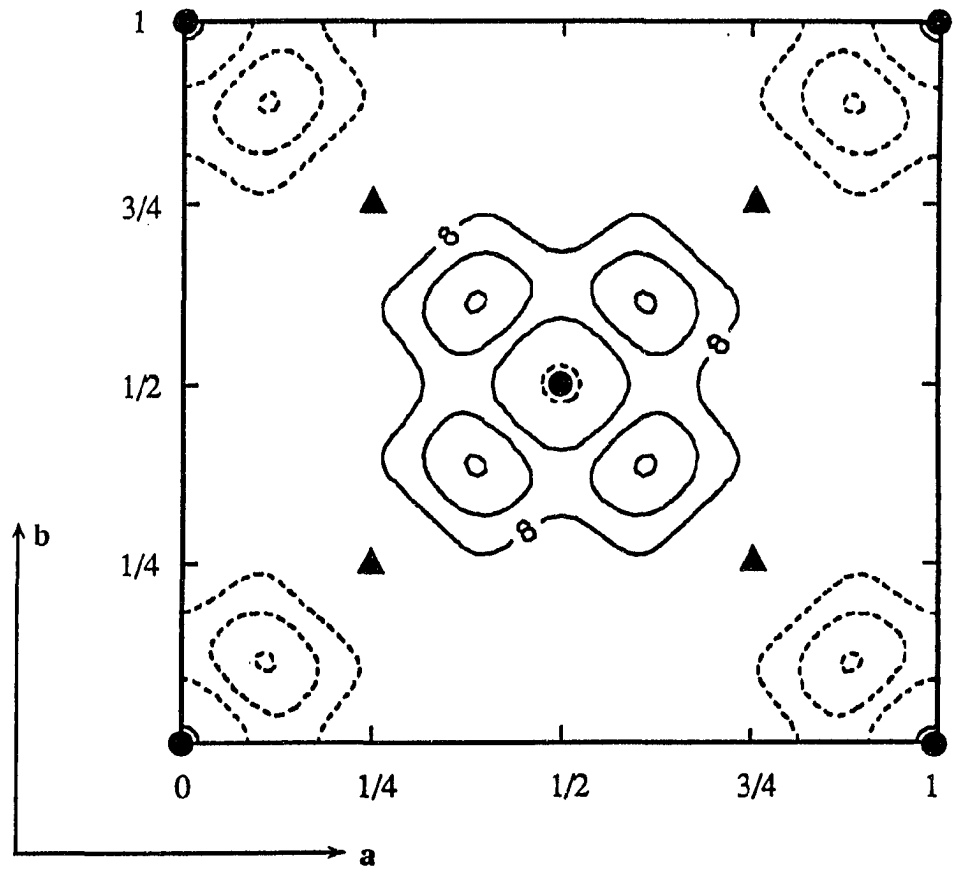


Figure 5.9 The difference magnetization density of $La_2NiO_4$ in the Ni-O plane. The atom symbols are: circles, Ni; triangles, O. The solid and dashed contours denote positive and negative densities, respectively. The Ni atoms at the corner positions have been defined to have positive density. The Ni atom at the face-centered position, which has an antiparallel moment, has negative density.

The main feature of this map is the appearance in the Ni-O plane of *antiparallel* densities around each Ni site. These densities spread along the Ni-O bonds and disappear at the in-plane oxygen sites, as they must because the oxygen is midway between a positive and negative Ni spin. Difference maps in other planes, for instance, the (1 1 0) plane as shown in Figure 5.10, reveal no additional density above the significance level, which is about 1 contour. From this we conclude that the magnetization density corresponding to the experimental data,

$$\mathbf{M}_{exp}(\mathbf{r}) = \mathbf{M}_{mod}(\mathbf{r}) + \overline{\mathbf{M}}_{diff}(\mathbf{r}) \quad . \tag{5.9}$$

is strongly anisotropic and, in particular, contracted along the Ni-O bonds in the Ni-O plane. These observations suggest that the anomalous features of the magnetic form factor could be attributed to covalency effects in the Ni-O plane. Such effects were found to be of significance in many transition compounds [30-32,36,69], such as NiO and $K_2CuF_4$. Detailed modelling of the experimental data will be presented in the next chapter after a complete development of the theory of covalency models.

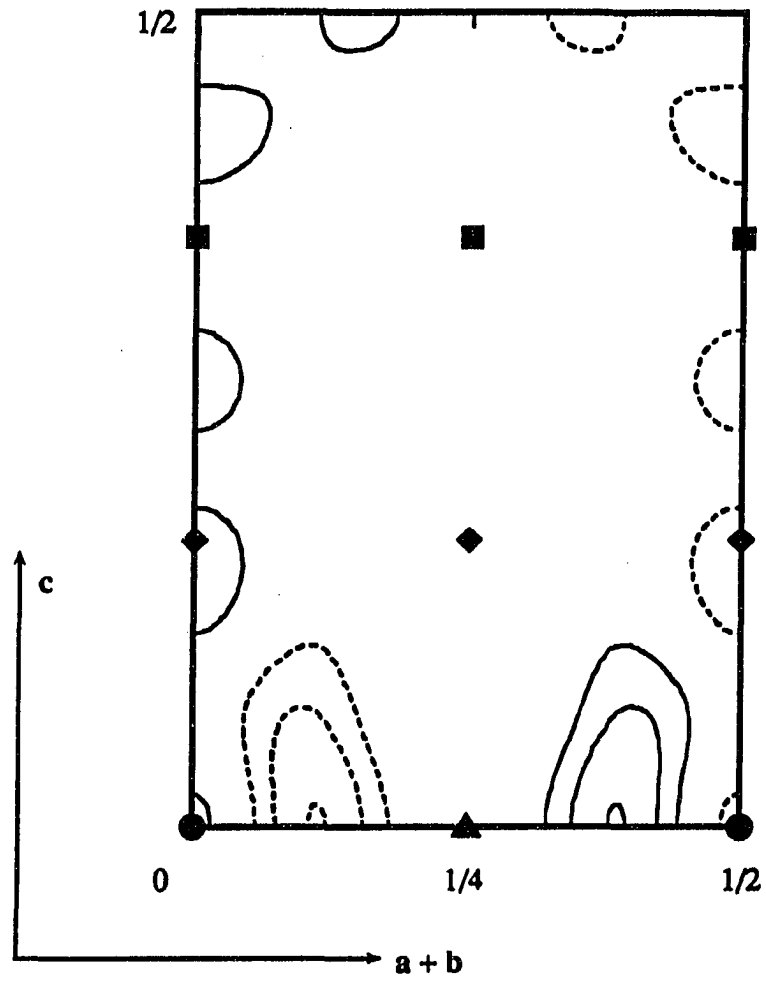


Figure 5.10 The difference magnetization density of $La_2NiO_4$ in the (1 1 0) plane. The atom symbols are: circles, Ni; triangles, in-plane O; squares, La; diamonds, out-of-plane O. The definition of contours is the same as in Figure 5.9.

# VI. COVALENCY EFFECTS

Covalency effects arise from the interaction between the 3d electrons of transition metal ions (e.g., $Cu^{2+}$, $Ni^{2+}$) and the 2p electrons of ligand ions (e.g., $O^-$ and $F^-$). We begin this chapter with a general introduction, then we shall focus our attention on the properties of these outer electrons.

As we discussed in Chapter II, the magnetic amplitude $\mu f(\mathbf{Q})$ measured in neutron diffraction experiments is related to the magnetization density by

$$\mu f(\mathbf{Q}) = \int \mathbf{M}(\mathbf{r}) \exp(i\mathbf{Q}\cdot\mathbf{r})\, d^3\mathbf{r} \quad . \tag{6.1}$$

In general, $\mathbf{M}(\mathbf{r})$ contains two components, one due to the spin and the other due to the orbital angular momentum of the unpaired electrons. In all subsequent discussions, we shall assume: (1) the spin-orbital coupling is negligible, thus the eigenstates are specified by $|sm_s lm\rangle$; (2) the orbital angular momentum does not contribute to the magnetization density. As shall be seen in Section B, these two assumptions are justified for the 3d electrons of transition metal ions and for the 2p electrons of ligand ions in a crystal environment. Then, we are left with only the contribution from the spin. By definition, the magnetization density due to the spin part of unpaired electrons, expressed in Bohr magneton, is given by

$$\mathbf{M}_s(\mathbf{r}) = \sum_\alpha n_{\uparrow,\alpha}\, \rho_{\uparrow,\alpha} - \sum_\alpha n_{\downarrow,\alpha}\, \rho_{\downarrow,\alpha} \quad , \tag{6.2}$$

where $\rho_{\uparrow,\alpha}$ ($\rho_{\downarrow,\alpha}$) is the charge density per unit volume per electron of electrons in the eigenstate $|\uparrow,\alpha\rangle$ ($|\downarrow,\alpha\rangle$), and $n_{\uparrow,\alpha}$ ($n_{\downarrow,\alpha}$) is the number of electrons occupying the $|\uparrow,\alpha\rangle$

( $|\downarrow,\alpha>$ ) state. The total moment is obtained by integrating (6.2) over a Wigner-Seitz cell,

$$\mu = \sum_{\alpha} n_{\uparrow,\alpha} - \sum_{\alpha} n_{\downarrow,\alpha} \quad . \tag{6.3}$$

Substituting (6.2) and (6.3) into (6.1), we obtain the magnetic form factor

$$f(\mathbf{Q}) = \frac{1}{\sum_{\alpha} n_{\uparrow,\alpha} - \sum_{\alpha} n_{\downarrow,\alpha}} \int \left[ \sum_{\alpha} n_{\uparrow,\alpha} \rho_{\uparrow,\alpha} - \sum_{\alpha} n_{\downarrow,\alpha} \rho_{\downarrow,\alpha} \right] \exp(i\mathbf{Q}\cdot \mathbf{r})\ d^3r \quad . \tag{6.4}$$

The form factor defined in this way is normalized to unity at Q = 0.

For any non-degenerate state $|\alpha>$ (either spin-up or spin-down), the charge density is given by

$$\rho_{\alpha} = |\psi_{\alpha}|^2 \quad , \tag{6.5}$$

where $\psi_{\alpha}$ is the wavefunction of $|\alpha>$. But if $|\alpha>$ is degenerate, the right-hand side of (6.5) must be replaced by the average over all degenerated states,

$$\rho_{\alpha} = \frac{1}{d_{\alpha}} \sum_{j=1}^{d_{\alpha}} |\phi_{\alpha,j}|^2 \quad , \tag{6.6}$$

where $d_{\alpha}$ is the degree of degeneracy and $\phi_{\alpha,j}$ (j=1, 2, ..., $d_{\alpha}$) are the basis functions of $|\alpha>$.

## A. Magnetic Form Factor of Free Ions

In the following context, we shall frequently use a term *shell* to represent all energy levels which share all other quantum numbers except m. Obviously, each $l$-shell has $2l+1$ sublevels.

The wavefunction, $\psi_\alpha$, belonging to a given $l$-shell can be expanded as a linear combination of spherical harmonics

$$\psi_\alpha = R_l(r) \cdot \sum_{m=-l}^{l} a_{l\,m}\, Y_{l\,m}(\theta,\varphi) \quad . \tag{6.7}$$

The radial function $R_l(r)$ may be obtained from the the self-consistent Hartree-Fock calculations. In the *restricted* Hartree-Fock method, $R_l(r)$ is shared by all electrons of the same shell. In the *unrestricted* [70] Hartree-Fock method, however, the radial functions for the spin-up and spin-down states are allowed to vary independently, and their difference gives rise to a phenomenon called *spin-polarization* of the shell. Watson and Freeman [70] found that some small spin-polarization effects were present in $Ni^{2+}$ ions; the resulting magnetic form factor was slightly expanded. We have included such effects in all subsequent calculations regarding $Ni^{2+}$ ions. But for other ions, we shall assume the spin-polarization effects are negligible.

To illustrate the procedure of computing the form factor using Equation (6.4), we consider the $l$-shell electrons of a *free* ion. For free ions, all $2l+1$ sublevels are degenerate. If we choose $Y_{lm}$ as the basis functions, the charge density (for both spin-up and spin-down state) is given by

$$\rho = \frac{1}{2l+1} \sum_{m=-l}^{l} R^2(r) \left| Y_{l\,m}(\theta,\varphi) \right|^2 \quad . \tag{6.8}$$

According to the 'sum rule' [71] for the squares of $Y_{lm}$'s,

$$\sum_{m=-l}^{l} \left| Y_{l\,m}(\theta,\varphi) \right|^2 = \frac{2l+1}{4\pi} ,$$

thus the charge density is reduced to

$$\rho = \frac{R^2(r)}{4\pi} , \tag{6.9}$$

which is spherical.

Now substituting (6.9) into (6.4), we obtain

$$f(\mathbf{Q}) = \frac{1}{4\pi} \int R^2(r)\ \exp(i\mathbf{Q}\cdot\mathbf{r})\ d^3\mathbf{r} . \tag{6.10}$$

The integration over $(\theta,\varphi)$ leads to

$$\int \exp(i\mathbf{Q}\cdot\mathbf{r})\ \sin\theta d\theta\ d\varphi = 4\pi \frac{\sin(Qr)}{Qr} , \tag{6.11}$$

therefore,

$$f(\mathbf{Q}) = \int (R(r)\,r)^2\ \frac{\sin(Qr)}{Qr}\ dr . \tag{6.12}$$

It can be seen that the form factor for a free ion is spherical. In practice, it is convenient to define a radial charge density $U^2(r)$, where U(r) is given by

$$U(r) = R(r)\,r . \tag{6.13}$$

With U(r), we may rewrite Equation (6.12) as

$$f(Q) = \int U^2(r) \frac{\sin(Qr)}{Qr} dr \qquad (6.14)$$

In Figure 6.1, we compare the radial charge density of the 3d electrons of $Cu^{2+}$ and $Ni^{2+}$, and the 2p electrons of $O^-$ ions. Figure 6.2 shows the corresponding form factor calculated using Equation (6.12). In Appendix III, we list the values of the calculated magnetic form factors.

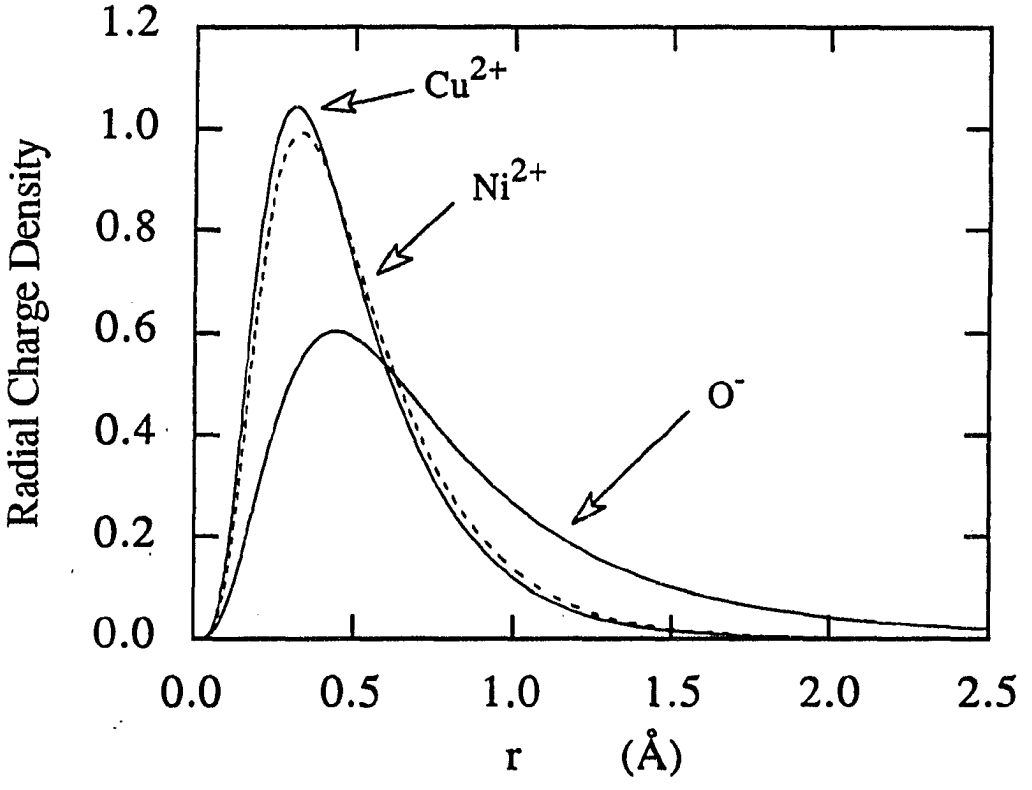


Figure 6.1 The radial charge density of $Cu^{2+}$, $Ni^{2+}$, and $O^-$ free ions.

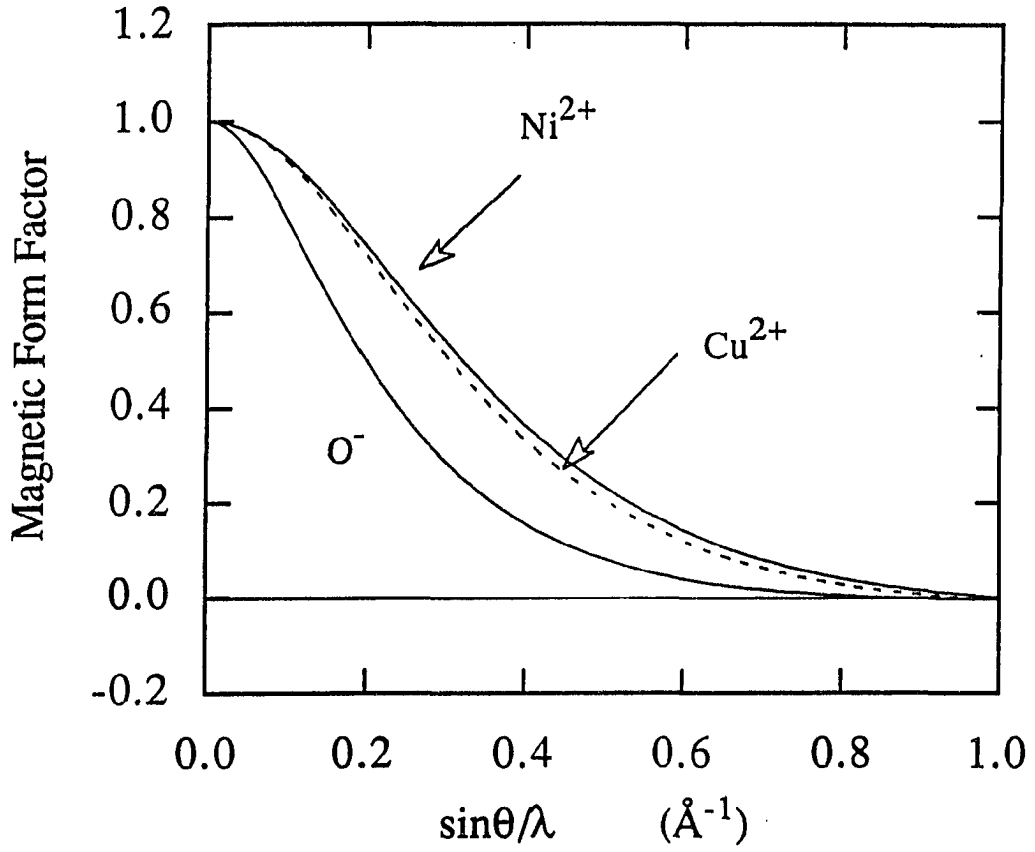


Figure 6.2 The magnetic form factor of $Cu^{2+}$, $Ni^{2+}$, and $O^{-}$ free ions.

## B. Crystal Field Splitting

In solids, the electrons of the outmost shell experience an intense inhomogeneous electric field, known as the *crystal field*, produced by neighboring ions. The impact of the crystal field on the inner shells is largely reduced due to the screening effects of the electrons residing on the outmost shell.

For the 3d electrons of transition metal ions, the interaction with the crystal field is much stronger than the spin-orbital coupling [72]. (Experiments have shown that a typical crystal field excitation in transition metal salts is of the order of 1 eV, whereas the spin-orbital coupling parameter is at most 0.1 eV.) This is also true for the 2p electrons of ligand ions because the 2p wavefunction is broader (Figure 6.1) and, furthermore, the spin-orbital coupling is weaker in lighter elements.

For these outer electrons, to a good approximation, the spin-orbital coupling can be ignored altogether. It follows that the spin and spatial part of the eigenfunctions are separable and the wavefunctions can be expanded on the basis of $|sm_s lm\rangle$. The crystal fields do not have spherical symmetry, but only the symmetry of the crystal sites where the ions are located. Thus, the second consequence resulting from the interaction with crystal fields is that the $2l+1$ sublevels belonging to a given $l$, which would otherwise be degenerate, are now split. The splitting leads to $d_{x^2-y^2}$, $d_{3z^2-r^2}$, $d_{xy}$, $d_{yz}$, and $d_{zx}$ orbitals for the 3d electrons, and $p_x$, $p_y$, and $p_z$ orbitals for the 2p electrons, all named after the angular dependence of their wavefunctions. The explicit expressions for these wavefunctions are compiled in Appendix IV. For these orbitals, it is easy to show that the mean value of *every* component of the orbital angular momentum vanishes. This phenomenon is called *quenching* of the orbital angular momentum. In this case, there is no orbital magnetic moment because such a moment is proportional to the mean value of the component of the orbital angular momentum in the direction of the magnetic field.

Since the 3d and 2p orbitals are linear combinations of $Y_{lm}$'s, the basic integrals that appear in the calculation of the form factor are of the form [73]

$$f_{ij} = \int R^2(r)\; Y^*_{l\,m_i}(\theta,\varphi)\, Y_{l\,m_j}(\theta,\varphi)\; \exp(i\mathbf{Q}\cdot\mathbf{r})\; d^3\mathbf{r} \quad . \qquad (6.15)$$

Denote

$$Y_{l\,m}(\theta,\varphi) = \Theta_{l\,m}(\cos\theta)\,\Phi_m(\varphi) \quad , \tag{6.16}$$

where

$$\Phi_m(\varphi) = \frac{1}{\sqrt{2\pi}}\, e^{i\varphi} \tag{6.17}$$

and $\Theta_{lm}$'s are the associated Legendre functions, and notice

$$\exp(i\mathbf{Q}\cdot\mathbf{r}) = 4\pi \sum_{n=0}^{\infty} \sum_{m=-n}^{n} i^n\, j_n(Qr)\,\Theta_{nm}(\cos\theta)\,\Phi_m(\varphi)\,\Theta_{nm}(\cos\beta)\,\Phi_m(\gamma) \quad , \tag{6.18}$$

where $j_n$'s are the spherical Bessel functions, $\beta$ and $\gamma$ are, respectively, the polar and azimuthal angles of $\mathbf{Q}$. Upon substitution into Equation (6.15) and subsequent integration over $\varphi$, it can be shown

$$f_{ij} = \sqrt{4\pi} \sum_{n=0}^{\infty} i^n \sqrt{2n+1}\, C^n(lm_i,\, lm_j)\, \langle j_n \rangle\, \Theta_{n,\,m_i-m_j}(\cos\beta)\,\Phi_{m_i-m_j}(\gamma) \quad . \tag{6.19}$$

The coefficients $C^n(lm_i,lm_j)$ are given by

$$C^n(lm_i,\, lm_j) = \int_0^{\pi} \left(\frac{2}{2n+1}\right)^{1/2} \Theta_{n,\,m_i-m_j}(\cos\theta)\,\Theta_{lm_i}(\cos\theta)\,\Theta_{lm_j}(\cos\theta)\,\sin\theta d\theta \quad , \tag{6.20}$$

and have been conveniently tabulated by Condon and Shortley [74]. $\langle j_n \rangle$'s are the Bessel transforms of one electron radial charge density and are given by

$$\langle j_n \rangle = \int (R(r)\,r)^2\, j_n(Qr)\, dr \quad . \tag{6.21}$$

In particular, when $n = 0$,

$$j_n(Qr) = j_0(Qr) = \frac{\sin(Qr)}{Qr} \tag{6.22}$$

and (6.21) is identical to (6.12).

Equation (6.19) shows that the form factor of any given orbital can be expanded as a series of $\langle j_n \rangle$ terms. For instance, for the 2p electrons, it is easy to show that the form factors of $p_x$, $p_y$, and $p_z$ orbitals are, respectively, given by

$$f_x(Q) = \langle j_0 \rangle + P_2(\cos\beta)\langle j_2 \rangle + \frac{3}{2}\sin^2\beta\cos(2\gamma)\langle j_2 \rangle \ , \tag{6.23}$$

$$f_y(Q) = \langle j_0 \rangle + P_2(\cos\beta)\langle j_2 \rangle - \frac{3}{2}\sin^2\beta\cos(2\gamma)\langle j_2 \rangle \ , \tag{6.24}$$

$$f_z(Q) = \langle j_0 \rangle - 2P_2(\cos\beta)\langle j_2 \rangle \ . \tag{6.25}$$

The application of these expansions has greatly simplified the form factor calculations, because $\langle j_n \rangle$'s are 1-dimensional integrals and much easier to compute.

Two conclusions can be quickly drawn from Equation (6.19). First, the spherically averaged form factor of any given orbital is equal to $\langle j_0 \rangle$. Second, the averaged form factor (over all $2l+1$ sublevels) of a given $l$-shell is equal to $\langle j_0 \rangle$. These two statements can be easily verified for the 2p electrons by using Equations (6.23)-(6.25).

We now wish to make a comment on the form factor of free ions calculated in Section A. By *free* we mean that ions experience zero external field. This is, however, paradoxical. In the absence of crystal field, the spin-orbital coupling can no longer be neglected. And, the eigenstates will be specified by the total angular momentum and its projection rather than $|sm_s lm\rangle$ as we have been using. Therefore the entire calculations are based on a self-conflicting assumption. From the above discussion, it is clear that the form factor calculated this way will be meaningful only if it is interpreted as the

spherically averaged form factor of a given orbital or the averaged form factor of a given shell.

In Chapter V, we showed that the measured form factor of $La_2NiO_4$ was poorly fitted by the spherical $Ni^{2+}$ form factor. However, such a comparison is inadequate, because the $Ni^{2+}$ ions are in a crystal environment and we have not yet considered the crystal field effects. In $La_2NiO_4$, the 3d orbitals split according to the tetragonal symmetry of the Ni sites (Figure 6.3). For each $Ni^{2+}$ ion, there are two unpaired electrons occupying the upper $d_{x^2-y^2}$ and $d_{3z^2-r^2}$ orbitals, respectively. Here, we take the x and y axes along the directions from a Ni to one of the nearest-neighbor in-plane oxygen atom, and the z axis parallel to c-axis. Using (6.19), we obtain the form factor for the $d_{x^2-y^2}$ and $d_{3z^2-r^2}$ orbitals,

$$f_{x^2-y^2}(\mathbf{Q}) = \langle j_0 \rangle + \frac{10}{7} P_2(\cos\beta) \langle j_2 \rangle + \frac{3}{7} P_4(\cos\beta) \langle j_4 \rangle + \frac{15}{8} \sin^4\beta \cos(4\gamma) \langle j_4 \rangle , \tag{6.26}$$

$$f_{3z^2-r^2}(\mathbf{Q}) = \langle j_0 \rangle - \frac{10}{7} P_2(\cos\beta) \langle j_2 \rangle + \frac{18}{7} P_4(\cos\beta) \langle j_4 \rangle . \tag{6.27}$$

In Figure 6.4 we compare the $\langle j_0 \rangle$, $\langle j_2 \rangle$, and $\langle j_4 \rangle$ term of a $Ni^{2+}$ ion using the radial charge density obtained from free ionic calculations. As can be seen, the $\langle j_4 \rangle$ term is largely negligible in the Q range covered in the present experiment ($\sin\theta/\lambda \leq 0.5$ Å$^{-1}$ ). Ignoring $\langle j_4 \rangle$, we obtain the magnetic amplitude (this is the quantity that should be compared with the experimental data)

$$\begin{aligned} \mu f &= \mu_{x^2-y^2} f_{x^2-y^2} + \mu_{3z^2-r^2} f_{3z^2-r^2} \\ &= (\mu_{x^2-y^2} + \mu_{3z^2-r^2}) \langle j_0 \rangle + (\mu_{x^2-y^2} - \mu_{3z^2-r^2}) \frac{10}{7} P_2(\cos\beta) \langle j_2 \rangle . \end{aligned} \tag{6.28}$$

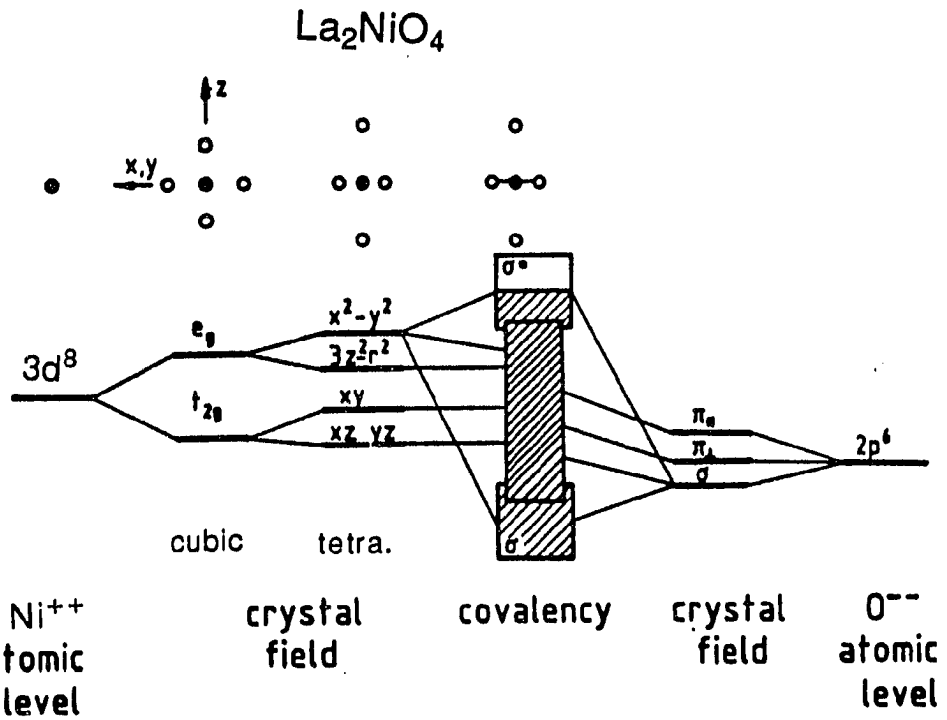


Figure 6.3 Schematic picture of the crystal field splitting of the Ni 3d and O 2p orbitals in $La_2NiO_4$. In the center is the bonding complex of bands arising from the hybridization between Ni 3d and O 2p orbitals. Specifically, the separation of the bonding (bottom) and antibonding (top) $\sigma$ bands (due to the Ni $3d_{x^2-y^2}$ and the in-plane O $2p_{x,y}$ orbitals) is illustrated. (Adapted after Ref. 26)

Clearly, unless $\mu_{x^2-y^2} = \mu_{3z^2-r^2}$, the magnetic amplitude is no longer spherical but modified by an angular dependent $\langle j_2 \rangle$ term. The fit to the data using this form factor is, however, only marginally better than the one obtained using the spherical $Ni^{2+}$ form factor (the $\chi^2$ is reduced from 10.7 to 9.9). This result can be rather easily understood if

one notices that the $<j_2>$ term is significant only for $\sin\theta/\lambda \geq 0.25$ Å$^{-1}$. While the addition of this term improves the fit slightly (Figure 6.5) for $\sin\theta/\lambda \geq 0.25$ Å$^{-1}$, it fails to account for the plateau at low Q values, which is the primary feature of the experimental data. We may also look at this result from the real space perspective. As we know, the spin density of $d_{3z^2-r^2}$ is isotropic in the Ni-O plane, whereas that of $d_{x^2-y^2}$ is anisotropic with maxima along the x and y axes. Therefore, any combination of these two orbitals will lead to a magnetization density with maxima along the x and y axes, a result which is in contrast to the experimental observations (see Figure 5.9). We believe the observed plateau is due to the covalency effects to be addressed below.

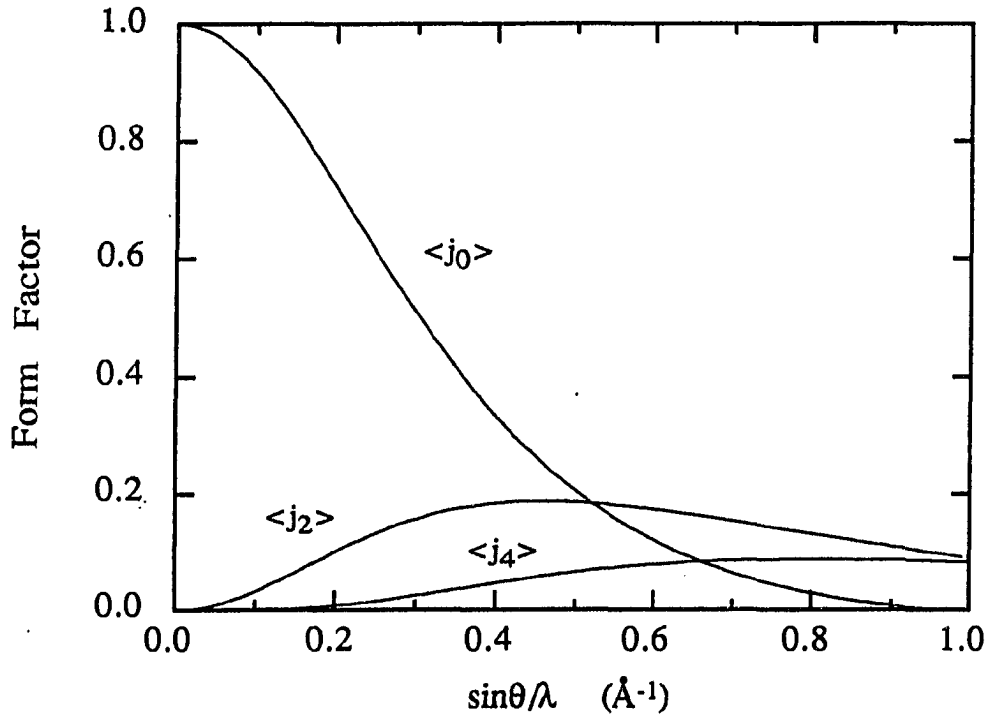


Figure 6.4 The $<j_0>$, $<j_2>$, and $<j_4>$ term of a $Ni^{2+}$ ion.

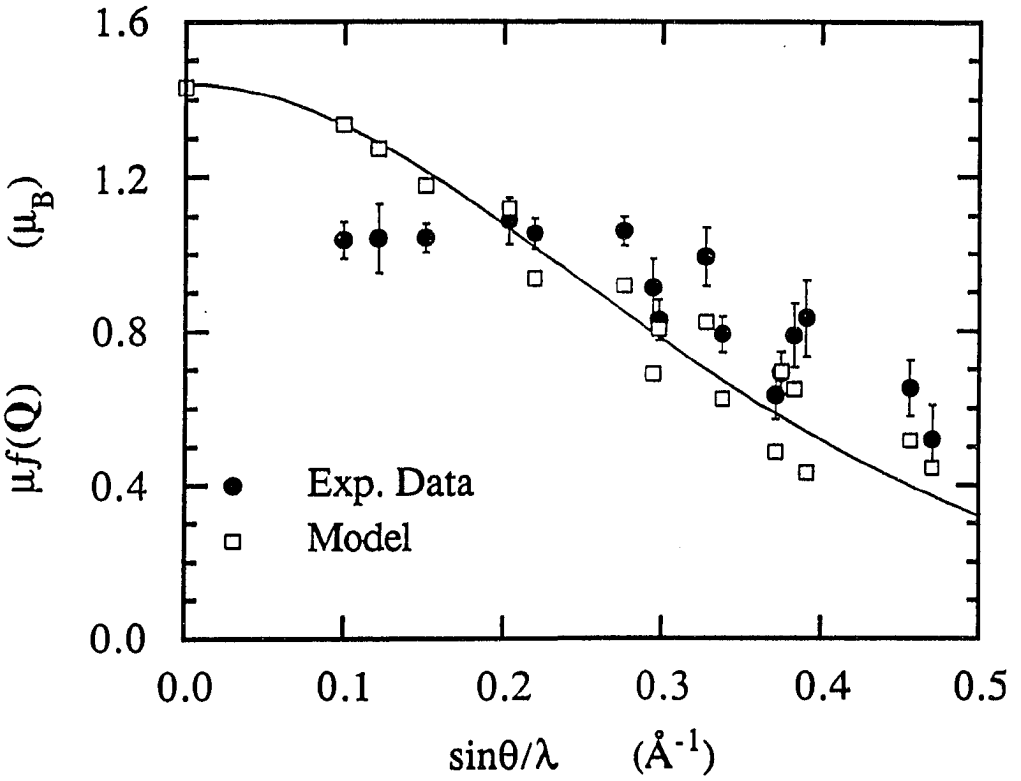


Figure 6.5 Least-squares fit to the experimental data of $La_2NiO_4$ using a simple superposition of the $d_{x^2-y^2}$ and $d_{3z^2-r^2}$ orbitals. For comparison, the spherical $Ni^{2+}$ form factor is also shown (solid curve).

## C. Covalency Effects

To assess the importance of including the covalency effects, we form the antibonding wavefunctions for the Ni $d_{x^2-y^2}$ and $d_{3z^2-r^2}$ orbitals combined with the O $2p_\alpha$ ($\alpha$=x,y,z) orbitals, noticing that for the $d_{x^2-y^2}$ orbital only the in-plane oxygen atoms need to be included. The configurations of these wavefunctions are schematically shown in

Figures 6.6 and 6.7. Since the crystal field has tetragonal symmetry, the antibonding wavefunctions can be written as

$$\psi_{x^2-y^2}(\mathbf{r}) = N_{x^2-y^2}\{d_{x^2-y^2}(\mathbf{r}) + A_{x^2-y^2}[p_x(\mathbf{r}-x_0\mathbf{i}) - p_x(\mathbf{r}+x_0\mathbf{i}) + p_y(\mathbf{r}-y_0\mathbf{j}) - p_y(\mathbf{r}+y_0\mathbf{j})]\} \quad (6.29)$$

and

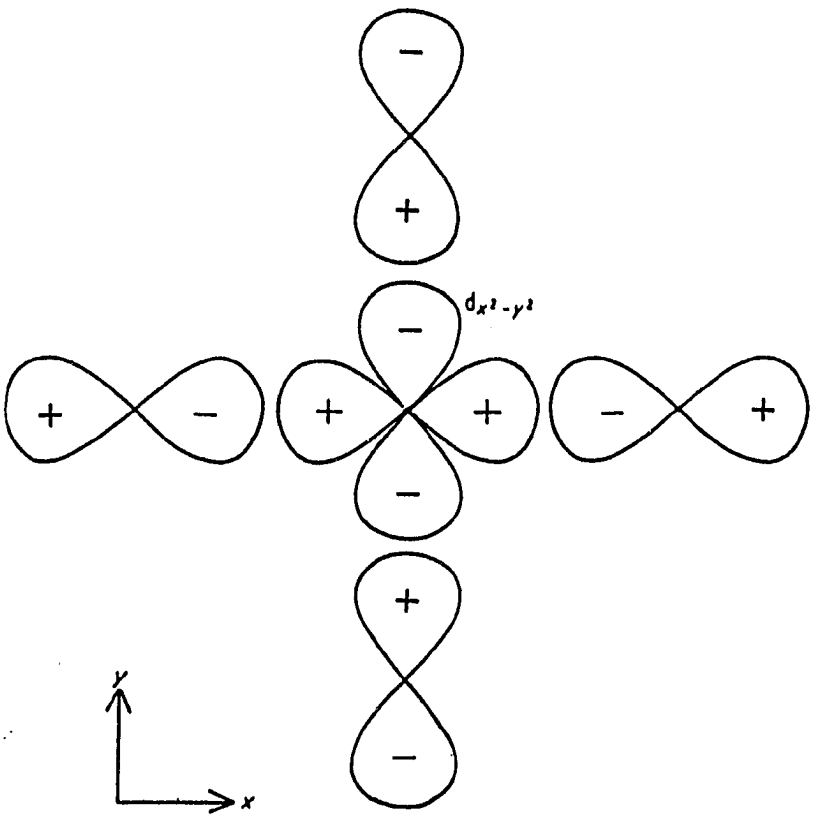


Figure 6.6 Configuration of the wavefunctions for the antibonding $d_{x^2-y^2}$ orbital.

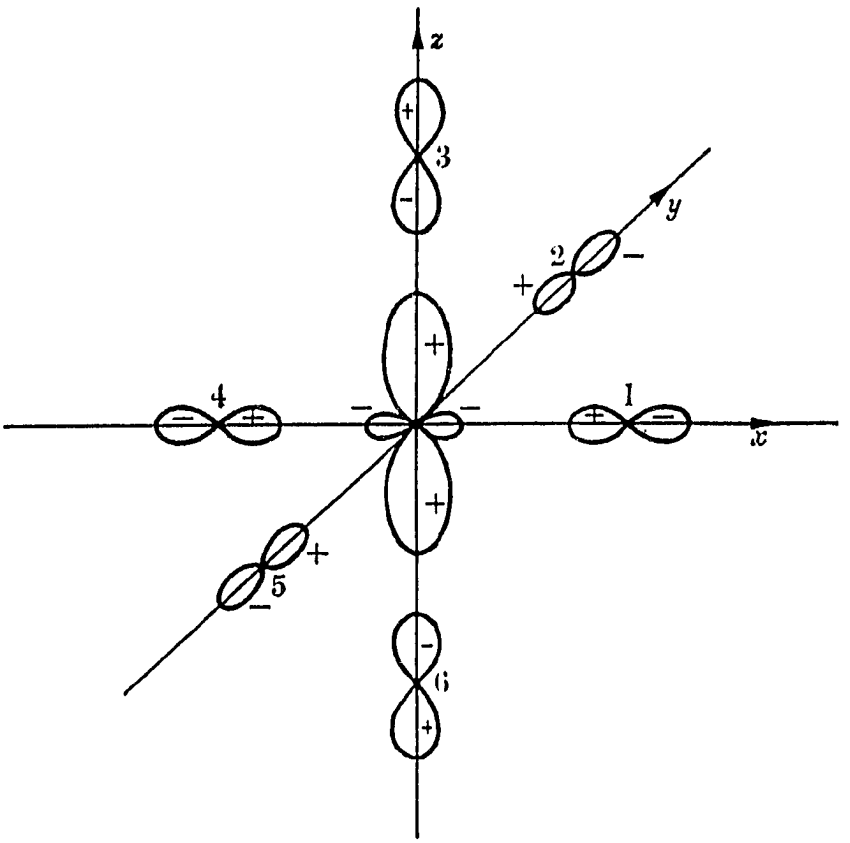


Figure 6.7 Configuration of the wavefunctions for the antibonding $d_{3z^2-r^2}$ orbital.

$$\psi_{3z^2-r^2}(\mathbf{r}) = N_{3z^2-r^2}\{d_{3z^2-r^2}(\mathbf{r}) + A^{//}_{3z^2-r^2}[-p_x(\mathbf{r}-x_0\mathbf{i}) + p_x(\mathbf{r}+x_0\mathbf{i}) - p_y(\mathbf{r}-y_0\mathbf{j}) + p_y(\mathbf{r}+y_0\mathbf{j})] + A^{\perp}_{3z^2-r^2}[p_z(\mathbf{r}-z_0\mathbf{k}) - p_z(\mathbf{r}+z_0\mathbf{k})]\} \quad (6.30)$$

In the above equations, A's are the mixing parameters, $p_\alpha(\mathbf{r}-\mathbf{r}_i)$ is the oxygen 2p wavefunction centered at $\mathbf{r}_i$ with the polarization vector along the $\alpha$-axis, and N's are the

normalization constants. For $d_{3z^2-r^2}$, // and ⊥ denote the in-plane and out-of-plane contributions, respectively.

Ignoring the cross terms between different 2p orbitals, we obtain the spin densities

$$S_{x^2-y^2}(\mathbf{r}) = N^2_{x^2-y^2}\Big\{d^2_{x^2-y^2}(\mathbf{r}) + 2A_{x^2-y^2}d_{x^2-y^2}(\mathbf{r})\left[p_x(\mathbf{r}-x_0\mathbf{i}) - p_x(\mathbf{r}+x_0\mathbf{i}) + p_y(\mathbf{r}-y_0\mathbf{j}) - p_y(\mathbf{r}+y_0\mathbf{j})\right] + A^2_{x^2-y^2}\left[p^2_x(\mathbf{r}-x_0\mathbf{i}) + p^2_x(\mathbf{r}+x_0\mathbf{i}) + p^2_y(\mathbf{r}-y_0\mathbf{j}) + p^2_y(\mathbf{r}+y_0\mathbf{j})\right]\Big\} \quad (6.31)$$

and

$$S_{3z^2-r^2}(\mathbf{r}) = N^2_{3z^2-r^2}\Big\{d^2_{3z^2-r^2}(\mathbf{r}) + 2A^{//}_{3z^2-r^2}d_{3z^2-r^2}(\mathbf{r})\left[-p_x(\mathbf{r}-x_0\mathbf{i}) + p_x(\mathbf{r}+x_0\mathbf{i}) - p_y(\mathbf{r}-y_0\mathbf{j}) + p_y(\mathbf{r}+y_0\mathbf{j})\right] + 2A^{\perp}_{3z^2-r^2}d_{3z^2-r^2}(\mathbf{r})\left[p_z(\mathbf{r}-z_0\mathbf{k}) - p_z(\mathbf{r}+z_0\mathbf{k})\right] + \left(A^{//}_{3z^2-r^2}\right)^2\left[p^2_x(\mathbf{r}-x_0\mathbf{i}) + p^2_x(\mathbf{r}+x_0\mathbf{i}) + p^2_y(\mathbf{r}-y_0\mathbf{j}) + p^2_y(\mathbf{r}+y_0\mathbf{j})\right] + \left(A^{\perp}_{3z^2-r^2}\right)^2\left[p^2_z(\mathbf{r}-z_0\mathbf{k}) + p^2_z(\mathbf{r}+z_0\mathbf{k})\right]\Big\}. \quad (6.32)$$

The normalization constants are obtained by normalizing the spin density distributions to unity,

$$N_{x^2-y^2} = \left[1 + 8A_{x^2-y^2}S_{x^2-y^2} + 4A^2_{x^2-y^2}\right]^{-\frac{1}{2}} \quad (6.33)$$

and

$$N_{3z^2-r^2} = \left[1 + 8A^{//}_{3z^2-r^2}S^{//}_{3z^2-r^2} + 4\left(A^{//}_{3z^2-r^2}\right)^2 + 4A^{\perp}_{3z^2-r^2}S^{\perp}_{3z^2-r^2} + 2\left(A^{\perp}_{3z^2-r^2}\right)^2\right]^{-\frac{1}{2}}. \quad (6.34)$$

where S's are the overlap integrals and given by, respectively,

$$S_{x^2-y^2} = \langle d_{x^2-y^2}(\mathbf{r}) \mid p_x(\mathbf{r}-x_0\mathbf{i}) \rangle \quad , \tag{6.35}$$

$$S^{//}_{3z^2-r^2} = \langle d_{3z^2-r^2}(\mathbf{r}) \mid p_x(\mathbf{r}+x_0\mathbf{i}) \rangle \quad , \tag{6.36}$$

and

$$S^{\perp}_{3z^2-r^2} = \langle d_{3z^2-r^2}(\mathbf{r}) \mid p_z(\mathbf{r}-z_0\mathbf{k}) \rangle \quad . \tag{6.37}$$

As can be seen from Figures 6.6 and 6.7, all S's are negative for antibonding orbitals.

The total magnetization density is given by

$$M(\mathbf{r}) = m_{x^2-y^2} S_{x^2-y^2}(\mathbf{r}) + m_{3z^2-r^2} S_{3z^2-r^2}(\mathbf{r}) \quad , \tag{6.38}$$

where $m_{x^2-y^2}$ and $m_{3z^2-r^2}$ are, respectively, the moments of $d_{x^2-y^2}$ and $d_{3z^2-r^2}$ orbitals of a $Ni^{2+}$ in the absence of any covalency effects. It can be seen from Equations (6.31) and (6.32) that the covalency effects result in two additional terms in the magnetization density. The first term is the overlap density due to d-p overlap and the second term is the spin density induced on the oxygen sites as a result of covalency. The overlap density is negative and has a relatively broad spatial extent, thus it gives a negative contribution to the $\mu f(\mathbf{Q})$ at low Q-values and makes it appear flat. The induced spin density on the oxygen sites, on the other hand, is positive and is of O 2p character, which is much more spatially extended than the Ni 3d density, and therefore, contributes only to the innermost reflections.

In such an antiferromagnet as $La_2NiO_4$ , the covalency effects have another consequence: the reduction of the ordered moment. For this compound, the induced moments on the in-plane oxygen sites, which are located in the middle of two antiferromagnetically coupled Ni moments, cancel. Therefore we obtain,

$$M(\mathbf{r}) = m_{x^2-y^2} N^2_{x^2-y^2} \Big\{ d^2_{x^2-y^2}(\mathbf{r}) +$$

$$+ 2 A_{x^2-y^2} d_{x^2-y^2}(\mathbf{r}) [p_x(\mathbf{r}-x_0\mathbf{i}) - p_x(\mathbf{r}+x_0\mathbf{i}) + p_y(\mathbf{r}-y_0\mathbf{j}) - p_y(\mathbf{r}+y_0\mathbf{j})] \Big\} +$$

$$m_{3z^2-r^2} N^2_{3z^2-r^2} \Big\{ d^2_{3z^2-r^2}(\mathbf{r}) +$$

$$+ 2 A^{//}_{3z^2-r^2} d_{3z^2-r^2}(\mathbf{r}) [- p_x(\mathbf{r}-x_0\mathbf{i}) + p_x(\mathbf{r}+x_0\mathbf{i}) - p_y(\mathbf{r}-y_0\mathbf{j}) + p_y(\mathbf{r}+y_0\mathbf{j})]$$

$$+ 2 A^{\perp}_{3z^2-r^2} d_{3z^2-r^2}(\mathbf{r}) [p_z(\mathbf{r}-z_0\mathbf{k}) - p_z(\mathbf{r}+z_0\mathbf{k})]$$

$$+ \left(A^{\perp}_{3z^2-r^2}\right)^2 [p^2_z(\mathbf{r}-z_0\mathbf{k}) + p^2_z(\mathbf{r}+z_0\mathbf{k})] \Big\} . \qquad (6.39)$$

And the net ordered moments are now given by

$$\mu_{x^2-y^2} = m_{x^2-y^2}\left[1 - 4 A^2_{x^2-y^2} N^2_{x^2-y^2}\right] \qquad (6.40)$$

and

$$\mu_{3z^2-r^2} = m_{3z^2-r^2}\left[1 - 4 \left(A^{//}_{3z^2-r^2}\right)^2 N^2_{3z^2-r^2}\right] , \qquad (6.41)$$

as compared to $m_{x^2-y^2}$ and $m_{3z^2-r^2}$, the moments in the absence of covalency effects.

The above discussions are based upon tetragonal crystal symmetry. For the antibonding $d_{x^2-y^2}$ and $d_{3z^2-r^2}$ orbitals, there are totally five independent parameters: the moments $m_{x^2-y^2}$ and $m_{3z^2-r^2}$, and three mixing parameters $A_{x^2-y^2}$, $A^{//}_{3z^2-r^2}$, and $A^{\perp}_{3z^2-r^2}$. In a crystal field of higher symmetry, the number of parameters will be reduced. For instance, in a crystal field of cubic symmetry, it can be shown [69],

$$m_{x^2-y^2} = m_{3z^2-r^2} \qquad (6.42)$$

and

$$A^{\perp}_{3z^2-r^2} = 2\,A^{//}_{3z^2-r^2} = \frac{2}{\sqrt{3}} A_{x^2-y^2} \quad , \tag{6.43}$$

and the number of independent parameters is reduced to two. This is the situation encountered in NiO.

## D. Analysis of the Experimental Data of $La_2NiO_4$

Now we shall apply the covalency models to the experimental data of $La_2NiO_4$. In the theory developed above, there are totally five fitting parameters. Due to the limited number of data, various constraints were imposed in fitting the experimental data to limit the number of parameters involved. In all cases, the fit to the experimental data improved over that obtained using a simple superposition of the $d_{x^2-y^2}$ and $d_{3z^2-r^2}$ orbitals. For instance, by imposing the constraint $m_{x^2-y^2} + m_{3z^2-r^2} = 2.2\ \mu_B$, the $\chi^2$ is reduced from 9.9 to 6.7. The results for this particular model are given in Figure 6.8 and Table IX. The fit suggests that the in-plane oxygen atoms strongly mix with the $d_{x^2-y^2}$ orbital, resulting in a much smaller moment on the antibonding $d_{x^2-y^2}$ orbital than the antibonding $d_{3z^2-r^2}$ orbital.

Interestingly, we find that an excellent fit to the experimental data can be obtained (Figure 6.9) if one assumes an antibonding orbital arising from a spherical Ni 3d mixed with O $2p_\alpha$ ($\alpha$=x, y, z) orbitals. As shown in Table IX, the fit with this model also suggests a predominant mixing from the in-plane oxygen atoms, which is rather consistent with our preceding analysis. The problem with this model is that it is difficult to justify the use of the spherical 3d wavefunction. Therefore, we shall not continue to explore the meaning of this particular fit but merely show the results in Figure 6.9 and Table IX.

The above models demonstrate that the magnetization density about the Ni sites deviates from that expected for an isotropic $Ni^{2+}$ ion. However, the models are rudimentary. While this simplifies the quantitative analysis, one should question the effects of the approximations of the models. For example, the antibonding phase relationship chosen between Cu and O orbitals is strictly only valid for states at the X point in the Brillouin zone. Also, the radial part of the fitting functions were taken from free ion calculations and clearly could be adopted to the environment in the solid to obtain a better fit.

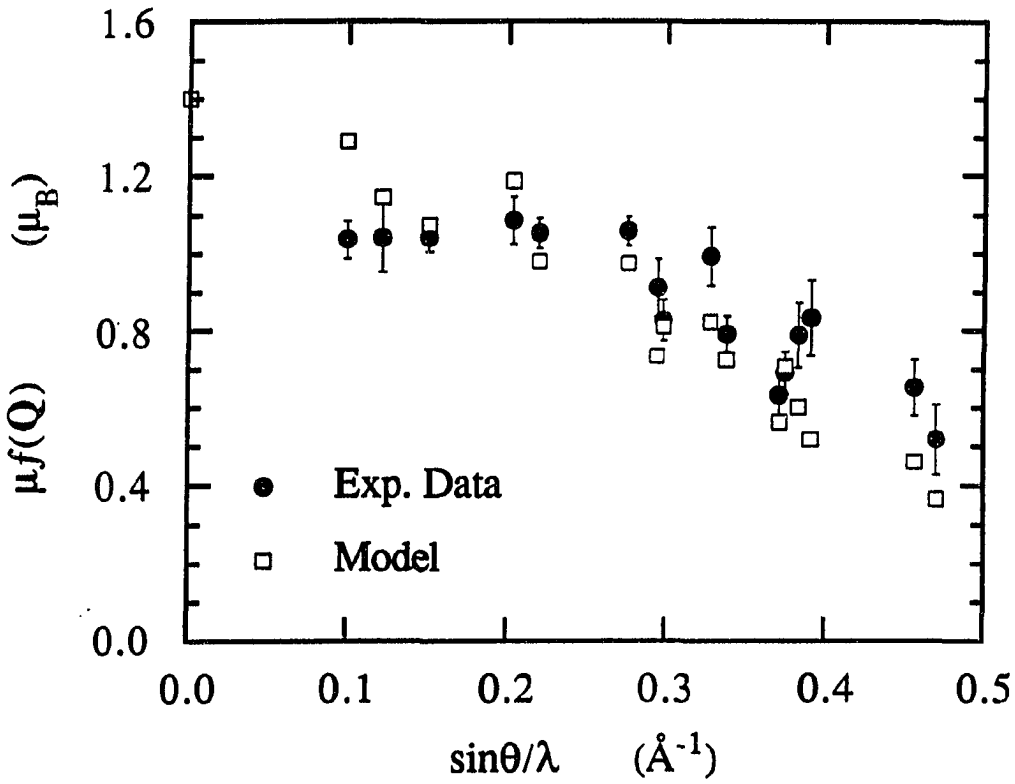


Figure 6.8 Least-squares fit to the experimental data of $La_2CuO_4$ using a covalency model consisting of two antibonding orbitals constructed from a $d_{x^2-y^2}$ and a $d_{3z^2-r^2}$ mixed, respectively, with O $2p_\alpha$ ($\alpha$=x, y, z) orbitals.

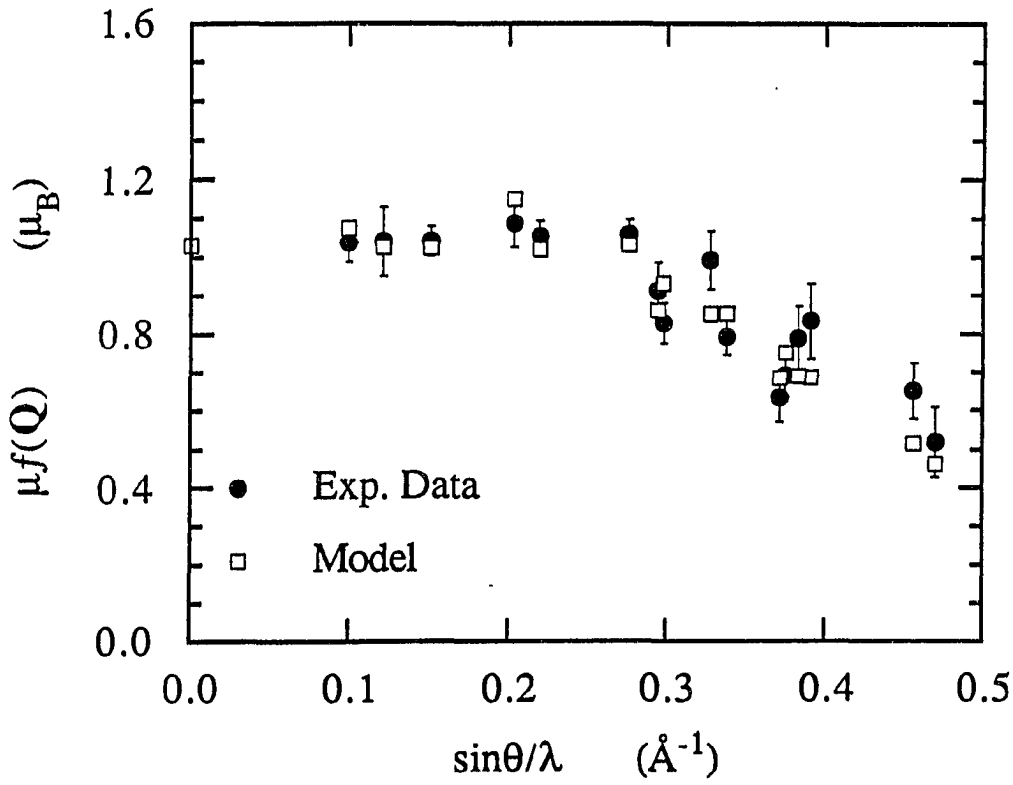


Figure 6.9 Least-squares fit to the experimental data of $La_2NiO_4$ using a covalency model arising from a spherical Ni 3d mixed with O $2p_\alpha$ ($\alpha$=x,y,z) orbitals.

To eliminate some of the arbitrariness, it would of course be desirable to perform first-principle band calculations. For calculating spin densities in many magnetically ordered crystals, first-principle spin-polarized band theoretical methods have proven very successful. However, in systems having strong intra-atomic Coulomb correlations, the usual density functional approach is inadequate. For example, band theory is unable [27] to stabilize the antiferromagnetic ground state of $La_2CuO_4$. For $La_2NiO_4$, an antiferromagnetic state is obtained [75], whose the moment is very sensitive to structural

Table IX. Least-squares fits to the experiment data of $La_2NiO_4$ with various models and band-theoretical calculations: (1) spherical 3d; (2) $d_{x^2-y^2}$ and $d_{3z^2-r^2}$ orbitals; (3) $d_{x^2-y^2}$ and $d_{3z^2-r^2}$ orbitals including covalency effects, and with the constraint $m_{x^2-y^2} + m_{3z^2-r^2} = 2.2\ \mu_B$; (4) LAPW band calculations; (5) spherical 3d orbital with covalency effects. The band results have been scaled by a factor 2.9, because the calculated moment is too small. A's are the mixing parameters, m's are the moments of a $Ni^{2+}$ ion in the absence of covalency effects, and μ's are the net ordered moments. The standard deviations of the fitting parameters are computed from the covariant matrix and may not reflect the actual confidence level of the fitting parameters.

| (h k *l*) | sinθ/λ (Å$^{-1}$) | $\mu f(Q)$ ($\mu_B$) | (1) | (2) | (3) | (4) | (5) |
|---|---|---|---|---|---|---|---|
| (0 1 1) | 0.0993 | 1.04± 0.05 | 1.33 | 1.34 | 1.29 | 1.38 | 1.08 |
| (0 1 3) | 0.1505 | 1.04±0.04 | 1.21 | 1.18 | 1.08 | 0.94 | 1.03 |
| (0 1 5) | 0.2196 | 1.06±0.04 | 1.01 | 0.94 | 0.98 | 1.03 | 1.02 |
| (0 1 7) | 0.2943 | 0.91±0.08 | 0.79 | 0.69 | 0.74 | 0.80 | 0.86 |
| (0 1 9) | 0.3712 | 0.63±0.07 | 0.58 | 0.49 | 0.56 | 0.51 | 0.69 |
| (0 3 1) | 0.2755 | 1.06±0.04 | 0.85 | 0.92 | 0.98 | 0.96 | 1.03 |
| (0 3 3) | 0.2979 | 0.83±0.06 | 0.78 | 0.80 | 0.81 | 0.62 | 0.93 |
| (0 3 5) | 0.3381 | 0.79±0.05 | 0.67 | 0.62 | 0.73 | 0.68 | 0.85 |
| (0 3 7) | 0.3907 | 0.83±0.10 | 0.54 | 0.43 | 0.52 | 0.51 | 0.69 |
| (1 2 0) | 0.2032 | 1.09±0.06 | 1.06 | 1.12 | 1.19 | 1.34 | 1.05 |
| (3 2 0) | 0.3277 | 0.99±0.08 | 0.70 | 0.82 | 0.82 | 0.98 | 0.85 |

| | | | | | | | |
|---|---|---|---|---|---|---|---|
| (1 4 0) | 0.3747 | 0.69±0.06 | 0.58 | 0.70 | 0.71 | 0.78 | 0.75 |
| (0 5 1) | 0.4561 | 0.65±0.08 | 0.40 | 0.52 | 0.46 | 0.50 | 0.52 |
| (0 5 3) | 0.4699 | 0.52±0.09 | 0.37 | 0.45 | 0.37 | 0.32 | 0.46 |
| (1 0 2) | 0.1211 | 1.04±0.09 | 1.29 | 1.27 | 1.15 | 1.08 | 1.03 |
| (1 4 2) | 0.3831 | 0.79±0.08 | 0.56 | 0.65 | 0.60 | 0.56 | 0.69 |
| reduced $\chi^2$ | | | 10.7 | 9.9 | 6.7 | 9.3 | 1.7 |
| Overlap Integrals | | | — | — | $S^{//}_{3z^2-r^2} = -0.0310$<br>$S^{\perp}_{3z^2-r^2} = -0.0445$<br>$S_{x^2-y^2} = -0.0541$ | — | $S^{//} = -0.1733$<br>$S^{\perp} = -0.1271$ |
| Mixing Parameters | | | — | — | $A^{//}_{3z^2-r^2} = 0.13\pm0.15$<br>$A^{\perp}_{3z^2-r^2} = 0.28\pm0.05$<br>$A_{x^2-y^2} = 0.55\pm0.11$ | — | $A^{//} = 0.34\pm0.03$<br>$A^{\perp} = 0.13\pm0.04$ |
| Moments ($\mu_B$) | | | — | — | $m_{3z^2-r^2} = 1.01\pm0.09$<br>$m_{x^2-y^2} = 1.19$ | — | $m = 1.97\pm0.13$ |
| Net ordered Moments ($\mu_B$) | $\mu_{3z^2-r^2}$ | | | 1.08 | 0.95 | 0.78 | |
| | $\mu_{x^2-y^2}$ | | | 0.35 | 0.45 | 0.52 | |
| | $\mu$ | | 1.44 | 1.43 | 1.40 | 1.38 | 1.03 |

changes. To determine whether the magnetic ground state obtained from the first-principle spin-polarized band theory can provide any further insight on the measured form factor, Leung et al. [76] performed such calculations using the scalar relativistic linear augmented plane wave (LAPW) method. The calculations did converge to an antiferromagnetic ground state, but with a moment of only 0.45 $\mu_B$ inside each Ni muffin-tin sphere. This is too small, and reflects the problem with the local-density approximation (LDA) in treating the strong intra-atomic correlations. The band structure is very similar to that obtained by Guo and Temmerman [75], and the large hybridization between 3d and 2p orbitals is similar to that obtained for $La_2CuO_4$ [27]. The large oxygen contribution to the antibonding bands near $E_F$ results in some contraction of the Ni spin density along the Ni-O bond direction, which is consistent with the picture inferred from the simple covalency models. Thus, in spite of the small moment, one might expect the basic shape of the electronic spin densities to be reasonably calculated. Indeed, by simply scaling the theoretical spin density by a factor of 2.9, a rather decent fit to the experimental data is obtained (see Figure 6.10).

The comparison between the experimental form factor and the one obtained from the band-structure calculations also suggests the kind of improvements needed for theories which go beyond band theory in treating the strong on-site correlation. The calculated anisotropy for the larger reflections agrees well with the experiment and arises from a 60%-40% contribution of states with Ni $d_{3z^2-r^2}$ and Ni $d_{x^2-y^2}$ character, respectively. The larger moment is associated with the $d_{3z^2-r^2}$ orbital because there is stronger covalent bonding between the $d_{x^2-y^2}$ orbitals and the in-plane oxygen orbitals than for the $d_{3z^2-r^2}$ orbital with the out-of-plane oxygen $p_z$ orbitals. The stronger bonding causes a greater band width and the magnetic interactions are less effective (a situation

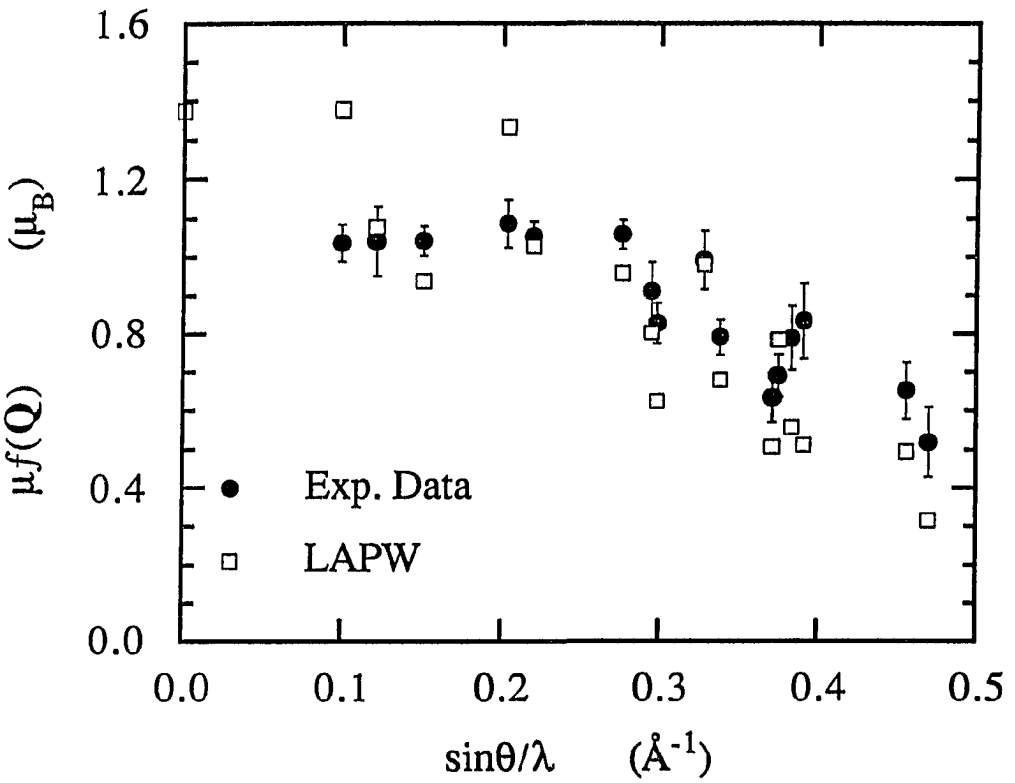


Figure 6.10 Comparison of the experimental data of $La_2NiO_4$ with spin-polarized band calculations. The band result has been multiplied by a factor of 2.9 because the calculated moment is too small.

frequently encountered in itinerant magnetism). Although the anisotropy can be explained through covalency arguments, we believe the band structure overemphasizes the d-p interactions. From model calculations using the 3-band Hubbard Hamiltonian, it is clear that strong Coulomb correlations will reduce the effective hopping (or hybridization) between the d and p states [76]. At the same time, the magnetic moment is enhanced.

The band-structure calculations also indicate a moment on the out-of-plane oxygen atoms (about 10% of the Ni moment). These oxygen contributions add to the (0 1 1) and (1 2 0) reflections which cause the largest disagreement with the experimental data as shown in Figure 6.9. Again, this may indicate that the covalency (with the out-of-plane oxygen atoms in this case) is predicted to be too strong from the band theory.

So far, we have used both model and first-principles approaches to describe the experimental data. Although the degree of agreement varies, qualitatively, both approaches point to a common conclusion: Covalency effects are important in the $La_2NiO_4$ compound, and are particularly pronounced in the Ni-O plane.

## E. Analysis of the Experimental Data of $La_2CuO_4$ and $Sr_2CuO_2Cl_2$

As a natural extension of the discussion, we apply the covalency model to address the antiferromagnetic form factor of $La_2CuO_4$. In an ionic model, the $Cu^{2+}$ ion has a $d^9$ configuration with the only unpaired electron occupying the $d_{x^2-y^2}$ orbital. Thus, the modelling is much simpler than in the Ni compound. As shown in Figure 6.11 and Table X, an excellent fit is obtained with the $d_{x^2-y^2}$ covalency model. The fit leads to a mixing parameter $A_{x^2-y^2} = 0.51 \pm 0.02$ and a moment $m_{x^2-y^2} = 0.61 \pm 0.03\ \mu_B$. The value of this mixing parameter is in excellent agreement with that obtained for the Ni compound and consistent with the results of paramagnetic band-structure calculations [27], which show that the states at the Fermi level have 40% Cu $d_{x^2-y^2}$ character. Notice that $m_{x^2-y^2}$ is smaller than expected for a free $Cu^{2+}$ ion, which is about 1 $\mu_B$. Such a difference may be attributed to the well-known quantum spin fluctuation effects. The ordered moment computed from the fit is $\mu_{x^2-y^2} = 0.25\ \mu_B$. Thus, in this model, the covalency effects reduce the moment from $m_{x^2-y^2} = 0.61\ \mu_B$ to $\mu_{x^2-y^2} = 0.25\ \mu_B$.

Table X. Least-squares fits to the experiment data of $La_2CuO_4$ with various models: (1) spherical 3d; (2) $d_{x^2-y^2}$ orbital; (3) $d_{x^2-y^2}$ orbital including covalency effects. The definition of various parameters follows Table IX.

| (h k *l*) | $\sin\theta/\lambda$ ($Å^{-1}$) | $\mu f(Q)$ ($\mu_B$) | (1) | (2) | (3) |
|---|---|---|---|---|---|
| (1 0 0) | 0.0935 | 0.250±0.002 | 0.271 | 0.270 | 0.259 |
| (0 1 1) | 0.1008 | 0.288±0.006 | 0.268 | 0.269 | 0.259 |
| (0 1 3) | 0.1468 | 0.261±0.003 | 0.245 | 0.260 | 0.253 |
| (0 1 5) | 0.2106 | 0.264±0.006 | 0.209 | 0.243 | 0.242 |
| (3 0 0) | 0.2805 | 0.186±0.003 | 0.167 | 0.131 | 0.188 |
| (3 0 2) | 0.2905 | 0.186±0.006 | 0.161 | 0.130 | 0.185 |
| (0 5 5) | 0.4675 | 0.00±0.09 | 0.079 | 0.013 | 0.021 |
| reduced $\chi^2$ | | | 47.3 | 90.7 | 12.7 |
| Overlap Integrals | | | — | — | $S_{x^2-y^2} = -0.0633$ |
| Mixing Parameters | | | — | — | $A_{x^2-y^2} = 0.51\pm0.02$ |
| Moments ($\mu_B$) | | | — | — | $m_{x^2-y^2} = 0.61\pm0.03$ |
| Net Ordered Moments ($\mu_B$) | | | 0.29 | 0.30 | 0.25 |

An excellent fit can also be obtained for the $Sr_2CuO_2Cl_2$ compound with this model. Due to the large error bars of the experimental data, the fit is not very sensitive to the fitting parameters in the vicinity of minimum $\chi^2$. If both $m_{x^2-y^2}$ and $A_{x^2-y^2}$ are varied, we obtain an excellent fit with $m_{x^2-y^2} = 1.27\pm0.29\ \mu_B$ and $A_{x^2-y^2} = 0.82\pm0.11$. These values are, however, too large and are difficult to interpret. A statistically equally good

fit can be obtained if one fixes $A_{x^2-y^2}$ =0.51, a value taken from the fit to the $La_2CuO_4$ data, and varies $m_{x^2-y^2}$ only. In this case, the least-squares fit gives $m_{x^2-y^2} = 0.63\pm0.02\ \mu_B$. We view this set of parameters more sensible physically. The results for the $Sr_2CuO_2Cl_2$ compound are summarized in Table IX and Figure 6.12.

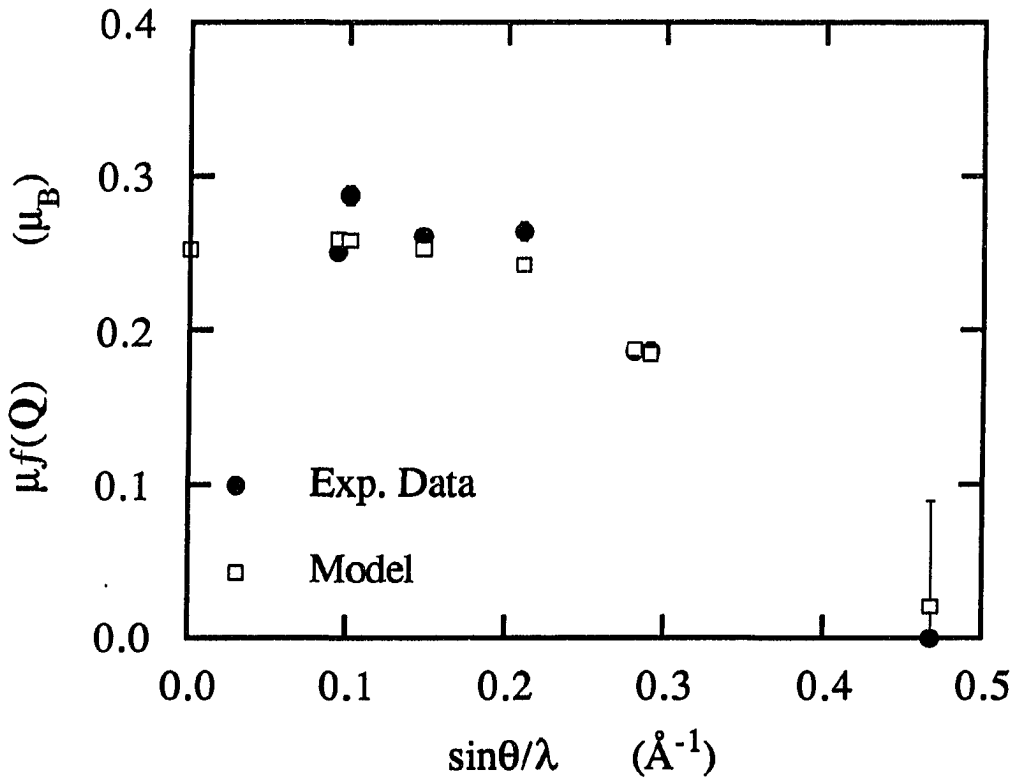


Figure 6.11 Least-squares fit to the experimental data of $La_2CuO_4$ using a covalency model arising from the Cu $d_{x^2-y^2}$ mixed with O $2p_{x,y}$ orbitals. Notice for the two data points around 0.3 $Å^{-1}$, the calculated values nearly overlap with the data.

Table XI. Least-squares fits to the experiment data of $Sr_2CuO_2Cl_2$ with various models: (1) $d_{x^2-y^2}$ only; (2) $d_{x^2-y^2}$ mixed with oxygen atoms under no constraints; (3) $d_{x^2-y^2}$ mixed with oxygen atoms and with $A_{x^2-y^2}$ fixed at 0.51 (see text). The definition of various parameters follows Table IX.

| (h k *l*) | $\sin\theta/\lambda$ ($Å^{-1}$) | $\mu f(Q)$ ($\mu_B$) | (1) | (2) | (3) |
|---|---|---|---|---|---|
| (1/2 1/2 0) | 0.0892 | 0.26±0.02 | 0.28 | 0.26 | 0.27 |
| (1/2 1/2 2) | 0.1100 | 0.26±0.01 | 0.28 | 0.26 | 0.27 |
| (1/2 1/2 3) | 0.1315 | 0.28±0.02 | 0.27 | 0.26 | 0.27 |
| (3/2 3/2 0) | 0.2677 | 0.23±0.02 | 0.15 | 0.24 | 0.20 |
| (3/2 3/2 6) | 0.3301 | 0.20±0.02 | 0.14 | 0.21 | 0.18 |
| (3/2 5/2 1) | 0.3693 | 0.16±0.03 | 0.08 | 0.12 | 0.10 |
| (3/2 3/2 8) | 0.3715 | 0.22±0.03 | 0.13 | 0.20 | 0.17 |
| (5/2 5/2 0) | 0.4461 | 0.00±0.14 | 0.02 | 0.04 | 0.03 |
| reduced $\chi^2$ | | | 6.0 | 0.7 | 1.6 |
| Overlap Integrals ($S_{x^2-y^2}$) | | | — | -0.0573 | -0.0573 |
| Mixing Parameters ($A_{x^2-y^2}$) | | | — | 0.82±0.11 | 0.51(fixed) |
| Moments ($m_{x^2-y^2}$, in $\mu_B$) | | | — | 1.27±0.29 | 0.63±0.02 |
| Net Ordered Moments ($\mu_B$) | | | 0.31 | 0.24 | 0.27 |

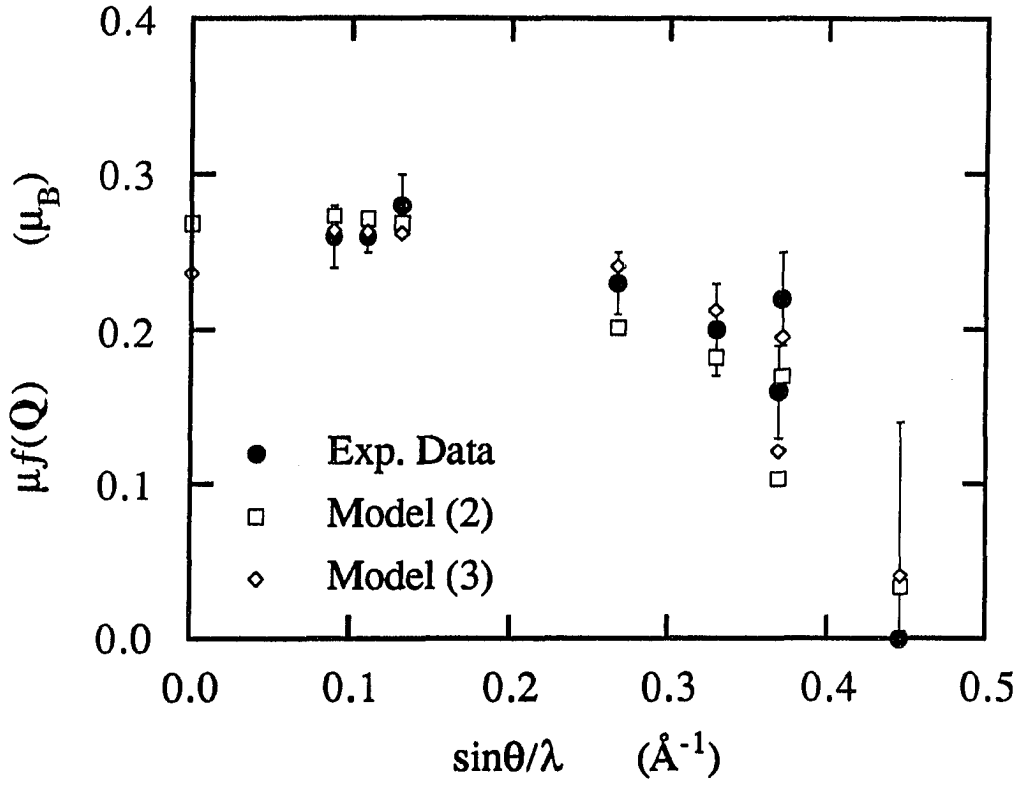


Figure 6.12 Least-squares fits to the experimental data of $Sr_2CuO_2Cl_2$ using a covalency model arising from the Cu $d_{x^2-y^2}$ mixed with O $2p_{x,y}$ orbitals. The symbols are: solid circles, experimental data; diamonds, both $m_{x^2-y^2}$ and $A_{x^2-y^2}$ are varied; squares, with $A_{x^2-y^2}$ fixed at 0.51 (see text).

# VII. SUMMARY

In this dissertation, neutron diffraction techniques were used to study the antiferromagnetic form factor (so as to obtain information of the electronic structures) of high-$T_c$ compounds. Two compounds were investigated: $Sr_2CuO_2Cl_2$ and $La_2NiO_4$. In both cases, the experimentally determined form factor exhibited a plateau at low Q values, similar to that observed for $La_2CuO_4$. These experimental data as well as the data for $La_2CuO_4$ were fitted to models in which we incorporated covalency effects. Our analysis showed that covalency effects in the Ni-O or Cu-O plane may be responsible for the plateau observed at low Q values in the antiferromagnetic form factor of these compounds. We arrived at a similar conclusion from a comparison of the $La_2NiO_4$ data with the first-principle spin-polarized band calculations, although the band theoretical results seem to overemphasize the degree of d-p interaction.

Covalency effects can also be observed in NMR experiments. Recent NMR measurements by Borsa et al. [77] on polycrystalline $Sr_2CuO_2Cl_2$ samples revealed that the Cu-Cl bond is largely ionic, meaning the covalent coupling between the Cu and Cl atoms was very weak. In our analysis, we always assumed that the $d_{x^2-y^2}$ did not mix with the $2p_z$ orbital of the out-of-plane O or Cl atoms, because their wavefunctions are perpendicular. In this regard, the experimental results by Borsa et al. actually validated our assumptions. Notice that the mixing parameters can also be calculated from the hyperfine parameters measured in NMR experiments [31-32]. Therefore, it will be interesting to see whether such parameters agree with those obtained in our neutron-diffraction experiments.

Contrary to the antiferromagnetic form factor measurements, however, little covalency effects, if any, were found in the field-induced form factor measurements. As we discussed in Chapter I, the field-induced form factor of $La_2CuO_4$ is rather consistent with the spherical $Cu^{2+}$ form factor to within the experimental precision. Recently, Lander et al. [78] conducted similar measurements on a Sr-doped $La_2NiO_4$ sample with much greater precision. Once again their results agree very well with the spherical $Ni^{2+}$ form factor. This is an area that remains to be understood. Clearly, more experimental work is needed, especially in the antiferromagnetic form factor measurements. In order to unambiguously establish the electronic nature of these compounds, we need not only to conduct more precise measurements but also to extend these measurements to high Q values beyond present work.

Another unclear aspect of the covalency models concerns the moments of $La_2CuO_4$. As noted in Chapter I, the ordered moment varies as a function of Néel temperature (Figure 1.10). The maximum value of the moment is ~ 0.5 $\mu_B$, if one assumes $f(\mathbf{Q}) = 1$ for the first reflection. The $La_2CuO_4$ data analyzed in Chapter VI were measured by Freltoft et al. [28] on a sample with Néel temperature ~ 185 K. Our fit to this set of data using a covalency model leads to an ordered moment $\mu = 0.25\ \mu_B$. According to this model, there is about a 60% reduction from the moment $m_{x^2-y^2} = 0.61\ \mu_B$. If we simply apply this result to the compound with the highest $T_N$, we will obtain a moment $m_{x^2-y^2} \sim 1.2\ \mu_B$, but this would leave no room for the quantum spin fluctuation effects [79], which are believed to play a substantial role in the antiferromagnetism of the compound. However, until a comprehensive theory is developed addressing both covalency and quantum spin fluctuation effects, it is difficult to make a detailed comparison with the experiments, especially since the neutron experiments measure the average moment which, of course, depends on the stoichiometry of the samples. It is

clear from the above discussion that there is need for experiments on stoichiometric samples, presumably those with the highest possible $T_N$, and a further development of the theory to resolve these issues.

## REFERENCES


1. For recent reviews, see *Physical Properties of High Temperature Superconductors*, Vols. I and II, edited by D. M. Ginsberg (World Scientific, Singapore, 1989 and 1990).

2. C. Michel and B. Raveau, Rev. Chim. Miner. **21**, 407 (1984).

3. J. D. Jorgensen, H.-B. Schuttler, D. G. Hinks, D. W. Capone, II, K. Zhang, M. B. Brodsky, and D. J. Scalapino, Phys. Rev. Lett. **58**, 1024 (1987).

4. J. M. Delgado, R. K. McMullan, G. Diaz de Delgado, B. J. Wuensch, P. J. Picone, H. P. Jenssen, and D. R. Gabbe, Phys. Rev. B **37**, 9343 (1988); A. J. Schultz, C.-K. Loong, J. Z. Liu, W.-K. Kwok, G. W. Crabtree, and D. J. Lam, Physica C **157**, 301 (1989).

5. D. Vaknin, S. K. Sinha, D. E. Moncton, D. C. Johnston, J. M. Newsam, C. R. Safinya, and H. E. King, Jr., Phys. Rev. Lett. **58**, 2802 (1987).

6. J. D. Axe, A. H. Moudden, D. Hohlwein, D. E. Cox, K. M. Mohanty, A. R. Moodenbaugh, and Y. Xu, Phys. Rev. Lett. **62**, 2751 (1989).

7. D. E. Cox, P. Zolliker, J. D. Axe, A. H. Moudden, A. R. Moodenbaugh, and Y. Xu, Mat. Res. Soc. Symp. Proc. **156**, 141 (1989).

8. J. Rodriguez-Cavajal, J. L. Martinez, J. Pannetier, and R. Saez-Puche, Phys. Rev. B **38**, 7148 (1988).

9. G. H. Lander, P. J. Brown, J. Spalek, and J. M. Honig, Phys. Rev. B **40**, 4463 (1990).

10. J. L. Martinez, M. T. Fernandez-Diaz, J. Rodriguez-Carvajal, and P. Odier, Phys. Rev. B **43**, 13766 (1991).

11. K. Yamada, M. Matsuda, Y. Endoh, B. Keimer, R. J. Birgeneau, S. Onodera, J. Mizusaki, T. Matsuura, and G. Shirane, Phys. Rev. B **39**, 2336 (1989).

12. D. C. Johnston, J. P. Stokes, D. P. Goshorn, and J. T. Lewandowski, Phys. Rev. B **36**, 4007 (1987).

13. S. Mitsuda, G. Shirane, S. K. Sinha, D. C. Johnston, M. S. Alvarez, D. Vaknin, and D. E. Moncton, Phys. Rev. B **36**, 822 (1987).

14. B. X. Yang, S. Mitsuda, G. Shirane, Y. Yamaguchi, H. Yamaguchi, and Y. Syono, J. Phys. Soc. Japan **56**, 2283 (1987).

15. T. Freltoft, J. E. Fischer, G. Shirane, D. E. Moncton, S. K. Sinha, D. Vaknin, J. P. Remeika, A. S. Cooper, and D. Harshman, Phys. Rev. B **36**, 826 (1987).

16. K. Yamada, E. Kudo, Y. Endoh, Y. Hidaka, M. Oda, M. Suzuki, and T. Murakami, Solid State Comm. **64**, 753 (1987).

17. G. Shirane, Y. Endoh, R. J. Birgeneau, M. A. Kastner, Y. Hidaka, M. Oda, M. Suzuki, and T. Murakami, Phys. Rev. Lett. **59**, 1613 (1987).

18. Y. Endoh, K. Yamada, R. J. Birgeneau, D. R. Gabbe, H. P. Jenssen, M. A. Kastner, C. J. Peters, P. J. Picone, T. R. Thurston, J. M. Tranquada, G. Shirane, Y. Hidaka, M. Oda, Y. Enomoto, M. Suzuki, and T. Murakami, Phys. Rev. B **37**, 7443 (1988).

19. K. Yamada, K. Kakurai, Y. Endoh, T. R. Thurston, M. A. Kastner, R. J. Birgeneau, G. Shirane, Y. Hidaka, and T. Murakami, Phys. Rev. B **40**, 4557 (1989).

20. S. Chakravarty, B. I. Halperin, and D. R. Nelson, Phys. Rev. Lett. **60**, 1057 (1988); Phys. Rev. B **39**, 2344 (1989); S. Tyc, B. I. Halperin, and S. Chakravarty, Phys. Rev. Lett. **62**, 835 (1989).

21. G. Aeppli, S. M. Hayden, H. A. Mook, Z. Fisk, S-W. Cheong, D. Rytz, J. P. Remeika, G. P. Espinosa, and A. S. Cooper, Phys. Rev. Lett. **62**, 2052 (1989).

22. S. M. Hayden, G. Aeppli, H. A. Mook, S.-W. Cheong, and Z. Fisk, Phys. Rev. B **42**, 10220 (1990).

23. S. M. Hayden, G. Aeppli, R. Osborn, A. D. Taylor, T. G. Perring, S.-W. Cheong, and Z. Fisk, Phys. Rev. Lett. **67**, 3622 (1991).

24. D. C. Johnston, Phys. Rev. Lett. **62**, 957 (1989).

25. K. B. Lyons, P. A. Fleury, J. P. Remeika, A. S. Cooper, and T. J. Negran, Phys. Rev. B **37**, 2353 (1988); R. R. P. Singh, P. A. Fleury, K. B. Lyons, and P. E. Sulewski, Phys. Rev. Lett. **62**, 2736 (1989).

26. For a review, see W. E. Pickett, Rev. Mod. Phys. **61**, 433 (1989).

27. T. C. Leung, X. W. Wang, and B. N. Harmon, Phys. Rev. B **37**, 384 (1988).

28. T. Freltoft, G. Shirane, S. Mitsuda, J. P. Remeika, and A. S. Cooper, Phys. Rev. B **37**, 137 (1988).

29. C. Stassis, B. N. Harmon, T. Freltoft, G. Shirane, S. K. Sinha, K. Yamada, Y. Endoh, Y. Hidaka, and T. Murakami, Phys. Rev. B **38**, 9291 (1988).

30. J. Akimitsu and Y. Ito, J. Phys. Soc. Japan **40**, 1621 (1976).

31. K. Hirakawa and H. Ikeda, Phys. Rev. Lett. **33**, 347 (1974).

32. I. Yamada, J. Phys. Soc. Japan, **33**, 979 (1972).

33. M. Gross, E. Sanchez-Valasco, and E. Sigga, Phys. Rev. B **39**, 2484 (1989); J. D. Reger and A. P. Young, Phys. Rev. B **37**, 5978 (1988).

34. P. W. Anderson, Phys. Rev. **86**, 694 (1952).

35. B. Grande and Hk. Müller-Buschbaum, Z. Anorg. Allg. Chem. **417**, 68 (1975).

36. W. Marshall and S. W. Lovesey, *Theory of Thermal Neutron Scattering* (Oxford University Press, 1971).

37. G. L. Squires, *Introduction to the Theory of Thermal Neutron Scattering* (Cambridge University Press, 1978).

38. G. E. Bacon, *Neutron Diffraction*, 3rd edition (Oxford University Press, 1975).

39. D. L. Price and K. Skold, in *Methods of Experimental Physics*, Vol. 23 A, *Neutron Scattering*, edited by K. Skold and D. L. Price (Academic Press, 1986).

40. J. Rossat-Mignod, in *Methods of Experimental Physics*, Vol. 23 C, *Neutron Scattering*, edited by K. Skold and D. L. Price (Academic Press, 1986).

41. G. Venkataraman, L. A. Feldkamp, and V. G. Sahni, *Dynamics of Perfect Crystals* (MIT Press, 1975).

42. For detailed discussions of the effects of Debye-Waller factor in diffraction experiments, see B. T. M. Willis and A. W. Pryor, *Thermal Vibrations in Crystallography* (Cambridge University Press, 1975).

43. J. M. Carpenter and W. B. Yelon, in *Methods of Experimental Physics*, Vol. 23 A, *Neutron Scattering*, edited by K. Skold and D. L. Price (Academic Press, 1986).

44. C. G. Windsor, in *Methods of Experimental Physics*, Vol. 23 A, *Neutron Scattering*, edited by K. Skold and D. L. Price (Academic Press, 1986).

45. A. J. Schultz, in *Methods of Experimental Physics*, Vol. 23 A, *Neutron Scattering*, edited by K. Skold and D. L. Price (Academic Press, 1986).

46. A. J. Schultz, *Single Crystal Diffraction User's Guide and Reference Manual*, Argonne National Laboratory, May 1988 (unpublished).

47. A. J. Schultz (private communication).

48. C. Wilkinson and A. J. Schultz, J. Appl. Cryst. **22**, 110 (1989); *IPNS Progress Report*, 1985-1986, Argonne National Laboratory.

49. P. J. Becker and P. Coppens, Acta. Cryst. A **30**, 129 (1974); *ibid.* A **30**, 148 (1974); *ibid.* A **31**, 417 (1975).

50. W. Jauch, A. J. Schultz, and G. Heger, J. Appl. Cryst. **20**, 117 (1987).

51. W. Jauch, A. J. Schultz, and J. Schneider, J. Appl. Cryst. **21**, 975 (1988).

52. *IPNS Progress Report*, 1986-1988, Argonne National Laboratory.

53. *IPNS Progress Report*, 1988-1990, Argonne National Laboratory.

54. J. D. Jorgensen, J. Faber, Jr., J. M. Carpenter, R. K. Crawford, J. Haumann, R. L. Hitterman, R. Kleb, G. E. Ostrowskin, F. J. Rotella, and T. G. Worlton, J. Appl. Cryst. **22**, 321 (1989).

55. F. J. Rotella, *Users Manual For Rietveld Analysis at IPNS*, Argonne National Laboratory, November 1988 (unpublished).

56. R. B. Von Dreele, J. D. Jorgensen, and C. G. Windsor, J. Appl. Cryst. **15**, 581 (1982).

57. G. A. Lager, F. K. Ross, F. J. Rotella, and J. D. Jorgensen, J. Appl. Cryst. **14**, 137 (1981).

58. L. L. Miller, X. L. Wang, S. X. Wang, C. Stassis, D. C. Johnston, J. Faber Jr., and C.-K. Loong, Phys. Rev. B **41**, 1921 (1990).

59. H. H. Wang, U. Geiser, R. J. Thorn, K. D. Carlson, M. A. Bono, M. R. Monaghan, T. J. Allen, R. B. Proksch, D. L. Stupka, W. K. Kwok, G. W. Crabtree, and J. M. Williams, Inorg. Chem. **26**, 1190 (1987).

60. R. D. Shannon, Acta. Cryst. A **32**, 751 (1976).

61. D. Vaknin, S. K. Sinha, C. Stassis, L. L. Miller, and D. C. Johnston, Phys. Rev. B **41**, 1926 (1990).

62. This possibility was suggested to us by W. E. Pickett (private communication).

63. G. Aeppli and D. J. Buttrey, Phys. Rev. Lett. **61**, 203 (1988).

64. T. Freltoft, D. J. Buttrey, G. Aeppli, D. Vaknin, and G. Shirane, Phys. Rev. **B** 44, 5046 (1991).

65. J. Fontcuberta, G. Langworth, and J. B. Goodenough, Phys. Rev. B **37**, 6320 (1984).

66. R. R. Schartman, and J. M. Honig, Mat. Res. Bull. **24**, 671 (1989); D. J. Buttrey, J. M. Honig, and C. N. R. Rao, J. Solid State Chem. **64**, 287 (1986).

67. R. M. Moon, J. Phys. **43**, C7-187 (1982), and references cited therein.

68. R. J. Weiss, *X-ray Determination of Electrons Distributions* (North Holland, Amesterdam, 1966).

69. J. Owen and J. H. M. Thornley, Report of Progress in Phys. **29**, 675 (1966); J. Hubbard and W. Marshall, Proc. Phys. Soc. **86**, 561 (1965).

70. R. E. Watson and A. J. Freeman, Phys. Rev. **120**, 1125 (1960).

71. For detailed mathematical properties of special functions, see W. Magnus, F. Oberhettinger, and R. P. Soni, *Formulars and Theorems for the Special Functions of Mathmatical Physics* (Spring-Verlag, New York, 1966).

72. See, for instance, C. Kittel, *Introduction to Solid State Physics*, 6th edition (John Wiley and Sons, 1986).

73. R. J. Weiss and A. J. Freeman, J. Phys. Chem. Solids **10**, 147 (1959).

74. E. U. Condon and G. H. Shortley, *Theory of Atomic Spectra*, revised edition (Cambridge University Press, 1951).

75. G. Y. Guo and W. M. Temmerman, J. Phys. C **21**, L803 (1988).

76. T. C. Leung, Ph.D. Thesis, Iowa State University, Ames (1991).

77. F. Borsa, M. Corti, T. Goto, A. Rigamonti, D. C. Johnston, and F. C. Chou, Phys. Rev. B (in press).

78. G. H. Lander, P. J. Brown, C. Stassis, P. Gopalan, J. Spalek, and J. M. Honig, Phys. Rev. B. **43**, 448 (1991).

79. T. A. Kaplan, S. D. Mahanti, and Hyunju Chang, Phys. Rev. B **45**, 2565 (1992); T. A. Kaplan and S. D. Mahanti, J. Appl. Phys. **69**, 5382 (1991), and references cited therein.

## ACKNOWLEDGMENTS

I would like to thank my adviser Professor C. Stassis for his guidance, encouragement, and care throughout this study. From him I have learned not only the experimental skills but also the attitude of a scientist. I am also much indebted to Dr. C.-K. Loong of Argonne National Laboratory for advice and practical help and to Dr. G. H. Lander of the European Institute for Transuranium Elements, Federal Republic of Germany, for his initiative of the $La_2NiO_4$ project and many stimulating communications.

Appreciation is extended to Professor J. M. Honig of Purdue University and to Professor D. C. Johnston and Dr. L. L. Miller of Iowa State University for providing high quality samples. Without their persistent endeavor, this work would never commence.

In addition, I would like to acknowledge the assistance from many scientists at Argonne National Laboratory during the experiments and subsequent data analysis. Among those to whom I owe specific gratitude are Drs. A. J. Schultz, J. Faber, Jr., F. J. Rotella, and J. M. Carpenter.

I have benefitted a great deal from helpful discussions with many people including, but not limited to, Professor B. N. Harmon, Dr. T. C. Leung, Mr. J. Ye, Professor D. C. Johnston, all from Iowa State University, and Dr. S. K. Sinha from Exxon Research and Engineering Company. In addition, Mr. J. Ye kindly supplied his Hartree-Fock calculation results of the radial wavefunctions. All are appreciated. Special thanks are sent to Dr. S. K. Sinha for a critical suggestion which led to systematic investigations of modelling the experimental data.

Ms. R. A. Shivvers cheerfully edited this manuscript. Her excellent technical editing skills are gratefully acknowledged.

Finally, I would like to thank my wife and my parents for their love, support and understanding. I am especially grateful to my father, Jin-Zhen Wang, who opened my eyes to the magnificent world of science during my childhood.

Part of this work was performed at Ames Laboratory under contract no. W-7405-Eng-82 with the U. S. Department of Energy (USDOE). Work performed at Argonne National Laboratory was supported by the USDOE under contract no. W-31-109-Eng-38. The United States Government has assigned the DOE report number IS-T 1580 to this dissertation.

# APPENDIX I. CALCULATED STRUCTURE FACTORS FOR $Sr_2CuO_2Cl_2$ AT T = 300 K

Table XII. Calculated structure factors for $Sr_2CuO_2Cl_2$ at T = 300 K. The calculations were based on structural parameters listed in Table I. The Debye-Waller factors were not included.

| *h* | *k* | *l* | d (Å) | sinθ/λ (Å$^{-1}$) | \| F \| |
|---|---|---|---|---|---|
| 0 | 0 | 2 | 7.8063 | 0.0164 | 1.91 |
| 0 | 0 | 4 | 3.9032 | 0.0656 | 0.95 |
| 1 | 0 | 1 | 3.8490 | 0.0675 | 0.95 |
| 1 | 0 | 3 | 3.1572 | 0.1003 | 0.91 |
| 1 | 1 | 0 | 2.8083 | 0.1268 | 5.80 |
| 1 | 1 | 2 | 2.6425 | 0.1432 | 2.73 |
| 0 | 0 | 6 | 2.6021 | 0.1477 | 5.28 |
| 1 | 0 | 5 | 2.4547 | 0.1660 | 7.52 |
| 1 | 1 | 4 | 2.2796 | 0.1924 | 3.69 |
| 2 | 0 | 0 | 1.9858 | 0.2536 | 10.44 |
| 0 | 0 | 8 | 1.9516 | 0.2626 | 1.86 |
| 1 | 0 | 7 | 1.9447 | 0.2644 | 0.75 |
| 2 | 0 | 2 | 1.9245 | 0.2700 | 1.91 |
| 1 | 1 | 6 | 1.9087 | 0.2745 | 0.64 |
| 2 | 0 | 4 | 1.7699 | 0.3192 | 0.95 |
| 2 | 1 | 1 | 1.7648 | 0.3211 | 0.95 |
| 1 | 2 | 1 | 1.7648 | 0.3211 | 0.95 |
| 2 | 1 | 3 | 1.6810 | 0.3539 | 0.91 |
| 1 | 2 | 3 | 1.6810 | 0.3539 | 0.91 |
| 1 | 1 | 8 | 1.6026 | 0.3894 | 2.78 |
| 1 | 0 | 9 | 1.5897 | 0.3957 | 3.45 |
| 2 | 0 | 6 | 1.5786 | 0.4013 | 5.28 |
| 0 | 0 | 10 | 1.5613 | 0.4103 | 8.18 |

| *h* | *k* | *l* | d (Å) | sinθ/λ (Å$^{-1}$) | \| F \| |
|---|---|---|---|---|---|
| 2 | 1 | 5 | 1.5439 | 0.4195 | 7.52 |
| 1 | 2 | 5 | 1.5439 | 0.4195 | 7.52 |
| 2 | 2 | 0 | 1.4042 | 0.5072 | 10.44 |
| 2 | 0 | 8 | 1.3919 | 0.5161 | 1.86 |
| 1 | 2 | 7 | 1.3894 | 0.5180 | 0.75 |
| 2 | 1 | 7 | 1.3894 | 0.5180 | 0.75 |
| 2 | 2 | 2 | 1.3820 | 0.5236 | 1.91 |
| 1 | 1 | 10 | 1.3646 | 0.5370 | 3.54 |
| 1 | 0 | 11 | 1.3365 | 0.5598 | 4.21 |
| 2 | 2 | 4 | 1.3213 | 0.5728 | 0.95 |
| 3 | 0 | 1 | 1.3191 | 0.5747 | 0.95 |
| 0 | 0 | 12 | 1.3010 | 0.5908 | 4.44 |
| 3 | 0 | 3 | 1.2830 | 0.6075 | 0.91 |
| 3 | 1 | 0 | 1.2559 | 0.6340 | 5.80 |
| 1 | 3 | 0 | 1.2559 | 0.6340 | 5.80 |
| 2 | 1 | 9 | 1.2410 | 0.6493 | 3.45 |
| 1 | 2 | 9 | 1.2410 | 0.6493 | 3.45 |
| 3 | 1 | 2 | 1.2400 | 0.6504 | 2.73 |
| 1 | 3 | 2 | 1.2400 | 0.6504 | 2.73 |
| 2 | 2 | 6 | 1.2357 | 0.6549 | 5.28 |
| 2 | 0 | 10 | 1.2274 | 0.6638 | 8.18 |
| 3 | 0 | 5 | 1.2188 | 0.6731 | 7.52 |
| 1 | 3 | 4 | 1.1956 | 0.6996 | 3.69 |
| 3 | 1 | 4 | 1.1956 | 0.6996 | 3.69 |
| 1 | 1 | 12 | 1.1805 | 0.7176 | 0.20 |
| 1 | 0 | 13 | 1.1496 | 0.7567 | 0.93 |
| 2 | 2 | 8 | 1.1398 | 0.7697 | 1.86 |
| 3 | 0 | 7 | 1.1384 | 0.7716 | 0.75 |
| 1 | 3 | 6 | 1.1311 | 0.7817 | 0.64 |
| 3 | 1 | 6 | 1.1311 | 0.7817 | 0.64 |
| 0 | 0 | 14 | 1.1152 | 0.8041 | 2.43 |
| 2 | 1 | 11 | 1.1088 | 0.8134 | 4.21 |

| *h* | *k* | *l* | d (Å) | sinθ/λ ($Å^{-1}$) | \|F\| |
|---|---|---|---|---|---|
| 1 | 2 | 11 | 1.1088 | 0.8134 | 4.21 |
| 2 | 3 | 1 | 1.0988 | 0.8283 | 0.95 |
| 3 | 2 | 1 | 1.0988 | 0.8283 | 0.95 |
| 2 | 0 | 12 | 1.0883 | 0.8443 | 4.44 |
| 3 | 2 | 3 | 1.0776 | 0.8611 | 0.91 |
| 2 | 3 | 3 | 1.0776 | 0.8611 | 0.91 |
| 1 | 3 | 8 | 1.0561 | 0.8965 | 2.78 |
| 3 | 1 | 8 | 1.0561 | 0.8965 | 2.78 |
| 3 | 0 | 9 | 1.0524 | 0.9029 | 3.45 |
| 2 | 2 | 10 | 1.0440 | 0.9174 | 8.18 |
| 3 | 2 | 5 | 1.0388 | 0.9267 | 7.52 |
| 2 | 3 | 5 | 1.0388 | 0.9267 | 7.52 |

# APPENDIX II. CALCULATED STRUCTURE FACTOR FOR $La_2NiO_4$ AT T = 10 K

Table XIII. Calculated Structure Factors for $La_2NiO_4$ at T = 10 K. The calculations were based on structural parameters listed in Table V. The isotropic Debye-Waller factors were included.

| *h* | *k* | *l* | d (Å) | $\sin\theta/\lambda$ ($Å^{-1}$) | \| F \| |
|---|---|---|---|---|---|
| 0 | 0 | 2 | 6.2520 | 0.0256 | 5.00 |
| 1 | 0 | 2 | 4.1303 | 0.0586 | 0.58 |
| 1 | 1 | 0 | 3.8905 | 0.0661 | 0.17 |
| 1 | 1 | 1 | 3.7148 | 0.0725 | 1.75 |
| 1 | 1 | 2 | 3.3032 | 0.0917 | 0.13 |
| 0 | 0 | 4 | 3.1260 | 0.1023 | 1.02 |
| 1 | 1 | 3 | 2.8440 | 0.1236 | 5.24 |
| 2 | 0 | 0 | 2.7510 | 0.1321 | 10.29 |
| 1 | 0 | 4 | 2.7180 | 0.1354 | 1.70 |
| 2 | 0 | 2 | 2.5180 | 0.1577 | 3.93 |
| 1 | 1 | 4 | 2.4368 | 0.1684 | 0.20 |
| 2 | 1 | 1 | 2.4143 | 0.1716 | 0.99 |
| 2 | 1 | 2 | 2.2896 | 0.1908 | 1.34 |
| 2 | 1 | 3 | 2.1189 | 0.2227 | 0.65 |
| 1 | 1 | 5 | 2.1037 | 0.2260 | 10.13 |
| 0 | 0 | 6 | 2.0840 | 0.2303 | 15.10 |
| 2 | 0 | 4 | 2.0652 | 0.2345 | 7.72 |
| 1 | 0 | 6 | 1.9489 | 0.2633 | 1.13 |
| 2 | 2 | 0 | 1.9453 | 0.2643 | 18.97 |
| 2 | 1 | 4 | 1.9335 | 0.2675 | 0.04 |
| 2 | 2 | 1 | 1.9221 | 0.2707 | 0.22 |
| 2 | 2 | 2 | 1.8574 | 0.2899 | 5.31 |
| 1 | 1 | 6 | 1.8370 | 0.2963 | 0.17 |

| *h* | *k* | *l* | d (Å) | sinθ/λ ($Å^{-1}$) | \| F \| |
|---|---|---|---|---|---|
| 2 | 2 | 3 | 1.7627 | 0.3218 | 0.53 |
| 3 | 0 | 2 | 1.7598 | 0.3229 | 3.20 |
| 2 | 1 | 5 | 1.7539 | 0.3251 | 0.50 |
| 3 | 1 | 0 | 1.7399 | 0.3303 | 0.48 |
| 3 | 1 | 1 | 1.7233 | 0.3367 | 1.47 |
| 3 | 1 | 2 | 1.6762 | 0.3559 | 0.24 |
| 2 | 0 | 6 | 1.6612 | 0.3624 | 6.26 |
| 2 | 2 | 4 | 1.6516 | 0.3666 | 1.20 |
| 1 | 1 | 7 | 1.6234 | 0.3795 | 1.84 |
| 3 | 1 | 3 | 1.6056 | 0.3879 | 5.76 |
| 2 | 1 | 6 | 1.5903 | 0.3954 | 1.15 |
| 3 | 0 | 4 | 1.5819 | 0.3996 | 1.72 |
| 0 | 0 | 8 | 1.5630 | 0.4093 | 9.69 |
| 2 | 2 | 5 | 1.5354 | 0.4242 | 0.46 |
| 3 | 1 | 4 | 1.5203 | 0.4327 | 0.02 |
| 3 | 2 | 1 | 1.5147 | 0.4358 | 0.76 |
| 1 | 0 | 8 | 1.5035 | 0.4424 | 0.89 |
| 3 | 2 | 2 | 1.4825 | 0.4550 | 2.24 |
| 1 | 1 | 8 | 1.4503 | 0.4754 | 0.66 |
| 2 | 1 | 7 | 1.4455 | 0.4786 | 1.75 |
| 3 | 2 | 3 | 1.4330 | 0.4870 | 0.59 |
| 3 | 1 | 5 | 1.4282 | 0.4902 | 9.47 |
| 2 | 2 | 6 | 1.4220 | 0.4945 | 14.23 |
| 3 | 0 | 6 | 1.3768 | 0.5276 | 1.16 |
| 4 | 0 | 0 | 1.3755 | 0.5285 | 17.98 |
| 3 | 2 | 4 | 1.3713 | 0.5318 | 3.10 |
| 2 | 0 | 8 | 1.3590 | 0.5415 | 2.06 |
| 4 | 0 | 2 | 1.3434 | 0.5541 | 5.60 |
| 3 | 1 | 6 | 1.3356 | 0.5606 | 0.72 |
| 4 | 1 | 1 | 1.3269 | 0.5680 | 1.67 |
| 2 | 1 | 8 | 1.3193 | 0.5745 | 1.99 |
| 2 | 2 | 7 | 1.3157 | 0.5777 | 0.01 |

| *h* | *k* | *l* | d (Å) | sinθ/λ ($Å^{-1}$) | \| F \| |
|---|---|---|---|---|---|
| 1 | 1 | 9 | 1.3084 | 0.5841 | 0.60 |
| 4 | 1 | 2 | 1.3050 | 0.5872 | 0.37 |
| 3 | 2 | 5 | 1.3026 | 0.5893 | 0.34 |
| 3 | 3 | 0 | 1.2968 | 0.5946 | 1.35 |
| 3 | 3 | 1 | 1.2899 | 0.6010 | 1.23 |
| 4 | 1 | 3 | 1.2709 | 0.6191 | 1.22 |
| 3 | 3 | 2 | 1.2698 | 0.6202 | 0.78 |
| 4 | 0 | 4 | 1.2590 | 0.6309 | 1.37 |
| 0 | 0 | 10 | 1.2504 | 0.6396 | 4.03 |
| 3 | 1 | 7 | 1.2464 | 0.6437 | 1.81 |
| 3 | 3 | 3 | 1.2383 | 0.6522 | 6.17 |
| 3 | 2 | 6 | 1.2312 | 0.6597 | 1.16 |
| 4 | 2 | 0 | 1.2303 | 0.6607 | 8.75 |
| 4 | 1 | 4 | 1.2273 | 0.6639 | 1.42 |
| 4 | 2 | 1 | 1.2244 | 0.6671 | 0.39 |
| 1 | 0 | 10 | 1.2193 | 0.6726 | 2.27 |
| 2 | 2 | 8 | 1.2184 | 0.6736 | 10.03 |
| 2 | 1 | 9 | 1.2098 | 0.6832 | 1.44 |
| 4 | 2 | 2 | 1.2071 | 0.6863 | 3.01 |
| 3 | 3 | 4 | 1.1978 | 0.6969 | 0.57 |
| 1 | 1 | 10 | 1.1904 | 0.7057 | 0.80 |
| 3 | 0 | 8 | 1.1896 | 0.7066 | 3.06 |
| 4 | 2 | 3 | 1.1800 | 0.7182 | 0.93 |
| 4 | 1 | 5 | 1.1773 | 0.7215 | 0.79 |
| 3 | 1 | 8 | 1.1627 | 0.7397 | 0.21 |
| 3 | 2 | 7 | 1.1603 | 0.7428 | 1.49 |
| 3 | 3 | 5 | 1.1512 | 0.7545 | 8.90 |
| 4 | 0 | 6 | 1.1480 | 0.7588 | 13.40 |
| 4 | 2 | 4 | 1.1448 | 0.7630 | 7.04 |
| 2 | 0 | 10 | 1.1383 | 0.7717 | 3.09 |
| 2 | 2 | 9 | 1.1306 | 0.7823 | 0.48 |
| 4 | 1 | 6 | 1.1238 | 0.7918 | 1.17 |

| *h* | *k* | *l* | d (Å) | sinθ/λ (Å$^{-1}$) | \| F \| |
|---|---|---|---|---|---|
| 2 | 1 | 10 | 1.1147 | 0.8048 | 1.21 |
| 4 | 2 | 5 | 1.1039 | 0.8206 | 0.82 |
| 3 | 3 | 6 | 1.1011 | 0.8249 | 0.85 |
| 4 | 3 | 1 | 1.0962 | 0.8322 | 1.27 |
| 3 | 2 | 8 | 1.0919 | 0.8388 | 0.10 |
| 1 | 1 | 11 | 1.0911 | 0.8400 | 14.07 |
| 3 | 1 | 9 | 1.0857 | 0.8484 | 0.06 |
| 4 | 3 | 2 | 1.0837 | 0.8514 | 2.56 |
| 5 | 0 | 2 | 1.0837 | 0.8514 | 3.65 |
| 5 | 1 | 0 | 1.0790 | 0.8589 | 0.70 |
| 5 | 1 | 1 | 1.0750 | 0.8653 | 0.98 |
| 4 | 1 | 7 | 1.0691 | 0.8750 | 3.14 |
| 4 | 3 | 3 | 1.0639 | 0.8834 | 1.11 |
| 5 | 1 | 2 | 1.0633 | 0.8845 | 0.41 |
| 4 | 2 | 6 | 1.0594 | 0.8909 | 5.01 |
| 2 | 2 | 10 | 1.0518 | 0.9039 | 3.91 |
| 3 | 3 | 7 | 1.0494 | 0.9080 | 1.76 |
| 5 | 1 | 3 | 1.0446 | 0.9164 | 6.62 |
| 0 | 0 | 12 | 1.0420 | 0.9210 | 5.79 |
| 4 | 3 | 4 | 1.0380 | 0.9282 | 1.05 |
| 5 | 0 | 4 | 1.0380 | 0.9282 | 4.28 |
| 3 | 0 | 10 | 1.0331 | 0.9369 | 0.20 |
| 4 | 0 | 8 | 1.0326 | 0.9379 | 10.33 |
| 2 | 1 | 11 | 1.0319 | 0.9391 | 0.51 |
| 3 | 2 | 9 | 1.0273 | 0.9475 | 1.29 |
| 1 | 0 | 12 | 1.0238 | 0.9540 | 1.58 |
| 5 | 1 | 4 | 1.0200 | 0.9612 | 0.36 |
| 5 | 2 | 1 | 1.0183 | 0.9644 | 0.37 |
| 3 | 1 | 10 | 1.0154 | 0.9699 | 0.81 |
| 4 | 1 | 8 | 1.0149 | 0.9709 | 0.97 |
| 4 | 2 | 7 | 1.0132 | 0.9741 | 0.03 |

# APPENDIX III. MAGNETIC FORM FACTOR OF $Cu^{2+}$, $Ni^{2+}$, AND $O^{-}$ IONS

Table XIV. Magnetic form factor of $Cu^{2+}$ ions. The radial charge (spin) density was obtained using the restricted Hartree-Fock method and supplied by J. Ye of Ames Laboratory, Iowa State University.

| sinθ/λ | 0.00 | 0.01 | 0.02 | 0.03 | 0.04 | 0.05 | 0.06 | 0.07 | 0.08 | 0.09 |
|---|---|---|---|---|---|---|---|---|---|---|
| 0.00 | 1.0000 | 0.9992 | 0.9967 | 0.9927 | 0.9871 | 0.9800 | 0.9713 | 0.9613 | 0.9499 | 0.9373 |
| 0.10 | 0.9234 | 0.9085 | 0.8926 | 0.8757 | 0.8581 | 0.8397 | 0.8208 | 0.8013 | 0.7814 | 0.7611 |
| 0.20 | 0.7406 | 0.7200 | 0.6992 | 0.6784 | 0.6576 | 0.6369 | 0.6163 | 0.5960 | 0.5759 | 0.5560 |
| 0.30 | 0.5365 | 0.5173 | 0.4985 | 0.4800 | 0.4620 | 0.4444 | 0.4272 | 0.4104 | 0.3941 | 0.3782 |
| 0.40 | 0.3628 | 0.3479 | 0.3334 | 0.3193 | 0.3057 | 0.2925 | 0.2797 | 0.2674 | 0.2555 | 0.2440 |
| 0.50 | 0.2329 | 0.2222 | 0.2119 | 0.2019 | 0.1923 | 0.1831 | 0.1742 | 0.1657 | 0.1574 | 0.1495 |
| 0.60 | 0.1419 | 0.1346 | 0.1276 | 0.1209 | 0.1144 | 0.1082 | 0.1023 | 0.0966 | 0.0911 | 0.0859 |
| 0.70 | 0.0809 | 0.0761 | 0.0715 | 0.0671 | 0.0628 | 0.0588 | 0.0550 | 0.0513 | 0.0478 | 0.0444 |
| 0.80 | 0.0412 | 0.0382 | 0.0352 | 0.0325 | 0.0298 | 0.0273 | 0.0249 | 0.0226 | 0.0204 | 0.0183 |
| 0.90 | 0.0164 | 0.0145 | 0.0127 | 0.0110 | 0.0094 | 0.0079 | 0.0065 | 0.0051 | 0.0039 | 0.0026 |

Table XV. Magnetic form factor of $Ni^{2+}$ ions. The radial spin density was taken from Ref. 70 and it was obtained using the unrestricted (spin-polarized) Hartree-Fock method.

| sinθ/λ | 0.00 | 0.01 | 0.02 | 0.03 | 0.04 | 0.05 | 0.06 | 0.07 | 0.08 | 0.09 |
|---|---|---|---|---|---|---|---|---|---|---|
| 0.00 | 1.0000 | 0.9992 | 0.9969 | 0.9931 | 0.9878 | 0.9810 | 0.9727 | 0.9632 | 0.9523 | 0.9401 |
| 0.10 | 0.9268 | 0.9124 | 0.8970 | 0.8807 | 0.8635 | 0.8456 | 0.8270 | 0.8078 | 0.7881 | 0.7680 |
| 0.20 | 0.7476 | 0.7270 | 0.7061 | 0.6852 | 0.6642 | 0.6432 | 0.6223 | 0.6015 | 0.5809 | 0.5605 |
| 0.30 | 0.5404 | 0.5206 | 0.5011 | 0.4820 | 0.4632 | 0.4448 | 0.4268 | 0.4093 | 0.3922 | 0.3755 |
| 0.40 | 0.3593 | 0.3435 | 0.3282 | 0.3134 | 0.2990 | 0.2851 | 0.2716 | 0.2586 | 0.2460 | 0.2338 |
| 0.50 | 0.2221 | 0.2108 | 0.1999 | 0.1894 | 0.1793 | 0.1696 | 0.1603 | 0.1514 | 0.1428 | 0.1346 |
| 0.60 | 0.1267 | 0.1191 | 0.1119 | 0.1050 | 0.0983 | 0.0920 | 0.0860 | 0.0802 | 0.0747 | 0.0695 |
| 0.70 | 0.0645 | 0.0597 | 0.0552 | 0.0509 | 0.0468 | 0.0429 | 0.0392 | 0.0357 | 0.0324 | 0.0292 |
| 0.80 | 0.0262 | 0.0234 | 0.0207 | 0.0182 | 0.0158 | 0.0136 | 0.0114 | 0.0094 | 0.0076 | 0.0058 |
| 0.90 | 0.0041 | 0.0026 | 0.0011 | -0.0003 | -0.0016 | -0.0028 | -0.0039 | -0.0049 | -0.0059 | -0.0068 |

Table XVI. Magnetic form factor of $O^-$ ions. The radial charge (spin) density was obtained using the restricted Hartree-Fock method and supplied by J. Ye of Ames Laboratory, Iowa State University.

| sinθ/λ | 0.00 | 0.01 | 0.02 | 0.03 | 0.04 | 0.05 | 0.06 | 0.07 | 0.08 | 0.09 |
|---|---|---|---|---|---|---|---|---|---|---|
| 0.00 | 1.0000 | 0.9974 | 0.9896 | 0.9769 | 0.9598 | 0.9388 | 0.9144 | 0.8875 | 0.8585 | 0.8281 |
| 0.10 | 0.7967 | 0.7649 | 0.7330 | 0.7013 | 0.6700 | 0.6393 | 0.6092 | 0.5800 | 0.5516 | 0.5242 |
| 0.20 | 0.4977 | 0.4721 | 0.4476 | 0.4240 | 0.4014 | 0.3798 | 0.3591 | 0.3394 | 0.3206 | 0.3027 |
| 0.30 | 0.2856 | 0.2694 | 0.2539 | 0.2393 | 0.2254 | 0.2122 | 0.1997 | 0.1879 | 0.1766 | 0.1660 |
| 0.40 | 0.1559 | 0.1464 | 0.1374 | 0.1289 | 0.1209 | 0.1133 | 0.1061 | 0.0994 | 0.0930 | 0.0870 |
| 0.50 | 0.0813 | 0.0759 | 0.0709 | 0.0661 | 0.0616 | 0.0574 | 0.0534 | 0.0497 | 0.0461 | 0.0428 |
| 0.60 | 0.0397 | 0.0368 | 0.0340 | 0.0314 | 0.0290 | 0.0267 | 0.0246 | 0.0226 | 0.0207 | 0.0189 |
| 0.70 | 0.0172 | 0.0157 | 0.0142 | 0.0129 | 0.0116 | 0.0104 | 0.0093 | 0.0082 | 0.0073 | 0.0064 |
| 0.80 | 0.0055 | 0.0047 | 0.0040 | 0.0033 | 0.0027 | 0.0021 | 0.0015 | 0.0010 | 0.0005 | 0.0001 |
| 0.90 | -0.0003 | -0.0007 | -0.0010 | -0.0014 | -0.0017 | -0.0019 | -0.0022 | -0.0024 | -0.0026 | -0.0028 |

# APPENDIX IV. EXPLICIT EXPRESSIONS FOR 3d AND 2p WAVEFUNCTIONS

1. Spherical harmonics

$l$=0,

$$Y_{00} = \frac{1}{\sqrt{4\pi}}$$

$l$=1,

$$Y_{11} = -\sqrt{\frac{3}{8\pi}}\sin\theta\, e^{i\varphi}$$

$$Y_{10} = \sqrt{\frac{3}{4\pi}}\cos\theta$$

$l$=2,

$$Y_{22} = \frac{1}{4}\sqrt{\frac{15}{2\pi}}\sin^2\theta\, e^{i2\varphi}$$

$$Y_{21} = -\sqrt{\frac{15}{8\pi}}\sin\theta\cos\theta\, e^{i\varphi}$$

$$Y_{20} = -\sqrt{\frac{5}{4\pi}}\left(\frac{3}{2}\cos^2\theta - \frac{1}{2}\right)$$

and for all $l$ m,

$$Y_{l,-m}(\theta,\varphi) = (-)^m Y^*_{l,-m}(\theta,\varphi)$$

2. 3d wavefunctions in crystalline field

$$d_{3z^2-r^2} = Y_{2,0} = \sqrt{\frac{15}{16\pi}}\,\frac{1}{\sqrt{3}}\,\frac{(z^2-y^2)+(z^2-x^2)}{r^2}$$

$$d_{x^2-y^2} = \frac{1}{\sqrt{2}}[Y_{2,2} + Y_{2,-2}] = \sqrt{\frac{15}{16\pi}}\,\frac{x^2-y^2}{r^2}$$

$$d_{xy} = \frac{1}{\sqrt{2}}[Y_{2,2} - Y_{2,-2}] = i\sqrt{\frac{15}{16\pi}}\,\frac{2xy}{r^2}$$

$$d_{yz} = \frac{1}{\sqrt{2}}[Y_{2,1} + Y_{2,-1}] = (-i)\sqrt{\frac{15}{16\pi}}\,\frac{2yz}{r^2}$$

$$d_{zx} = \frac{1}{\sqrt{2}}[Y_{2,1} - Y_{2,-1}] = (-)\sqrt{\frac{15}{16\pi}}\,\frac{2zx}{r^2}$$

3. 2p wavefunctions in crystalline field

$$p_x = \frac{1}{\sqrt{2}}(Y_{1,1} - Y_{1,-1}) = (-)\sqrt{\frac{3}{4\pi}}\,\frac{x}{r}$$

$$p_y = \frac{1}{\sqrt{2}}(Y_{1,1} + Y_{1,-1}) = (-i)\sqrt{\frac{3}{4\pi}}\,\frac{y}{r}$$

$$p_z = Y_{1,0} = \sqrt{\frac{3}{4\pi}}\,\frac{z}{r}$$